

Marangoni flows induced by non-uniform surfactant distributions

Citation for published version (APA):

Hanyak, M. (2012). *Marangoni flows induced by non-uniform surfactant distributions*. [Phd Thesis 1 (Research TU/e / Graduation TU/e), Applied Physics and Science Education]. Technische Universiteit Eindhoven. <https://doi.org/10.6100/IR735354>

DOI:

[10.6100/IR735354](https://doi.org/10.6100/IR735354)

Document status and date:

Published: 01/01/2012

Document Version:

Publisher's PDF, also known as Version of Record (includes final page, issue and volume numbers)

Please check the document version of this publication:

- A submitted manuscript is the version of the article upon submission and before peer-review. There can be important differences between the submitted version and the official published version of record. People interested in the research are advised to contact the author for the final version of the publication, or visit the DOI to the publisher's website.
- The final author version and the galley proof are versions of the publication after peer review.
- The final published version features the final layout of the paper including the volume, issue and page numbers.

[Link to publication](#)

General rights

Copyright and moral rights for the publications made accessible in the public portal are retained by the authors and/or other copyright owners and it is a condition of accessing publications that users recognise and abide by the legal requirements associated with these rights.

- Users may download and print one copy of any publication from the public portal for the purpose of private study or research.
- You may not further distribute the material or use it for any profit-making activity or commercial gain
- You may freely distribute the URL identifying the publication in the public portal.

If the publication is distributed under the terms of Article 25fa of the Dutch Copyright Act, indicated by the "Taverne" license above, please follow below link for the End User Agreement:

www.tue.nl/taverne

Take down policy

If you believe that this document breaches copyright please contact us at:

openaccess@tue.nl

providing details and we will investigate your claim.

**Marangoni flows induced by
non-uniform surfactant distributions**



This research was financially supported by the Dutch Technology Foundation STW (project number 08066); in cooperation with Shell International Exploration and Production.

Copyright © 2012 M. Hanyak

Printed by Universiteitsdrukkerij TUE, Eindhoven, The Netherlands

CIP-DATA LIBRARY TECHNISCHE UNIVERSITEIT EINDHOVEN

Hanyak, Myroslava

Marangoni flows induced by non-uniform surfactant distributions / by Myroslava Hanyak. – Eindhoven: Technische Universiteit Eindhoven, 2012. – Proefschrift.

A catalogue record is available from the Eindhoven University of Technology Library

ISBN: 978-90-386-3211-7

NUR 924

Marangoni flows induced by non-uniform surfactant distributions

PROEFSCHRIFT

ter verkrijging van de graad van doctor aan de
Technische Universiteit Eindhoven, op gezag van de
rector magnificus, prof.dr.ir. C.J. van Duijn, voor een
commissie aangewezen door het College voor
Promoties in het openbaar te verdedigen
op donderdag 27 september 2012 om 16.00 uur

door

Myroslava Olehivna Hanyak

geboren te Chyshky, Oekraïne

Dit proefschrift is goedgekeurd door de promotor:

prof.dr. A. A. Darhuber

To Tiberiu

Contents

1	Introduction	1
1.1	Surfactants and interfacial flows	1
1.2	Outline of the thesis	3
2	Insoluble surfactant spreading at initially flat liquid-air interfaces	5
2.1	Introduction and system description for axisymmetric/planar spreading	5
2.1.1	Equation of state	6
2.2	Mathematical model based on lubrication approximation	7
2.3	Numerical results for axisymmetric spreading	9
2.3.1	Depleting surfactant supply	9
2.3.2	Continuous surfactant supply	13
2.3.3	Effect of different equation of state	18
2.4	Conclusions	21
3	Insoluble surfactant spreading at initially curved liquid-air interfaces	23
3.1	System description for spreading along rivulet interface	23
3.2	Mathematical model based on lubrication approximation	24
3.3	Results and discussion	27
3.3.1	Finite surfactant supply	27
3.3.2	Continuous surfactant supply	31
3.4	Summary and conclusions	37
4	Soluble surfactant spreading at initially curved liquid-air interfaces	39
4.1	Introduction and system description for spreading along rivulet interface	39
4.1.1	Equation of state	39
4.2	Mathematical model based on lubrication approximation and assumption of fast vertical diffusion	41

4.2.1	Initial and boundary conditions for continuous surfactant supply	43
4.2.2	Initial and boundary conditions for finite surfactant supply	46
4.3	Numerical results and discussion	46
4.3.1	Finite surfactant supply	46
4.3.2	Continuous surfactant supply	49
4.3.3	Effect of pre-contamination	54
4.4	Summary and conclusions	56
5	Slow-diffusion soluble surfactant spreading at initially flat liquid-air interfaces	59
5.1	System description for 1D rectilinear spreading	59
5.2	Model with the Arbitrary Lagrangian-Eulerian method	60
5.3	Weak-diffusion lubrication model	62
5.4	Results and discussion: Effect of vertical concentration profile	64
5.5	Summary and conclusions	67
6	Soluble surfactant spreading at liquid-liquid interfaces	69
6.1	System description	69
6.2	Governing equations and boundary conditions	71
6.2.1	Lubrication model	71
6.2.2	Model with Arbitrary Lagrangian-Eulerian method	72
6.3	Results and discussion	75
6.4	Summary and conclusions	81
7	Surfactant-induced delay of leveling of inkjet-printed patterns	83
7.1	Introduction and system description	83
7.2	Theoretical models and numerical simulations	86
7.2.1	Insoluble surfactants	86
7.2.2	Perturbation analysis for small amplitudes and insoluble surfactants	88
7.2.3	Soluble surfactants	90
7.3	Results and discussion	92
7.3.1	Leveling dynamics	92
7.3.2	Redistribution time of inkjet printed multi-lines	96
7.3.3	Implications for printing process windows	96
7.4	Summary	98
8	Conclusions and outlook	99
A	Derivation of lubrication equations for thin liquid films	103
	Bibliography	107
	List of publications	117

<i>CONTENTS</i>	iii
Summary	119
Acknowledgements	123
Curriculum vitae	125

Chapter 1

Introduction

1.1 Surfactants and interfacial flows

Surface active agents or surfactants are amphiphilic compounds that consist of a hydrophilic head and a hydrophobic tail. They may act as detergents, wetting agents, emulsifiers, foaming agents or dispersants. Due to their amphiphilic structure, surfactants tend to accumulate at interfaces, as shown schematically in Fig. 1.1, which leads to a reduction of the surface or interfacial tension. An example of a surfactant is oleic acid, which is a fatty acid insoluble in water occurring in many vegetable oils.

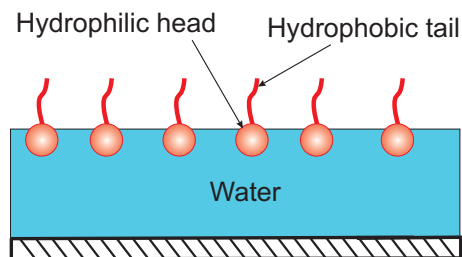


Figure 1.1: Schematic of surfactant molecules adsorbed at a liquid-air interface.

A great variety of surfactants is used in a wide range of industrial processes ranging from printing and coating processes [1], pulmonary drug delivery [2] to crude oil recovery [3].

In the context of oil recovery, the injection of surfactant solutions is considered a potential means for increasing the extraction efficiency from sub-surface oil reservoirs [4, 5], as surfactant induced reductions of interfacial tension facilitate deformations of oil-brine interfaces and therefore oil extraction.

Another application of surfactants is in the area of inkjet printing [114, 115, 116, 117, 118, 119, 120, 121, 122], where they lower surface tension of water-based ink solutions.

In the processes mentioned above, a non-uniform deposition gives rise to surfactant concentration gradients. Non-uniform concentrations at fluid-fluid interfaces give rise to interfacial tension gradients and associated Marangoni stresses that drive the liquid from the regions of lower surface to the regions of higher surface tension [6, 7, 8, 9, 10, 11, 12, 13, 14, 15, 16, 17, 18, 19, 20, 21, 22, 23, 24, 25, 26, 27, 73, 74, 75, 34, 35, 76, 77, 78, 55, 79, 54, 27, 80]. This type of flow is named after Carlo Marangoni who described them for the first time in 1872.

During surfactant-induced Marangoni flows, it was observed that film thinning occurred in the vicinity of the deposited surfactant and that a pronounced rim was formed near the surfactant leading edge [9, 10, 11, 12, 13]. The rim position $x_{\text{rim}}(t)$ follows a power law behavior $x_{\text{rim}} \sim t^\alpha$, where α is the so-called spreading exponent. A variety of spreading exponents were reported for different material systems and geometrical configurations: $\alpha = 0.5$ for planar spreading [9, 10], exponents around $\alpha = 0.25$ for axisymmetric spreading with large Peclet numbers [13, 14]. Only one systematic experimental study was done for surfactant spreading at liquid-liquid interface, and it was limited to a flat interface between deep, immiscible fluid layers with observed spreading exponents around $\alpha = 3/4$ [54]. The occurrence of a fingering instability at the spreading edge of surfactant droplet deposited on a thin liquid film was reported by Troian *et al.* [11].

Very few numerical studies provide direct comparison with the experimental results. The use of lubrication model for insoluble surfactants spreading at flat surfaces yields promising results when compared with the experimental data [14, 21, 28]. The use of lubrication model for soluble surfactant spreading is limited to systems with very fast vertical diffusion across the film thickness [16, 75]. Even for relatively thin films, a comparison with experiments is often not possible due to the fact that used surfactants diffuse relatively slow.

The motivation of the work presented in this thesis is twofold. First, we aim to perform a systematic quantitative study, which has rarely been done in the context of surfactant spreading, comparing numerical results with experimental data whenever possible. Second, we want to elucidate the impact of spatial confinement, achieved experimentally by chemical patterning, on the dynamics of surfactant spreading.

We have conducted an extensive numerical study of surfactant spreading dynamics for different geometries and material systems, which includes soluble and insoluble surfactants spreading at liquid-air and liquid-liquid interfaces. We monitored the spatio-temporal evolution of the liquid height profiles after non-uniform surfactant deposition at the interface. We have studied the effects of spatial confinements and different types of surfactant supply on the spreading dynamics.

The work presented in the thesis has been part of the "Surfactant-assisted enhanced oil recovery" project, for which numerical and experimental aspects have

been separated into two sub-projects. The two parts were carried out simultaneously providing a unique opportunity for a detailed comparison of numerical models with experiments.

1.2 Outline of the thesis

This section presents the organization of the thesis. Each chapter is briefly described in one paragraph, emphasizing the most important ideas and findings.

Chapter 2 describes the axisymmetric spreading dynamics of insoluble surfactants on thin liquid films. Numerical simulations based on the lubrication approximation and a non-linear equation of state compare very favorably with experimental results reported in the literature for oleic acid spreading on glycerol. A fingering instability was observed, which has a direct influence by increasing the spreading exponent.

Chapter 3 presents insoluble surfactant spreading on curved liquid-air interfaces. The spreading exponents determined from a model implementing a continuous supply of surfactant compare favorably with experimental data. We found that the initial film thickness has little effect on the spreading exponents for spreading at rivulet interfaces. The lateral confinement induces non-uniform height- and surface velocity profiles, which manifest themselves in a pronounced transition of the evolving rivulet morphology.

Chapter 4 contains the study of soluble surfactant spreading on curved liquid-air interfaces. Our numerical model is based on the lubrication approximation and the assumption of vertically uniform concentration profiles. A proper choice of initial and boundary conditions in the numerical models results in spreading exponents that are in excellent agreement with the experimental results for sodium dodecyl sulfate spreading on narrow glycerol rivulets.

Chapter 5 deals with the spreading of a soluble slow-diffusion surfactant along liquid-air interfaces. We present a model based on the full Navier-Stokes equation and convection-diffusion equations, which allows for vertically non-uniform concentration profiles.

Chapter 6 analyzes the spreading of a soluble surfactant at liquid-liquid interfaces. We consider an interface with initially uniform height as well as narrow rivulets. A model accounting for vertically non-uniform concentration profiles is used for slow-diffusion surfactants; a model based on the lubrication approximation corresponding to vertically uniform concentration profiles is applied in the case of sufficiently large diffusion coefficients.

Chapter 7 studies leveling and redistribution dynamics of inkjet-printed lines in the presence of soluble and insoluble surfactants. We present numerical results as well as scaling relations for both the leveling and redistribution times of sinusoidal ripples and multi-lines.

In Chapter 8 we discuss conclusions and our outlook on possible future studies.

Chapter 2

Insoluble surfactant spreading at initially flat liquid-air interfaces

2.1 Introduction and system description for axisymmetric/planar spreading

Marangoni stress driven spreading of an insoluble surfactant on flat liquid-air interfaces is the most elementary system to begin with in the investigation of spreading dynamics. It is therefore an often studied subject as evident from the literature [9, 10, 11, 12, 13, 14, 15, 16, 17, 30, 29, 18, 19, 20, 21, 31, 22, 32, 23, 24, 33, 35, 25, 28, 26, 36, 37]. We contribute to this list of references with few new findings. In this chapter we discuss how initial conditions, i. e. the presence of macroscopic droplet, affect the surfactant spreading. If the sub-phase liquid becomes trapped under the surfactant droplet, it is later expelled in the form of fingering instability. We observe the effects an expulsion of the liquid trapped in the deposition area has on the spreading dynamics.

We consider one-dimensional spreading of an insoluble surfactant on a thin Newtonian liquid film of the initially uniform height h_0 . Depending on the shape of the deposited surfactant two types of spreading are studied: axisymmetric and planar. In the case of axisymmetric spreading we assume that the surfactant is deposited as a drop of radius L_0 , see Fig. 2.1, and we adopt a cylindrical coordinates system (r, θ, z) with the origin at the solid-liquid interface on the symmetry axis of the surfactant droplet. In the case of planar spreading, the surfactant is deposited as a strip of width $2L_0$ and infinite length, and we adopt rectilinear coordinates (x, y, z) .

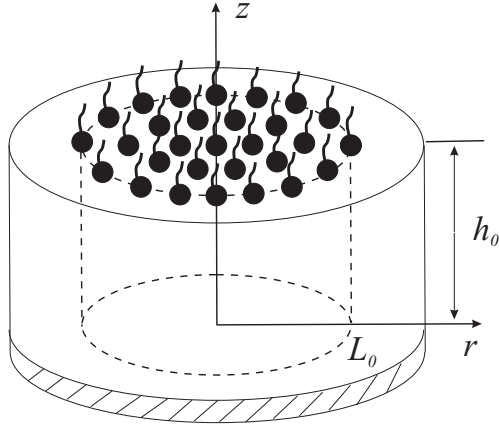


Figure 2.1: Schematic presentation of the geometry

An important characteristic of the system is that the aspect ratio $\epsilon = h_0/L_0 \ll 1$ is very small, i. e. lateral length-scale are much longer than h_0 , thus the so-called lubrication approximation can be applied. Non-uniform surfactant distributions at fluid-fluid interfaces give rise to interfacial tension gradients and associated Marangoni stresses, which locally cause flow from regions of lower to regions of higher interfacial tension.

2.1.1 Equation of state

Since concentration gradients and, consequently, Marangoni stresses are driving forces of the spreading, experimental data is needed in order to determine the relation between surface tension γ and surfactant concentration Γ . Our system of choice is glycerol and oleic acid, which is a surface-active substance that is practically insoluble in glycerol [14].

Gaver and Grotberg [14] measured the relation between surface tension γ and the surfactant surface concentration Γ for oleic acid on glycerol. The surface tension drops from the value $\gamma_0 = \gamma(\Gamma = 0) = 63.5 \text{ mN/m}$ to $\gamma_m = \gamma(\Gamma \rightarrow \infty) = 39 \text{ mN/m}$. The measured data points are often fitted with linear relation, but this fit poorly represents the data. Fitting the data with the following nonlinear equation of state, we obtain an excellent fit

$$\gamma = \gamma_m + \Pi_{\max} \exp(-A\Gamma^2) \quad (2.1)$$

where $\Pi_{\max} = \gamma_0 - \gamma_m$ is the maximum spreading pressure, and $A = 0.5 \text{ m}^4/\mu\text{l}^2$ is a fitting parameter. The point where the surface tension curve approximately reaches its asymptotic value of γ_m is defined as $\Gamma_c \equiv 3.5 \mu\text{l}/\text{m}^2$. Both the experimental data and resulting fit are shown in Fig.2.2.

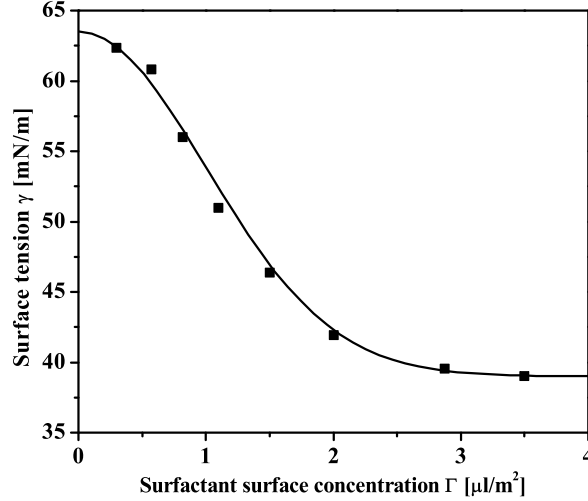


Figure 2.2: Dependence of the glycerol surface tension γ on the oleic acid surface concentration Γ . Experimental data [14] is indicated by triangles. The continuous line is a fit according to $\gamma = \gamma_m + \Pi_{\max} \exp(-\bar{A}\Gamma^2/\Gamma_c^2)$ with fit parameter $\bar{A} = 6.125$.

2.2 Mathematical model based on lubrication approximation

We perform model calculations for axisymmetric spreading by coupling the lubrication equation for thin film flow with the equation for surfactant surface transport by convection and diffusion [38, 39, 11, 12, 13]. The derivation of these equations can be found in Appendix A. In addition, we include the non-linear equation of state (EOS) Eq. (2.1) in the system, presented for oleic acid and glycerol in the previous section. For an insoluble surfactant of small molecular size and irregular conformation such as oleic acid, kinetic and dynamic effects due to adsorption/desorption or intermolecular surface interactions are absent or weak. Therefore, this equilibrium relation is expected to be valid for the dynamic surface tension as well, i.e. γ only depends on the local surfactant concentration, but not the velocity profile or previous system configurations.

The theoretical model does not consider the presence of the surfactant droplet, which is small compared to the capillary length $R_0 < l_{\text{cap}} \equiv \sqrt{\gamma/\rho g}$. Rather, it is approximated by a localized initial distribution of surfactant on the surface of an initially flat sub-phase film of thickness h_0 .

We introduce the following dimensionless variables: $\bar{r} \equiv r/R_0$, $\bar{h} \equiv h/h_0$, $\bar{\Gamma} \equiv \Gamma/\Gamma_c$, as well as

$$\bar{t} \equiv \frac{t}{t_M} \equiv t \frac{h_0 \Pi_{\max}}{\mu R_0^2} \quad \text{and} \quad \bar{p} \equiv \frac{p R_0^2}{h_0 \Pi_{\max}} \quad (2.2)$$

where h is the film height and p is the augmented pressure. The timescale t_M is chosen as the ratio of R_0 and the Marangoni velocity $h_0\tau/\mu \sim h_0\Pi_{\max}/(\mu R_0)$. Using the scales introduced above, the following system of coupled equations can be derived for axisymmetric spreading

$$\frac{\partial \bar{h}}{\partial \bar{t}} + \frac{1}{\bar{r}} \frac{\partial}{\partial \bar{r}} \left[\frac{\bar{r} \bar{h}^2}{2} \frac{\partial \bar{\gamma}}{\partial \bar{\Gamma}} \frac{\partial \bar{\Gamma}}{\partial \bar{r}} - \frac{\epsilon^2}{3} \bar{r} \bar{h}^3 \frac{\partial \bar{p}}{\partial \bar{r}} \right] = 0 \quad (2.3)$$

$$\frac{\partial \bar{\Gamma}}{\partial \bar{t}} + \frac{1}{\bar{r}} \frac{\partial}{\partial \bar{r}} \left[\bar{r} \bar{h} \bar{\Gamma} \frac{\partial \bar{\gamma}}{\partial \bar{r}} - \frac{\epsilon^2}{2} \bar{r} \bar{\Gamma} \bar{h}^2 \frac{\partial \bar{p}}{\partial \bar{r}} - \frac{\bar{r}}{\text{Pe}_s} \frac{\partial \bar{\Gamma}}{\partial \bar{r}} \right] = 0 \quad (2.4)$$

$$\bar{p} = \text{Bo} \bar{h} - \frac{\bar{\gamma}}{\bar{r}} \frac{\partial}{\partial \bar{r}} \left(\bar{r} \frac{\partial \bar{h}}{\partial \bar{r}} \right) \quad (2.5)$$

$$\bar{\gamma} = \frac{\gamma}{\Pi_{\max}} = [\gamma_m + \Pi_{\max} \exp(-\bar{A} \bar{\Gamma}^2)] / \Pi_{\max} \quad (2.6)$$

where $\epsilon \equiv h_0/R_0$, $\text{Bo} \equiv \rho g R_0^2 / \Pi_{\max}$ is the Bond number, $\bar{A} \equiv A \Gamma_c^2$ is a constant, $\text{Pe}_s \equiv h_0 \Pi_{\max} / (\mu D_s)$ is the Peclet number for surface transport, and D_s is the surface diffusion coefficient.

On the other hand, planar spreading is described by the following system

$$\frac{\partial \bar{h}}{\partial \bar{t}} + \frac{\partial}{\partial \bar{x}} \left[\frac{\bar{h}^2}{2} \frac{\partial \bar{\gamma}}{\partial \bar{\Gamma}} \frac{\partial \bar{\Gamma}}{\partial \bar{x}} - \frac{\epsilon^2}{3} \bar{h}^3 \frac{\partial \bar{p}}{\partial \bar{x}} \right] = 0 \quad (2.7)$$

$$\frac{\partial \bar{\Gamma}}{\partial \bar{t}} + \frac{\partial}{\partial \bar{x}} \left[\bar{h} \bar{\Gamma} \frac{\partial \bar{\gamma}}{\partial \bar{x}} - \frac{\epsilon^2}{2} \bar{\Gamma} \bar{h}^2 \frac{\partial \bar{p}}{\partial \bar{x}} - \frac{1}{\text{Pe}_s} \frac{\partial \bar{\Gamma}}{\partial \bar{x}} \right] = 0 \quad (2.8)$$

$$\bar{p} = \text{Bo} \bar{h} - \bar{\gamma} \frac{\partial}{\partial \bar{x}} \left(\frac{\partial \bar{h}}{\partial \bar{x}} \right) \quad (2.9)$$

$$\bar{\gamma} = \frac{\gamma}{\Pi_{\max}} = [\gamma_m + \Pi_{\max} \exp(-\bar{A} \bar{\Gamma}^2)] / \Pi_{\max} \quad (2.10)$$

The boundary conditions are

$$\frac{\partial \bar{\Gamma}}{\partial \bar{r}}(0, \bar{t}) = 0, \quad \frac{\partial \bar{h}}{\partial \bar{r}}(0, \bar{t}) = 0, \quad \frac{\partial \bar{p}}{\partial \bar{r}}(0, \bar{t}) = 0, \quad (2.11)$$

$$\bar{\Gamma}(+\infty, \bar{t}) = \bar{\Gamma}_d, \quad \bar{h}(+\infty, \bar{t}) = 1, \quad \bar{p}(+\infty, \bar{t}) = 0, \quad (2.12)$$

where $+\infty$ represents the right boundary of the computational domain, which is large enough such that the end point does not affect the spreading dynamics.

The initial conditions for the surfactant distribution used in the numerical simulations are sketched in Fig. 2.3(a). Two cases are considered

$$\bar{\Gamma}(\bar{r}, \bar{t}=0) = \begin{cases} f(\bar{r}) + \bar{\Gamma}_d & \text{(case I)} \\ 6f(\bar{r}) + \bar{\Gamma}_d & \text{(case II)} \end{cases} \quad (2.13)$$

where

$$f(\bar{r}) \equiv \frac{1}{2} (\tanh [10(1 - \bar{r})] + 1) \quad (2.14)$$

is used to provide a smooth and continuous variation of $\bar{\Gamma}$ at $\bar{r}=1$. The parameter $\bar{\Gamma}_d$ accounts for a pre-existing homogeneous contamination of the subphase with a surface-active material. For simplicity, we assume that the EOS and surface diffusion coefficient of the contaminant are identical to that of oleic acid. The initial condition for the height profile was a flat film $\bar{h}(\bar{r}, \bar{t}=0) = 1$ in both cases. For planar spreading case, the only modification needed in the boundary and initial conditions is replacing r with x .

The initial condition $\bar{\Gamma}(\bar{r}=0, \bar{t}=0) > 1$ can be viewed as a simple model for a highly compressed surfactant monolayer or an ultrathin "bulk" layer of oleic acid with thickness in order of 6 molecules. This initial condition increases the amount of surfactant present in the deposition region compared to the case $\bar{\Gamma}(\bar{r}=0, \bar{t}=0) = 1$ and, thus, mimics experiments with a very small surfactant source that depletes during the course of the experiment. It does not, however, consider any effects caused by the existence of the three-phase contact line at the edge of the droplet or the liquid-liquid interface between droplet and sub-phase. Due to the finite value of $\bar{\Gamma}(0, 0)$, the surfactant is depleted and $\bar{\Gamma}(0, \bar{t})$ falls below one after a certain dimensionless time \bar{t}_c , at which we expect a transition in the spreading behavior from the case of an infinite to a finite surfactant source.

We solve the system of equations (2.3-2.6), taking into account boundary and initial conditions, numerically with the finite element software Comsol Multiphysics 3.5 using transient analysis for the general form PDE equation mode.

2.3 Numerical results for axisymmetric spreading

2.3.1 Depleting surfactant supply

Since the surface tension of the sub-phase liquid in the surfactant deposition area is lower than the surface tension of an uncontaminated liquid, Marangoni stresses are induced. These stresses lead to film thinning in the vicinity of the deposited surfactant droplet and the formation of an advancing rim. After an initial growth phase, the rim broadens as time progresses and its height decreases.

The time evolution of the film height profiles is shown in Figs. 2.3(b,c) for $Pe_s = 5 \cdot 10^4$, $\epsilon = 0.01$, and the two initial conditions [Eqs. (2.13,2.14)] considered. In the first case, the film thickness at the origin $\bar{r}=0$ decreases rather immediately. In the second case $\bar{h}(0, \bar{t})$ remains at or above 1 for more than 60 dimensionless time units and a ridge develops at $\bar{r} \approx 1$, which subsequently widens and moves inwards. In the second case, the speed of advance of the rim is significantly higher than in the first case.

Figure 2.4 presents the rim position \bar{r}_{rim} as a function of the dimensionless time. The rim position exhibits a power law behavior, $\bar{r}_{rim}(t) \sim \bar{t}^\alpha$, where the parameter α is called spreading exponent. For case II and $\bar{t} < 200$ a power law behavior with exponent $\alpha \approx 0.284$ is observed. After $\bar{t} \approx 200$ the slope of \bar{r}_{rim} levels off and is comparable for both cases considered. The dotted line in Fig. 2.4 corresponds to

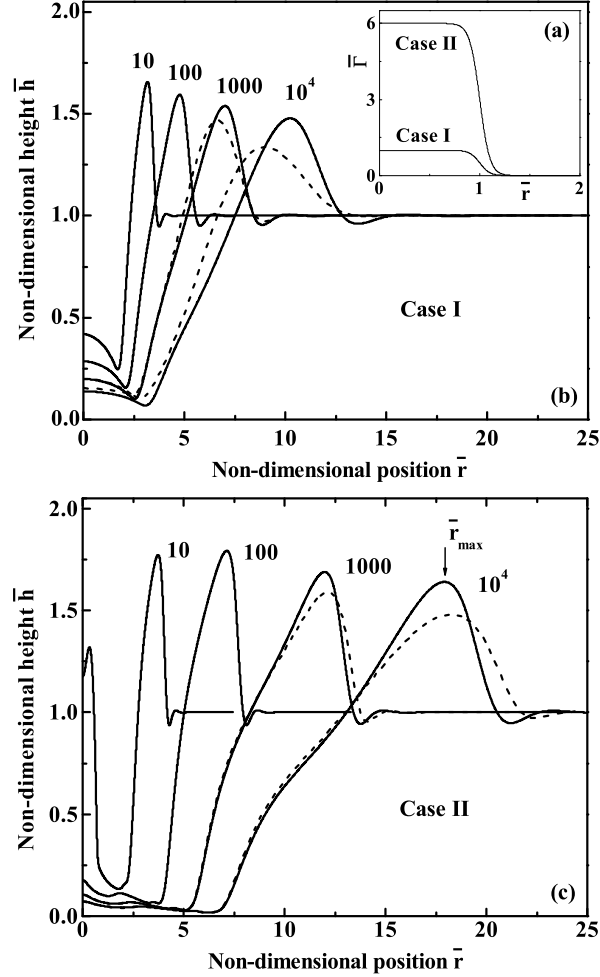


Figure 2.3: Model calculations for axisymmetric spreading of oleic acid on thin glycerol films assuming $Pe_s = 50000$, $\epsilon = 0.01$ and $\bar{\Gamma}_d = 0$ unless noted otherwise. (a) Initial surfactant distribution for two cases considered: $\bar{\Gamma}(\bar{r}=0, \bar{t}=0) = 1$ (case I) and $\bar{\Gamma}(0, 0) = 6$ (case II). (b) Time evolution of the height profile $\bar{h}(\bar{r}, \bar{t})$ for case I. The dashed lines correspond to solutions for $Pe_s = 1000$. (c) Time evolution of $\bar{h}(\bar{r}, \bar{t})$ for case II. The dashed lines correspond to solutions for $\bar{\Gamma}_d = 0.002$.

Case I and a hypothetically linear equation of state $\gamma = [\gamma_m + \Pi_{max}(1 - \Gamma/\Gamma_c)]$, for which $\partial\bar{\gamma}/\partial\bar{\Gamma} = -1$ is constant. The deviations from the solution for a realistic non-linear equation of state are significant. The slope of the dotted line corresponds to a spreading exponent of $1/4$.

The dashed lines in Fig. 2.3(b) correspond to $Pe_s = 1 \cdot 10^3$, which illustrates that

increased surface diffusion reduces both h_{\max} and the depth of the local minimum in the height profile ahead of the rim. The dashed lines in Fig. 2.3(c) correspond to $\bar{\Gamma}_d = 0.002$, whereas all other simulations in Fig. 2.3 have been obtained assuming $\bar{\Gamma}_d = 0$. This shows that a pre-existing contamination of the sub-phase has a similar effect on $\bar{h}(\bar{r}, \bar{t})$ as a reduction of Pe_s , even if the level of contamination is so low that it would be almost undetectable with a Wilhelmy plate technique. Dussaud *et al.* [28] suggested that contamination should improve the correspondence of the rim heights \bar{h}_{\max} with those experimentally observed.

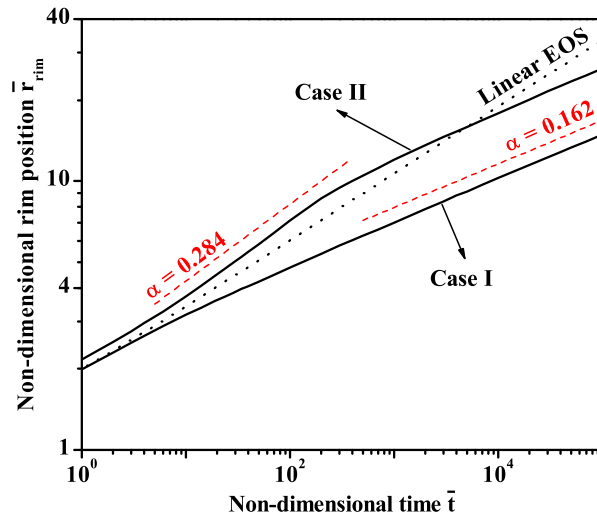


Figure 2.4: Time evolution of the rim position $\bar{r}_{\text{rim}}(t)$. The dotted line labeled 'Linear EOS' corresponds to case I with a hypothetical linear equation of state $\gamma = (\gamma_0 - \Pi_{\max}\bar{\Gamma})$ resulting in a spreading exponent of 0.25.

We choose the axisymmetric spreading of oleic acid on glycerol reported in [43] for a comparison of the numerical results with the experimental data. During the experiments, liquid films of variable thickness were deposited on Si wafers, with a diameter of 10 cm, by means of spin-coating. The films were initially flat and of uniform thickness h_0 between 0.2 and 10 μm . Oleic acid droplets, with the volume ranging from 0.2 to 100 nl, were deposited on the liquid films using dip-pen or a droplet-on-demand inkjet system with a capillary nozzle diameter of 70 μm . The time evolution of the film thickness $h(r, t)$ was monitored using interference microscopy.

In Fig. 2.4 case II numerical results for $\bar{t} < 200$ yield a power law behavior with exponent $\alpha \approx 0.284$, which is in good agreement with the experimental power law exponents shown in Fig. 2.5(a). After $\bar{t} \approx 200$ the slope of \bar{r}_{rim} levels off and is comparable for both cases considered. The situation corresponds exactly to the second curve in Fig. 2.5(a), where the surfactant droplet is depleted at $t \approx 350$ s,

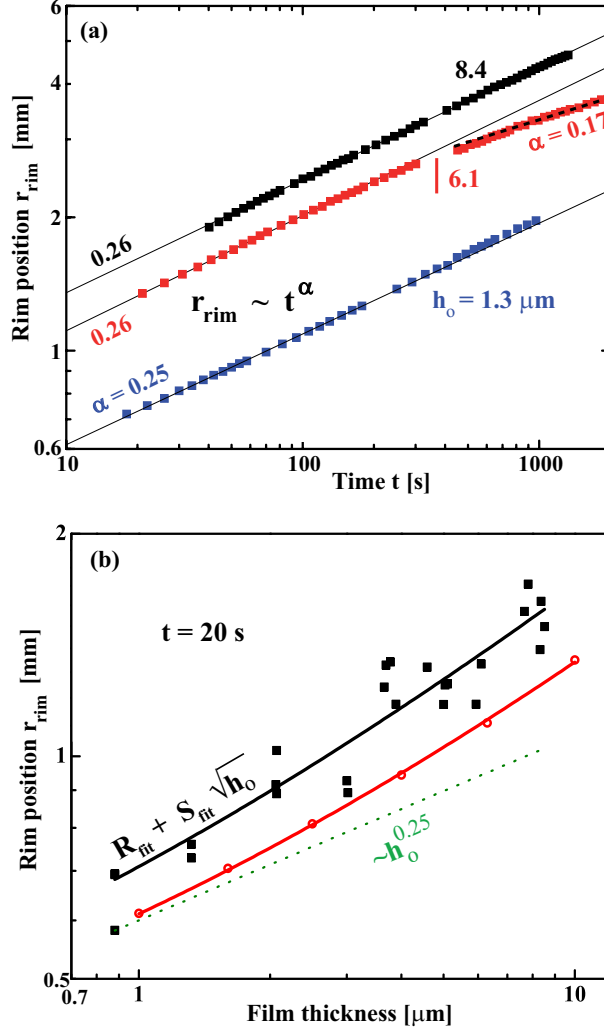


Figure 2.5: (a) Time dependence of the experimentally obtained rim radius $r_{\max}(t)$ for three different values of h_0 . The straight lines correspond to power law relations $r_{\text{rim}} \sim t^\alpha$. Image taken from [43], courtesy of David Sinz. (b) Rim position $r_{\max}(t=20\text{ s})$ as a function of h_0 . Experimentally and numerically obtained values are shown by closed squares and open circles, respectively. The black and red solid lines correspond to the function $r_{\max}(t=20\text{ s}) = R_{\text{fit}} + S_{\text{fit}}\sqrt{h_0}$ with fit parameters R_{fit} and S_{fit} . The green dotted line corresponds to a power law relation $r_{\max}(t=20\text{ s}) \sim h_0^{0.25}$

after which the slope of $r_{\text{rim}}(t)$ decreases markedly. The value of the predicted spreading exponent $\alpha = 0.16$ agrees very well with the experimental value 0.17 shown in Fig. 2.5(a).

Figure 2.5(b) presents numerical results (red squares) for the dependence of $r_{\max}(t=20\text{ s})$ on the initial film thickness h_0 with a value of $R_0 = 255\ \mu\text{m}$, which is the average droplet radius observed experimentally [67]. The scatter in the experimental data (black squares) is mainly due to variations in the surfactant droplet radius R_0 . Assuming constant net change in surface tension from the droplet position to the rim, $\Delta\gamma$, we can derive a scaling relation for the dependence of r_{rim} on h_0

$$\frac{dr}{dt} = \frac{h_0\Delta\gamma}{\mu(r - R_{\text{av}})} \quad \longrightarrow \quad r = R_{\text{av}} + \sqrt{2\frac{h_0\Delta\gamma}{\mu}t} \quad (2.15)$$

which yields the power law relation $r_{\text{rim}} \sim h_0^{1/2}$.

The red and black lines in Fig. 2.5(b) correspond to the function $r_{\text{rim}} = R_{\text{fit}} + S_{\text{fit}}\sqrt{h_0}$ with fit-parameters R_{fit} and S_{fit} . The numerical data is well described by the same scaling relation as the experimental data except for an offset in the slope S_{fit} . This offset is most likely related to a viscosity reduction of the glycerol in the experiments due to water uptake from the ambient air. Shown by the green dotted line is the power-law relation $r_{\text{rim}} \sim h_0^{0.25}$ which visibly deviates from the experimental and numerical data.

2.3.2 Continuous surfactant supply

During experiments the deposited surfactant quantity is often large and does not deplete as fast as in the finite supply model [43]. In an attempt to model this, we consider the solutions of Eqs. (2.3)-(2.6) for which the surfactant concentration is kept constant for $\bar{r} < 1$

$$\bar{\Gamma}(\bar{r} \leq 1) = \bar{\Gamma}_0 = \text{const} \quad (2.16)$$

Moreover, to account for the presence of the surfactant droplet, we added a pressure offset to Eq. (2.5) in the region $\bar{r} \leq 1$

$$\bar{p}(\bar{r} \leq 1) = \text{Bo}\bar{h} - \frac{\bar{\gamma}}{\bar{r}} \frac{\partial}{\partial \bar{r}} \left(\bar{r} \frac{\partial \bar{h}}{\partial \bar{r}} \right) + \bar{p}_{\text{offset}} \quad (2.17)$$

where

$$\bar{p}_{\text{offset}} \equiv \left(\rho g h_{\text{OA}} + \frac{2\gamma_{\text{OA}}}{R_1} \right) \frac{R_0^2}{\Pi_{\text{max}} h_0} \quad (2.18)$$

$$h_{\text{OA}} \equiv \sqrt{R_1^2 - R_0^2 \bar{r}^2} - \sqrt{R_1^2 - R_0^2}, \quad (2.19)$$

with $R_1 \equiv R_0/\sin\theta$ and γ_{OA} being oleic acid surface tension. Equation (2.18) accounts for the capillary and hydrostatic pressure that is exerted by a droplet of surfactant placed on top of the thin film of sub-phase liquid. The contact angle θ of the surfactant droplet was estimated to be 10° . These modifications are intended to more closely account for the presence of a *macroscopic* surfactant

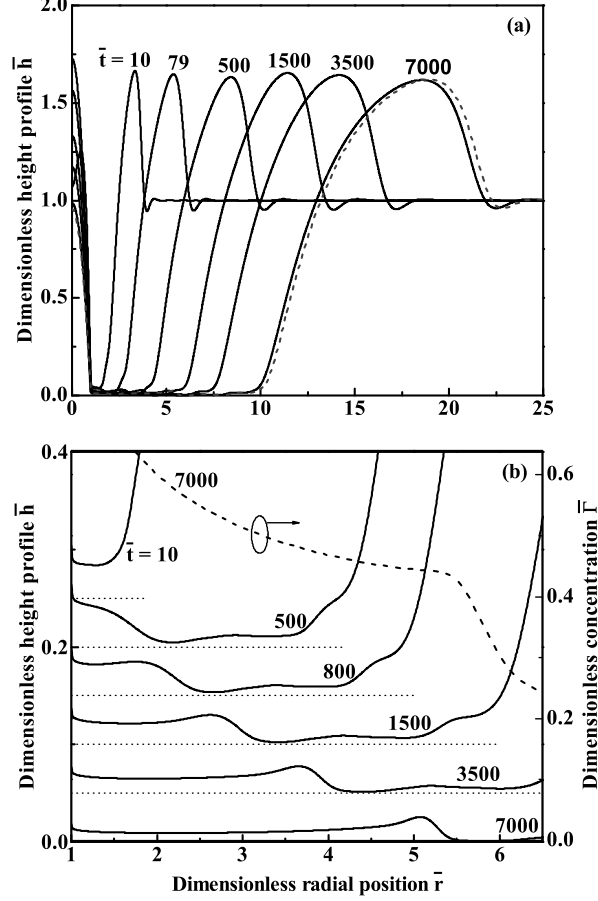


Figure 2.6: (a) Time evolution of the height profile $\bar{h}(\bar{r}, \bar{t})$ for $h_0 = 3 \mu\text{m}$, $R_0 = 250 \mu\text{m}$, $\text{Pe}_s = 2.5 \cdot 10^4$, and $\bar{\Gamma}_d = 0.002$. (b) Zoom of (a) in the crater region. For clarity, curves corresponding to different times were shifted consecutively by 0.05 along the ordinate. Dotted horizontal lines denote the solid surface $\bar{z} = 0$ for each solution. The dashed curve is the dimensionless concentration $\bar{\Gamma}(\bar{t} = 7000)$.

droplet deposited on the liquid film. They do not, however, faithfully represent local effects caused by the existence of the three-phase contact line at the edge of the droplet.

Figure 2.6 presents a time series of the height profile $\bar{h}(\bar{r}, \bar{t})$ for $h_0 = 3 \mu\text{m}$, $R_0 = 250 \mu\text{m}$, $\bar{p}_{\text{offset}} = 0$ and $\bar{\Gamma}(\bar{r} \leq 1, \bar{t}) = 1$. For $\bar{t} \lesssim 15$ a rim in $\bar{h}(\bar{r}, \bar{t})$ is observed at $\bar{r} \approx 1$, which subsequently moves inwards and disappears under the influence of capillary pressure. At $\bar{t} \approx 400$ a small 'bump' in the height profile appears at $\bar{r} \approx 1$, which develops into a thin film that is expelled from underneath the

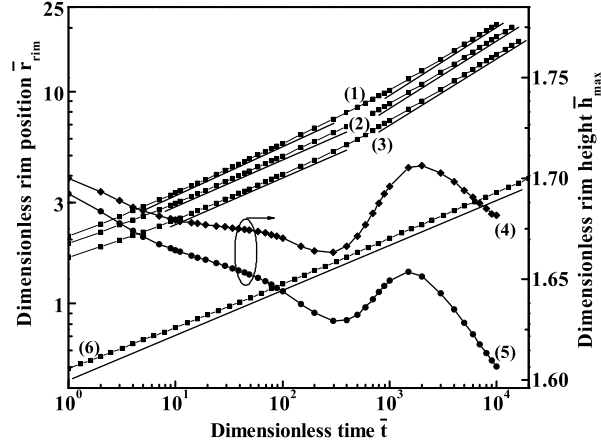


Figure 2.7: Rim position \bar{r}_{rim} and height $\bar{h}(\bar{r}_{\text{rim}})$ extracted from the simulations in (a) [curve (1)] and equivalent ones for $\bar{\Gamma}(\bar{r} \leq 1, \bar{t}) = 0.5$ [curve (2)] and $\bar{\Gamma}(\bar{r} \leq 1, \bar{t}) = 0.25$ [curve (3)]. Solid lines correspond to power-laws $\bar{r}_{\text{rim}} \sim \bar{t}^\alpha$ with $\alpha = 0.22$ and 0.32 . Curves (4,5) track the rim height for the data in (a) [curve (5)] and a smaller value of $\bar{\Gamma}_d = 0.001$ with all other parameters unchanged [curve (4)]. Curve (6) illustrates $r_{\text{rim}}(t)$ for $D_s = 0$ and a boundary condition $\bar{\Gamma}(\bar{r} = 0, \bar{t}) = 1$ representing surfactant supply only from a *point* source. No expulsion is observed. The resulting spreading exponent $\alpha = 0.21$ remains constant in time.

surfactant droplet. A magnified view of the height profile in the crater region is presented in Fig. 2.6(b). The front of this film exhibits a ridge similar in shape to films spreading under the action of thermocapillary stresses, which are known to undergo a fingering instability [41, 42].

Fischer and Troian [40] considered the linear stability of thin film flows for the case of a step-like increase in the Marangoni stress $\tau_1 \rightarrow \tau_2$ with and without additionally assuming an initial step-like change in the height profile $h_1 \rightarrow h_2$. The flow was found to be unstable if a thicker film ($h_1 > h_2$) flows into a region of reduced thickness h_2 but increased Marangoni stress τ_2 . The predicted lateral wavelength corresponding to the most unstable mode scales as $\lambda \sim h_0(\tau_2/\tau_1)^{-1/2}$. Due to increased complexity, a simple expression for the instability wavelength for the full problem including surfactant bulk- and surface transport can not be given [25, 26, 36, 37]. The dashed curve in Fig. 2.6(c) corresponds to the concentration profile $\bar{\Gamma}(\bar{r})$ for the solution at time $\bar{t} = 7000$. As can be seen, $\bar{\Gamma}(\bar{r})$ has a very pronounced kink in the thinned region just ahead of the rim of the expelled film. The Marangoni stress in this region is approximately a factor of 20 higher than behind the rim and the film thickness decreases by more than a factor of 10. Therefore, the conditions of the instability criterion in the model of Fischer and Troian [40] are met and the film is unstable, consistent with Fig. 2.8.

If we consider a value of the offset pressure $\bar{p}_{\text{offset}} \neq 0$ according to Eq. (2.18),

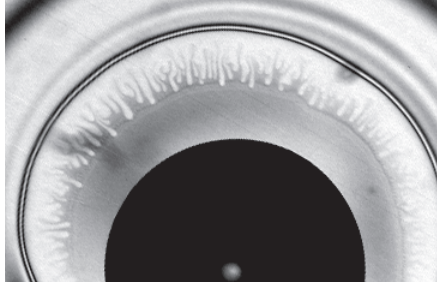


Figure 2.8: Unstable expulsion of glycerol trapped below an oleic acid droplet with $R_0 = 465 \mu\text{m}$. The thickness of the expelled film is below 100 nm. Image: courtesy of David Sinz [43].

the dashed curve in Fig. 2.6(a) results at time $\bar{t} = 7000$. This result differs very little from the solution obtained for $\bar{p}_{\text{offset}} = 0$ [solid line in Fig. 2.6(a)], which is also the case in the crater region and underneath the surfactant droplet. This indicates that the sub-phase transport is dominated by the Marangoni stresses and that the pressure exerted by the surfactant droplet does not substantially contribute for the values of ϵ and size of the droplet considered.

As illustrated by the dashed curve in Fig. 2.6(b), the surfactant concentration is significantly higher on top of the expelled film than in the region ahead of it. This implies that the expulsion process of the ultrathin film is very efficient in convecting "additional" surfactant across the crater region. It is therefore not surprising that this effect leads to an increase in both the slope of $\bar{r}_{\text{max}}(\bar{t})$ and the height of the rim \bar{h}_{max} as shown in Fig. 2.7. The non-dimensional rim height increases from about 1.66 to 1.71 around $\bar{t} = 800$ for curve (4). At the same time $\bar{r}_{\text{rim}}(\bar{t})$, which is well described by a powerlaw $\bar{r}_{\text{rim}} \sim \bar{t}^\alpha$ with $\alpha = 0.22$ over the interval $20 < \bar{t} < 200$, changes exponent towards $\alpha = 0.32$ after $\bar{t} \sim 700$.

Also shown in Fig. 2.7 is the rim position $\bar{r}_{\text{rim}}(\bar{t})$ for $\bar{\Gamma}(\bar{r}=0, \bar{t}) = 1$ and $D_s = 0$ [curve (6)]. For this system the expulsion, depicted in Fig. 2.6(b), was absent and the rim position could be approximated by $\bar{r}_{\text{rim}} \sim \bar{t}^\alpha$ with $\alpha = 0.21$ for the entire range shown (illustrated by the solid line). Experimentally it was found that the expulsion process, illustrated in Fig. 2.8, can increase the spreading exponent α by up to 0.15 [43]. The instability can be weakened or suppressed by reducing the surfactant droplet volume, i.e. by decreasing R_0 .

Analogous simulations for $\bar{\Gamma}(\bar{r} < 1, \bar{t}) = 0.25$ and 0.5 exhibit the same pre-expulsion power-law exponents of 0.22 and a corresponding jump in the rim height at $\bar{t} = 800$. For the boundary condition $\bar{\Gamma}(\bar{r} < 1, \bar{t}) = 0.25$, the highest Marangoni coefficient $\partial\gamma/\partial\Gamma$ occurs at the boundary value of the surfactant concentration, i.e. at $\bar{r} = 1$. On the other hand, for $\bar{\Gamma}(\bar{r} < 1, \bar{t}) = 0.5$ and 1, the stress maximum is assumed at a lower concentration of approximately $\bar{\Gamma} = 0.285$ for $\bar{A} = 6.125$, which

occurs ahead of the boundary in the crater region. Consequently, the fact that the shape evolution proceeds in a qualitatively identical fashion indicates that the precise functional form of the EOS is not crucial for the occurrence of the expulsion process and the ensuing fingering instability.

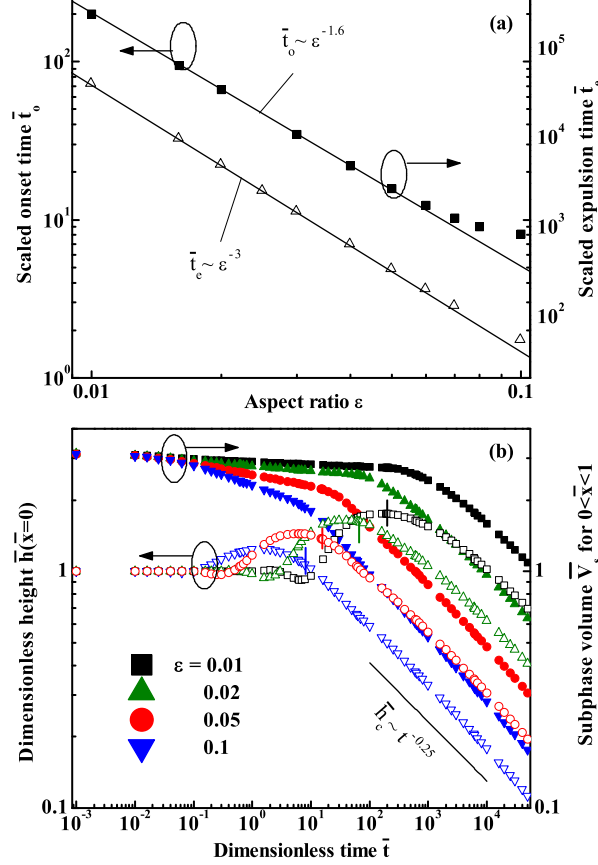


Figure 2.9: (a) Dimensionless onset \bar{t}_o and expulsion times \bar{t}_e as a function of ϵ . The solid and dashed lines correspond to power law relations with exponents -1.6 and -3, respectively. (b) Dimensionless height $\bar{h}(\bar{x} = 0)$ (open symbols) and subphase volume \bar{V}_s underneath the surfactant droplet for $0 < \bar{x} < 1$ (solid symbols) for different values of ϵ . The solid line corresponds to a power law relation with exponent -0.25. The onset times \bar{t}_o for the different aspect ratios are indicated by the vertical line segments.

In Fig. 2.9(a) we present the dimensionless onset time \bar{t}_o of the expulsion process as a function of ϵ . The parameter \bar{t}_o is defined as the time when the rate of increase of the local film thickness at the rim of the surfactant droplet ($\partial\bar{h}/\partial\bar{t})(\bar{r}=1)$ reaches the maximum. The solid line in Fig. 2.9(a) corresponds to a power law relation $\bar{t}_o \sim \epsilon^{-1.6}$, which translates into $t_o \sim R_0^{3.6}/h_0^{2.6}$. This scaling is rem-

inscent of the timescale for capillary leveling [44] of infinitesimal disturbances $t_{\text{Orchard}} \sim L^4/\langle h \rangle^3$, where L is the disturbance wavelength and $\langle h \rangle$ is the average film thickness. As exemplified in Fig. 2.6(a), the expulsion is indeed preceded by the profile of the trapped film evolving from initially flat $h(r, t = 0) = h_0$ to approximately a spherical cap shape.

Figure 2.9(b) shows the time evolution of the dimensionless center height $\bar{h}_c \equiv \bar{h}(\bar{x} = 0)$ and the sub-phase volume \bar{V}_s

$$\bar{V}_s \equiv 2\pi \int_0^1 \bar{r} \bar{h} d\bar{r} \quad (2.20)$$

underneath the surfactant droplet for different values of ϵ . The initial volume located underneath the surfactant droplet is $V_0 = \pi R_0^2 h_0$ or equivalently $\bar{V}_s(\bar{t} = 0) = \pi$. After the center-height reaches a maximum, the rate of volume loss shows a rapid increase. The vertical line segments indicate the onset times \bar{t}_o , which precede the regimes where $\bar{V}_s(\bar{t})$ and $\bar{h}_c(\bar{t})$ resemble power law behavior $\sim \bar{t}^{-0.25}$ as indicated by the solid line. Corresponding curves of $\bar{h}_c(\bar{t})$ and $\bar{V}_s(\bar{t})$ follow the same power law behavior, since the volume of a spherical cap of small aspect ratio is to a good approximation $V_{\text{cap}} = \pi R_0^2 h_c/2$, where R_0 is the base radius and h_c the center height; i.e. the sub-phase volume \bar{V}_s is proportional to the center height \bar{h}_c for droplet diameters below the capillary length.

We define the expulsion time \bar{t}_e as the instant when the sub-phase volume reaches a fraction of $1/e \approx 37\%$ of its initial value. In Fig. 2.9(a) \bar{t}_e is plotted as a function of aspect ratio ϵ (open symbols). The dashed line corresponds to a power law $\bar{t}_e \sim \epsilon^{-3}$.

2.3.3 Effect of different equation of state

We studied so far only one specific equation of state for dependence of surface tension on concentration. However, in industrial processes a variety of surfactants and sub-phase liquids is used. For instance, natural oil reservoirs are highly complex systems with multi-component mixtures, high temperatures and pressures. It is, therefore, essential to predict the effect of specific surfactant on spreading dynamics. In order to identify how different surfactant changes the spreading rates, we consider the following "generic" equations of state (EOS)

$$\gamma_1 = \gamma_m + \Pi_m \cos(8\bar{\Gamma}) \exp(-A\bar{\Gamma}^2) \quad (2.21)$$

$$\gamma_2 = \gamma_m + \Pi_m \exp(-A\bar{\Gamma}^2) \quad (2.22)$$

$$\gamma_3 = 15 + \frac{1}{2} \Pi_m (3 - \tanh[8(\bar{\Gamma} - 0.6)])^9 \quad (2.23)$$

Figure 2.10 shows plots of three surface tension functions defined in Eqs.(2.21-2.23). The initial condition for the surfactant distribution used here is corresponding to case I from Eq.2.13. While the maximum spreading pressure is similar for

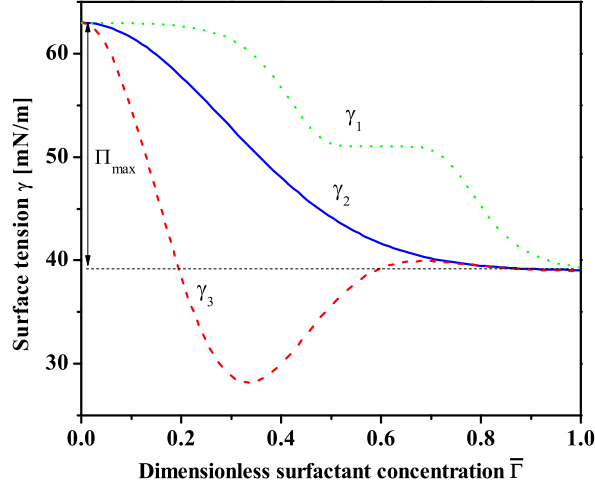


Figure 2.10: Equations of state that are defined in (2.17-2.19).

all three equations of state, the step-like behavior or reversed gradients may potentially affect the spreading dynamics.

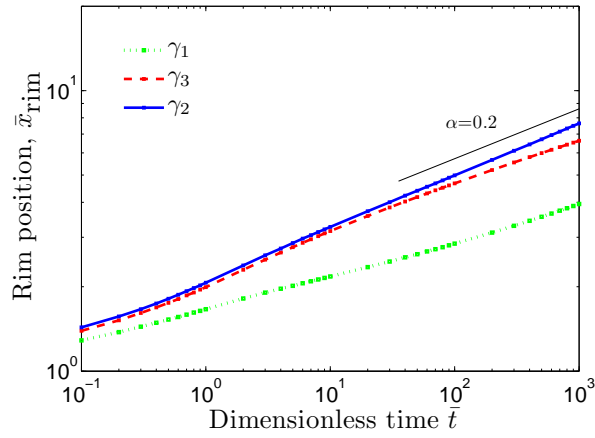


Figure 2.11: Effect of different equations of state, defined in (2.17-2.19), on the rim position.

Figure 2.11 illustrates the corresponding rim positions for 1D axisymmetric spreading with finite surfactant supply. The dotted line in Fig. 2.11, corresponding to γ_1 , is lower than two others because of the step-like EOS. The plateau regions leads to zero surface tension gradients for certain concentration intervals, thus reducing the spreading rate. The dashed line, corresponding to γ_3 , is lower than the solid line (oleic acid, γ_2) due to the backward flow implied by the local positive

slope in the equation of state. The spreading exponents vary in the beginning of the spreading process, but are only slightly affected in the later stages.

A more systematic study is be done by varying the slope in a piece-wise linear equation of state, $d\gamma/d\Gamma$ at $\Gamma = 0$, as shown in Fig. 2.12.

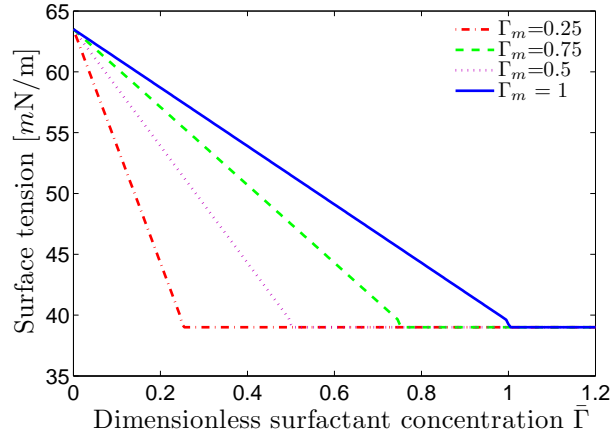


Figure 2.12: Different slope in the equation of state.

Figure 2.13 shows the corresponding rim positions from axisymmetric spreading simulations with finite surfactant supply. We conclude that for higher slopes, the rim position curve lies higher, but the effect on the spreading exponents is very small in the later stage.

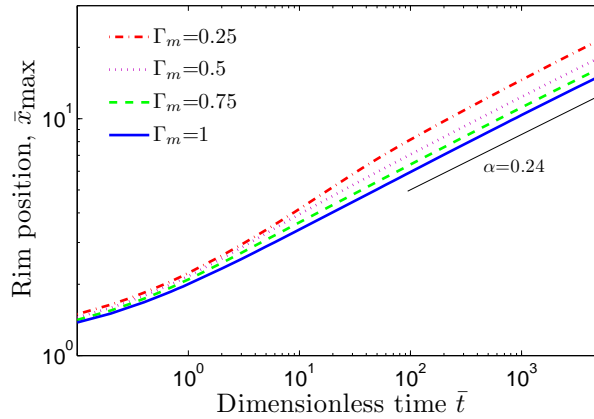


Figure 2.13: Effect of different initial slope in the equation of state on spreading exponents.

Thus, even extreme modifications of the equation of state for insoluble surfactant

do not drastically affect the time evolution of the rim position.

2.4 Conclusions

We have investigated the axisymmetric spreading dynamics of insoluble surfactants on thin liquid films. Numerical simulations of the far-field spreading dynamics compare very favorably with the experimental results reported in the literature. A non-linear equation of state, which provides an excellent fit for the experimental data of surface tension, is shown to influence spreading rates considerably compared with a linear equation of state.

A fingering instability is observed similar in appearance to the case of soluble surfactants, which is induced by the temporary entrapment of sub-phase liquid in the surfactant deposition area and its subsequent release. The expelled liquid enhances surfactant transport across the crater region, i. e. the expulsion has direct effect on the spreading rates. If the expulsion initiates at an earlier stage, the film thickness in the crater region has not thinned and its extension has not increased as much. Consequently, the crater region constitutes less of a flow obstacle for the expelled film. This has a noticeable influence on the spreading exponents that were determined as $\alpha = 0.32$ after, and $\alpha = 0.22$ before expulsion for $\epsilon = 0.012$. This range of values matches very well with the range of experimentally measured exponents between 0.23 and 0.34.

Since our model is based on the assumption of axisymmetry, the description of the expulsion process is also limited to axisymmetric case, unlike the fingering instabilities observed during the experiments. Owing to the uncertainties related with the experimental surfactant droplet deposition process, the relevant initial conditions may differ for the model and experiments. Furthermore, for a more faithful representation of the experiments the model should include the effects induced by the presence of the liquid-liquid interface between the droplet and the sub-phase film, or the deformation of the surfactant droplet in the vicinity of the three-phase contact line.

Chapter 3

Insoluble surfactant spreading at initially curved liquid-air interfaces

3.1 System description for spreading along rivulet interface

In the previous chapter we studied surfactant spreading on initially flat liquid-air interfaces. In technological applications, however, the interface often exhibits a non-zero curvature at the beginning of the spreading process. In the context of enhanced oil recovery (EOR), for instance, liquid phases are confined in pores of a very small scale, resulting in non-flat interfaces. This chapter is devoted to a study of an insoluble surfactant spreading on spatially confined thin liquid films and the effects these confinements have on transient rivulet morphology.

We consider the spreading of an insoluble surfactant on a thin curved liquid film of constant Newtonian viscosity μ . The liquid is confined to a stripe of width w and length L as shown in Fig. 3.1. This confinement can be achieved experimentally by chemical patterning: the substrate surface is hydrophilic within the stripe and hydrophobic outside it. The length L is large enough such that longitudinal edge effects can be neglected, thus, we assume that the rivulet height is initially uniform in x -direction.

An important characteristic of the system is that the liquid film is thin, thus the aspect ratio is very small: $\varepsilon \equiv h_0/(w/2) \ll 1$. We introduce a Cartesian coordinate system with the x -axis parallel to the rivulet and the z -axis normal to the (horizontal) substrate surface, i.e. opposite to the direction of gravity, see Fig. 3.1. The position $x = 0$ corresponds to the center of the surfactant deposition

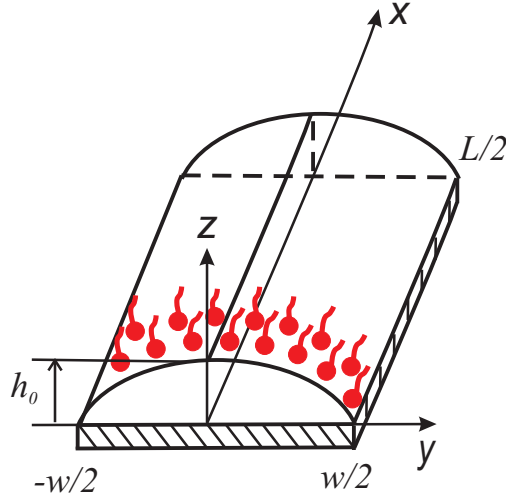


Figure 3.1: Sketch of the rivulet geometry with initial surfactant distribution.

area, and $y = 0$ corresponds to the centerline of the rivulet.

We choose the material system of oleic acid spreading on glycerol rivulets [67] for a comparison of numerical results with experimental data. During the experiments, liquid films of anhydrous glycerol with a center thickness of $h_0 = 1 - 10 \mu\text{m}$ were deposited on the hydrophilic regions of the substrates using spin-coating. The patterning procedure resulted in an advancing contact angle for glycerol between 70° and 90° on the hydrophobic areas, thus confining the liquid to the hydrophilic stripe during the experiments. After deposition of the sub-phase, typically 0.1 to $0.2 \mu\text{l}$ of the insoluble surfactant *cis*-9-octadecenoic acid were deposited in the center of the rivulets using a micro-syringe as a dip-pen. The time evolution of the film height was monitored using interference microscopy.

3.2 Mathematical model based on lubrication approximation

Based on the lateral aspect ratio $\varepsilon \equiv 2h_0/w \ll 1$, the small-slope approximation can be applied to derive an evolution equation for the sub-phase height profile [38] that accounts for the influence of Marangoni stresses, hydrostatic and capillary pressure gradients. An equation for surfactant surface transport including the effects of convection by the liquid surface motion as well as surface diffusion is derived in [70, 71, 72, 69]. Borgas & Grotberg [10] and Troian *et al.* [12] further simplified this equation for thin liquid films. A detailed derivation of these two equations can be found in Appendix A.

Using the scaled variables

$$\bar{x} = \frac{2x}{w}, \quad \bar{y} = \frac{2y}{w}, \quad \bar{h} = \frac{h}{h_0} \quad (3.1)$$

$$\bar{\Gamma} = \frac{\Gamma}{\Gamma_0}, \quad \bar{p} = \frac{pw^2}{4h_0\Pi_{\max}}, \quad \bar{t} = t \frac{4h_0\Pi_{\max}}{\mu w^2} \quad (3.2)$$

we arrive at the following non-dimensional system of equations

$$\frac{\partial \bar{h}}{\partial \bar{t}} + \bar{\nabla} \left[\frac{1}{2}(\bar{h}^2 \bar{\nabla} \bar{\gamma}) - \frac{\text{Bo}}{3} \bar{h}^3 \bar{\nabla} \bar{h} - \frac{\varepsilon^2}{3} \bar{h}^3 \bar{\nabla} \bar{p} \right] = 0 \quad (3.3)$$

$$\frac{\partial \bar{\Gamma}}{\partial \bar{t}} + \bar{\nabla} \left[\bar{h} \bar{\Gamma} \bar{\nabla} \bar{\gamma} - \frac{\text{Bo}}{2} \bar{h}^2 \bar{\Gamma} \bar{\nabla} \bar{h} - \frac{\varepsilon^2}{2} \bar{h}^2 \bar{\Gamma} \bar{\nabla} \bar{p} \right. \quad (3.4)$$

$$\left. - \frac{1}{\text{Pe}_s} \bar{\nabla} \bar{\Gamma} \right] = 0$$

$$\bar{p} = -\bar{\gamma} \bar{\nabla}^2 \bar{h} \quad (3.5)$$

$$\bar{\gamma} = \frac{\gamma_m}{\Pi_{\max}} + \exp(-\bar{A} \bar{\Gamma}^2) \quad (3.6)$$

where $\text{Bo} \equiv \rho g h_0^2 / \Pi_{\max}$ is the Bond number, $\text{Pe}_s \equiv h_0 \Pi_{\max} / (\mu D_s)$ is the surface Peclet number, μ and ρ are the fluid viscosity and density, respectively, and D_s represents the surface diffusion coefficient.

The second term in Eqs. (3.3,3.4) represents the influence of Marangoni stresses arising from gradients in surface tension $\bar{\gamma}$. The third term in both equations accounts for hydrostatic pressure gradients, and the fourth term reflects capillary pressure gradients. The last term in Eq. (3.4) describes surface diffusion along the liquid-air interface. Equation (3.5) corresponds to the Laplace-Young equation. Equation (3.6) is the non-dimensional version of the equation of state for oleic acid on glycerol (see Chapter 1, Section 1.2), which we used to fit the experimental data,

$$\gamma = \gamma_m + \Pi_{\max} \exp(-\bar{A} \Gamma^2 / \Gamma_0^2) \quad (3.7)$$

where $\Pi_{\max} = 24 \text{ mN/m}$ is the maximum spreading pressure, $\gamma_m = 39 \text{ mN/m}$ is the asymptotic value of the surface tension, $\Gamma_0 \equiv 3.5 \mu\text{l/m}^2$ and $\bar{A} = 6.125$ is a fit parameter. Thus, we consider a realistic, non-linear equation of state $\gamma(\Gamma)$ connecting surface tension and surface concentration for this material system.

The system of equations (3.3-3.6) is solved together with the following boundary

conditions (BCs)

$$\frac{\partial \bar{h}}{\partial \bar{x}}(0, \bar{y}, \bar{t}) = 0 = \frac{\partial \bar{h}}{\partial \bar{y}}(\bar{x}, 0, \bar{t}) \quad (3.8)$$

$$\frac{\partial \bar{\Gamma}}{\partial \bar{x}}(0, \bar{y}, \bar{t}) = 0 = \frac{\partial \bar{\Gamma}}{\partial \bar{y}}(\bar{x}, 0, \bar{t}) \quad (3.9)$$

$$\frac{\partial \bar{p}}{\partial \bar{x}}(0, \bar{y}, \bar{t}) = 0 = \frac{\partial \bar{p}}{\partial \bar{y}}(\bar{x}, 0, \bar{t}) \quad (3.10)$$

$$\bar{h}(\bar{x}, 1, \bar{t}) = 0 \quad (3.11)$$

$$\frac{\partial \bar{\Gamma}}{\partial \bar{y}}(\bar{x}, 1, \bar{t}) = 0 \quad (3.12)$$

$$\bar{h}(\infty, \bar{y}, \bar{t}) = \bar{f}(\bar{y}) \quad (3.13)$$

$$\bar{\Gamma}(\infty, \bar{y}, \bar{t}) = 0 \quad (3.14)$$

$$\frac{\partial \bar{p}}{\partial \bar{x}}(\infty, \bar{y}, \bar{t}) = 0 \quad (3.15)$$

where $\bar{f}(\bar{y})$ is the boundary height profile corresponding to the static equilibrium. If the influence of gravity is negligible, the static equilibrium profile is parabolic $\bar{f}(\bar{y}) = 1 - \bar{y}^2$.

Boundary conditions (3.11, 3.12) represent the edge of the hydrophilic stripe, corresponding to a rivulet height of zero and no surfactant flux at this boundary. Conditions (3.13-3.15) represent a clean, uncontaminated liquid surface at large distance from the surfactant deposition region, so that the rivulet height is undisturbed from the initial height profile and no surfactant is present at this boundary. Equations (3.8-3.10) reflect the mirror symmetry of the system with respect to the planes $\bar{x} = 0$ and $\bar{y} = 0$. Boundary conditions (3.11,3.12) represent the edge of the hydrophilic stripe, and (3.13-3.15) a clean, uncontaminated liquid surface at a large distance away from the surfactant deposition region.

The following initial conditions (ICs) are used for the height profile and pressure

$$\bar{h}(\bar{x}, \bar{y}, \bar{t} = 0) = \bar{f}(\bar{y}), \quad \bar{p}(\bar{x}, \bar{y}, \bar{t} = 0) = -\gamma \frac{\partial^2 \bar{f}}{\partial \bar{y}^2} \quad (3.16)$$

We consider two cases regarding the IC for the surfactant distribution:

1. In the case of *finite surfactant supply*, a limited initial quantity of surfactant is distributed in the region $[0 \leq \bar{x} \leq \bar{x}_0; 0 \leq \bar{y} \leq 1]$ according to

$$\bar{\Gamma}(\bar{x}, 0) = \frac{1}{2}(1 - \tanh[B(\bar{x} - \bar{x}_0)]) \quad (3.17)$$

which subsequently depletes during the spreading process. Here, $B \equiv 10$ defines the steepness of the initial concentration distribution. The parameter \bar{x}_0 quantifies the length of the area that is (initially) covered with surfactant.

2. In experiments, however, the deposited surfactant quantity is often large and does not deplete as fast as in the finite supply model. To mimic such a

continuous surfactant supply, we impose a constant surface concentration in the region of surfactant deposition, i.e., $\bar{\Gamma}(0 \leq \bar{x} \leq \bar{x}_0, \bar{y}, \bar{t}) = \text{const}$, and we maintain continuity of the state variables at $\bar{x} = \bar{x}_0$.

We solve the system of equations (3.3-3.6) numerically with the finite element software Comsol Multiphysics 3.5, using transient analysis for the general form PDE equation mode.

3.3 Results and discussion

3.3.1 Finite surfactant supply

Figure 3.2 shows typical snapshots of the surfactant spreading process represented by film thickness isolines for dimensionless times \bar{t} from 0 to 1000. We observe film thinning in the vicinity of the deposition region and development of a rim, which is advancing along the rivulet. Similarly to the case of axisymmetric spreading, the rim widens in time and propagates in the x -direction with the maximum located at the rivulet centerline $\bar{y} = 0$. A strong rim asymmetry can be observed: the height gradients are much steeper on the front side of the rim compared to the back side and the transverse height profile is not parabolic in back of the rim. This asymmetry, however, diminishes with the progression of time.

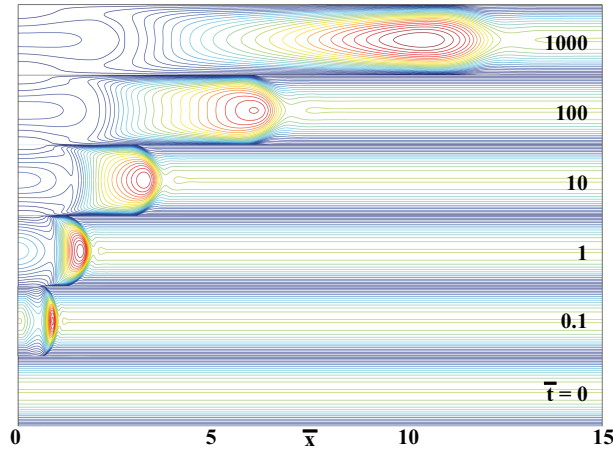


Figure 3.2: Contours of rivulet height for finite surfactant supply at $\bar{t} = 0, 0.1, 1, 10, 100, 1000$ with $\bar{x}_0 = 0.5$, $\text{Pe}_s = 50000$, $\varepsilon = 0.01$, and $\text{Bo} = 0$.

Figure 3.3 shows the time evolution of the height profile $\bar{h}(\bar{x}, \bar{y} = 0, \bar{t})$ and the surfactant concentration $\bar{\Gamma}(\bar{x}, \bar{y} = 0, \bar{t})$ at the rivulet center line, with parameters $\varepsilon = 10^{-2}$, $\text{Pe}_s = 10^3$, $\bar{x}_0 = 0.5$, and $\text{Bo} = 0$. The position where the maximum in the center-height is reached defines the rim position \bar{x}_{rim} . Comparing figures 3.3(a) and 3.3(b), we conclude that the surfactant front precedes the rim position. Since

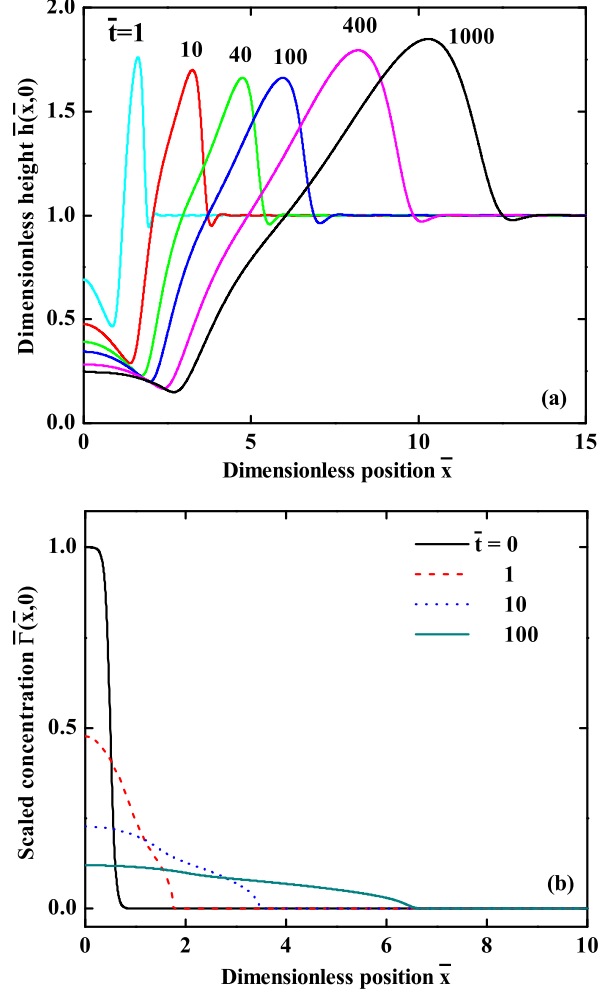


Figure 3.3: (a)-(b) Evolution of centerline height profile $\bar{h}(\bar{x}, \bar{y} = 0, \bar{t})$ and surfactant concentration $\bar{\Gamma}(\bar{x}, \bar{y} = 0, \bar{t})$ for finite surfactant supply and parameter values $\bar{x}_0 = 0.5$, $Pe_s = 1000$, $\varepsilon = 0.01$, and $Bo = 0$.

a finite amount of surfactant is modeled, it is depleted in time at the deposition region and redistributed along the rivulet surface.

The time evolution of the rim position \bar{x}_{rim} is presented in Fig. 3.4(a). To a good approximation, the rim position $\bar{x}_{\text{rim}}(t)$ follows a power law behavior $\bar{x}_{\text{rim}} \sim \bar{t}^\alpha$. The spreading exponents extracted from the data presented in Fig. 3.4(a) fall in the range 0.24 - 0.25, and are essentially independent of the aspect ratio ε .

The values of the spreading exponents α obtained from the corresponding ex-

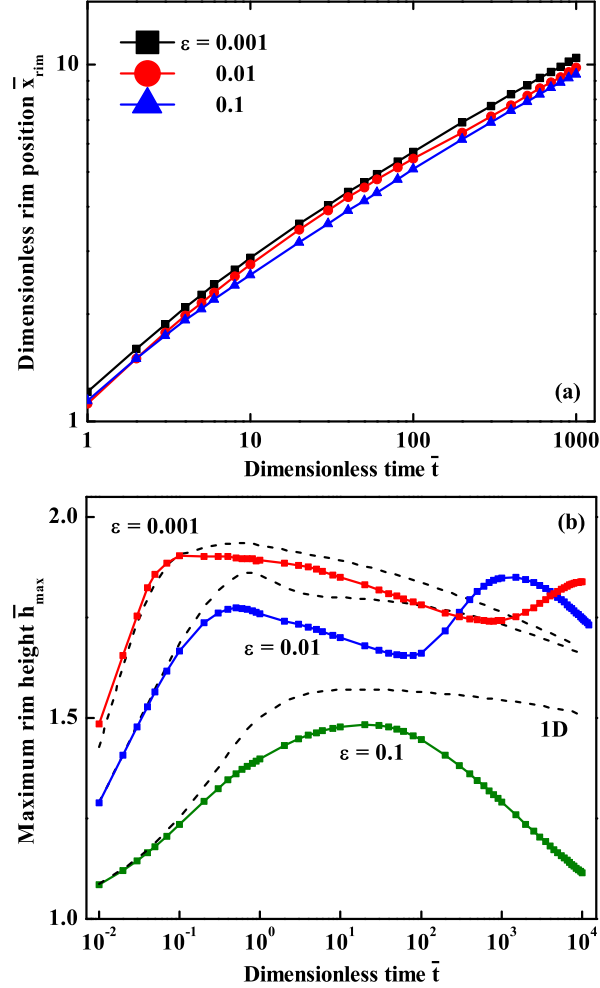


Figure 3.4: (a) Rim position $x_{\text{rim}}(\bar{t})$ for parameter values $\bar{x}_0 = 0.5$, $\text{Pe}_s = 1000$, and $\text{Bo} = 0$. (b) Maximum height vs dimensionless time for rivulets with finite surfactant supply (solid lines) compared to one-dimensional rectilinear spreading (dashed lines) for parameter values $\bar{x}_0 = 0.5$, $\text{Pe}_s = 1000$, and $\text{Bo} = 0$.

periments [67] are in the range between 0.32 and 0.34. The spreading exponents derived from the data in Fig. 3.4(a), are significantly smaller than the experimental results, for which the assumption of finite surfactant supply is not an accurate representation.

Figure 3.4(b) compares the time evolution of the rim height h_{max} for spreading along a rivulet (solid lines) with rectilinear, one-dimensional spreading along a thin liquid film of *uniform* thickness h_0 (dashed lines), i.e. in the limit of infinitely

wide rivulets, $w \rightarrow \infty$. The rapid increase of $\bar{h}_{\max}(\bar{t} \lesssim 0.2)$ represents the rim formation in the early stage of the spreading process. For lower aspect ratios two local maxima in $\bar{h}_{\max}(\bar{t})$ are observed, whereas for $\varepsilon = 0.1$ only a single peak is present. Except in the vicinity of the second maximum in $\bar{h}_{\max}(\bar{t})$, the rim height is larger for one-dimensional spreading due to the absence of transverse curvature. Smaller aspect ratios tend to give larger dimensionless rim heights, since smaller capillary pressure provides less of an opposing force to the height increase. Jensen [17] showed that for $\varepsilon \rightarrow 0$ and $\text{Pe}_s \rightarrow \infty$ the non-dimensional rim height equals 2 in the case of one-dimensional, rectilinear spreading.

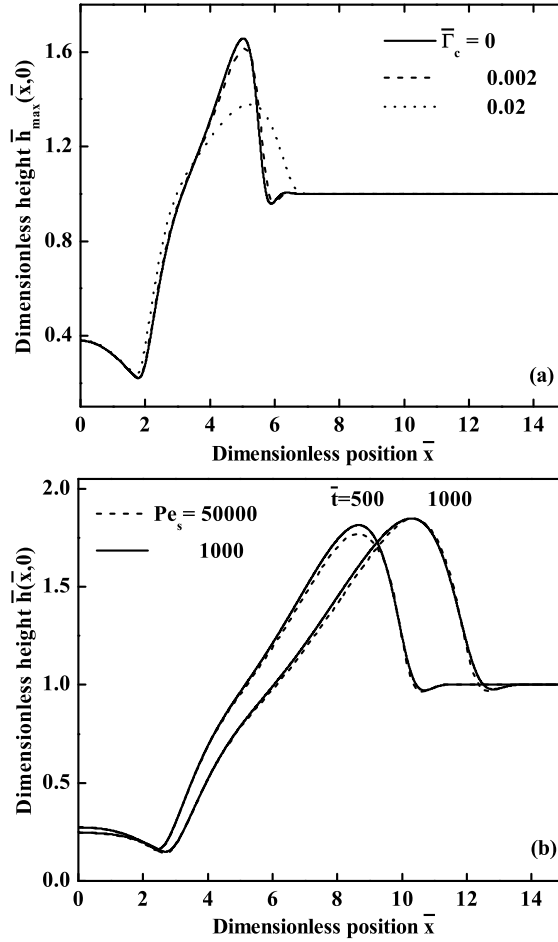


Figure 3.5: (a) Rivulet height profile for different pre-contamination levels for parameter values $\bar{x}_0 = 0.5$, $\text{Pe}_s = 1000$, $\varepsilon = 0.01$, and $\text{Bo} = 0$. (b) Effect of variations in Peclet number (50000 and 1000) on the rivulet center-height for $\bar{x}_0 = 0.5$, $\varepsilon = 0.01$, and $\text{Bo} = 0$.

During experiments surface-active contaminants, either airborne or from within the sub-phase liquid, can adsorb on the liquid-air interface. We account for such a contamination by adding a constant term $\bar{\Gamma}_c$ to the initial concentration distribution Eq. (3.17)

$$\bar{\Gamma}(\bar{x}, 0) = \bar{\Gamma}_c + 0.5(1 - \tanh[B(\bar{x} - \bar{x}_0)]) \quad (3.18)$$

The rim propagation dynamics along a pre-contaminated rivulet for a value of $\bar{\Gamma}_c = 0.02$ is essentially unaffected as compared to the case of $\bar{\Gamma}_c = 0$. However, already a contamination as small as 2% ($\bar{\Gamma}_c = 0.02$), which would be hard to detect experimentally, significantly reduces the rim height, as shown in Fig. 3.5(a), consistent with the findings of Dussaud *et al.* [28].

A variation of the Peclet number Pe_s from 1000 to 50000 has negligible effect on the rim position for $\bar{t} \leq 1000$ in Fig. 3.5(b). A Peclet number value of 1000 does not reduce the center-line height $\bar{h}_{\max}(\bar{t})$ compared to 50000, while a reduction was observed by Gaver & Grotberg [13] for one-dimensional surfactant spreading on thin liquid films of uniform thickness and Peclet numbers of 100 and 0.5.

3.3.2 Continuous surfactant supply

Figures 3.6(a,b) depict the time evolution of the surfactant concentration and the height profile in the case of continuous surfactant supply. The film thinning in the vicinity of the surfactant deposition area is significantly stronger than in the case of finite supply, because the constant surfactant concentration in the area $\bar{x} < \bar{x}_0$ sustains large surface tension gradients.

In Fig. 3.6(d) we present the rim position for different aspect ratios. The corresponding spreading exponents $\alpha = 0.40 \div 0.46$, fitted in the interval $10 < \bar{t} < 1000$, are higher compared to the case of finite surfactant supply, and an increased influence of the aspect ratio on the rim position \bar{x}_{rim} is apparent. The curves corresponding to aspect ratios $\varepsilon = 0.03$ and 0.01 exhibit an increase in the spreading exponent approximately at times $\bar{t} = 50$ and 200 , respectively. These transitions are preceded by a process of sub-phase expulsion [43], i.e. the ejection of liquid that was previously located in the area of surfactant deposition, as illustrated in Fig. 3.6(c) at $\bar{t} = 200$ for $\varepsilon = 0.03$. The dashed line in Fig. 3.6(d) corresponds to the rim position for an infinitely narrow surfactant deposition area, $\bar{x}_0 = 0$. No expulsion is observed in this case, which leads to significant reduction of $\bar{x}_{\text{rim}}(\bar{t})$.

While the fundamental setup of the numerical simulations and experiments are comparable, there are considerable uncertainties and differences connected to the surfactant deposition process. In the numerical simulations, surfactant is introduced as a dense monolayer on the surface of an initially *undisturbed* rivulet. Depending on the type of simulation, the amount of surfactant in the deposition area is then depleted or held constant during the course of the simulation. In experiments, due to the manual deposition technique, the deposited droplet is comparable in size to the rivulet width and initially squeezes part of the under-

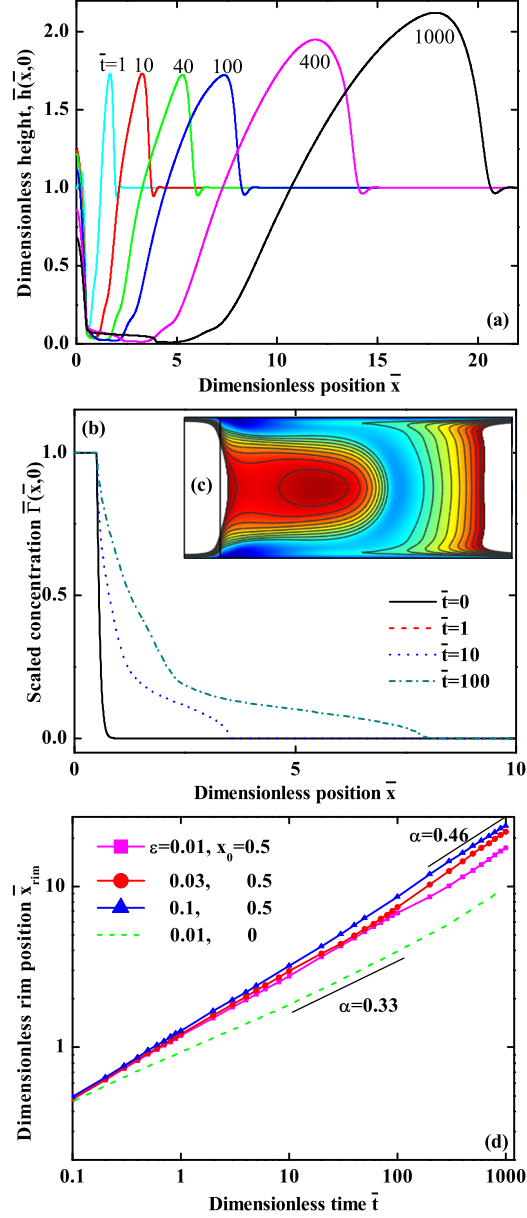


Figure 3.6: (a,b) Evolution of centerline height profile $\bar{h}(\bar{y} = 0)$ and surfactant concentration $\bar{\Gamma}(\bar{y} = 0)$ for continuous surfactant supply, $\varepsilon = 0.01$, $\text{Pe}_s = 1000$ and $\bar{x}_0 = 0.5$. (c) Sub-phase expulsion at $\bar{t} = 200$ for continuous surfactant supply and $\varepsilon = 0.03$. (d) Rim position $x_{\text{rim}}(\bar{t})$ for $\bar{x}_0 = 0.5$ and $\bar{x}_0 = 0$ and different values of the aspect ratio ε .

lying liquid. The relatively large amount of surfactant in the droplet ensures a continuous supply during the course of the experiment. Consequently, the numerical studies of surfactant spreading with a continuous supply can be expected to resemble the experimental data after short-time effects that are sensitive to the details of the deposition process have decayed.

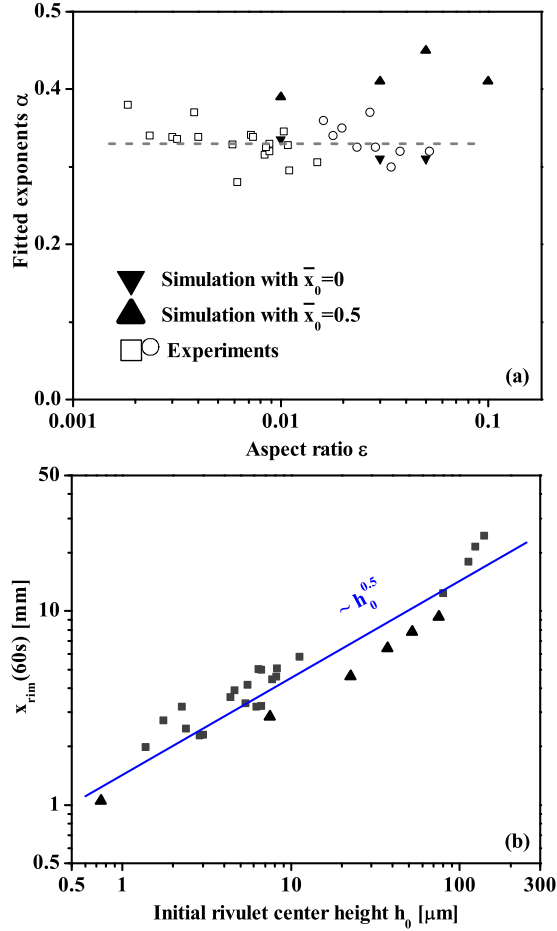


Figure 3.7: (a) Spreading exponent α as a function of the aspect ratio ϵ . Simulations with $\bar{x}_0 = 0.5$ (up-triangles) exhibited sub-phase expulsion while with $\bar{x}_0 = 0$ (down-triangles) did not. Open symbols indicate experiments with rivulet widths $w = 1.5$ mm (squares) and $w = 0.28$ mm (circles). (b) Numerical (triangles) and experimental (squares) rim position 60 s after surfactant deposition as a function of the initial height for $w = 1.5$ mm and $\bar{x}_0 = 0.5$. Solid line indicates scaling $x_{\text{rim}}(t = 60\text{ s}) \sim \sqrt{h_0}$.

Figure 3.7(a) shows the spreading exponents α as a function of the aspect ratio $\epsilon = 2h_0/w$. Experimental exponents (open symbols) were obtained for rivulet

widths of $w = 1.5$ mm and $w = 0.28$ mm. Exponents extracted from the numerical simulations for continuous supply and $\bar{x}_0 = 0.5$ are represented by up-triangles. Down-triangles designate numerical results for $\bar{x}_0 = 0$, with no sub-phase expulsion occurring. The latter resulted in slightly lower spreading exponents α that agree with the experimental data very well. The exponents corresponding to the blue down-triangles in Fig. 3.7(a) were fitted to the simulation results in the time interval $10 \leq \bar{t} \leq 100$, which is comparable to the experimental range.

At the edges of the surfactant source area, i.e. around $\bar{x} = \bar{x}_0$, the sub-phase film thickness rapidly decreases as depicted in Fig. 3.6(a). With the exception of the case $\bar{x}_0 = 0$, this implies that a volume of sub-phase liquid becomes temporarily immobilized in the surfactant-deposition region and is gradually discharged at a later time [Fig. 3.6(c)]. This delayed sub-phase release has a noticeable effect on the spreading exponent as shown in Fig. 3.7(a).

Figure 3.7(b) depicts the rim position 60 sec after deposition, $x_{\text{rim}}(60 \text{ s})$, as a function of the initial rivulet center height h_0 . Filled squares represent experimental data, while triangles indicate numerical simulations. The plotted simulation results were converted to dimensional values assuming the viscosity of pure glycerol at 25 °C. We assume that the rim propagation rate $\frac{dx_{\text{rim}}}{dt}$ scales with the Marangoni velocity $h_0\tau/\mu$. The stream-wise surface tension gradient $\tau = \partial\gamma/\partial x$ scales as $\tau \sim \Pi_{\text{max}}/x_{\text{rim}}$, thus, we expect a power law relation $x_{\text{rim}} \sim \sqrt{h_0}$, as derived in Chapter 2. The solid line in Fig. 3.7(b) corresponds to such a power law relation and is an excellent approximation to both experimental and numerical results. The numerically obtained peak positions in Fig. 3.7 systematically lie slightly below the experimental values. A probable explanation for this offset is water absorption into glycerol from the ambient atmosphere during the experiment, which reduces the viscosity of the sub-phase liquid.

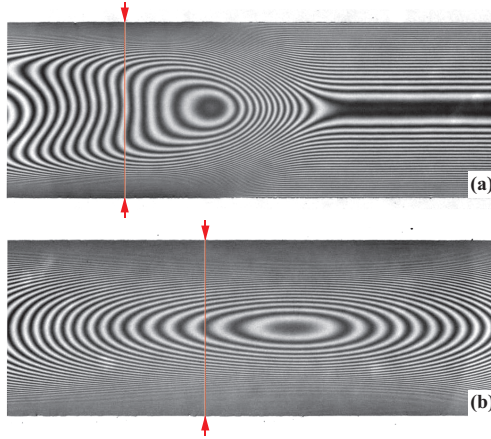


Figure 3.8: Interference microscopy images of the propagating rim at (a) an early stage ($t = 30$ s) and (b) a later stage ($t = 250$ s). The red lines are located at the distance of $w/2$ behind the rim. Images are taken from [67], courtesy of David Sinz.

The numerical results show a systematic change in the peak height and shape of the rim as it propagates along the rivulet, see Fig. 3.2. Initially the rim exhibits a considerable asymmetry in the stream-wise direction, which gradually disappears at later stages. The asymmetry at early stages, which is especially pronounced for low aspect ratio systems, was also observed during experiments [Fig. 3.8(a)], while at later stages it largely disappeared [Fig. 3.8(b)].

In Fig. 3.9 the non-dimensional rim height h_{\max}/h_0 is shown as a function of time for different values of the aspect ratio ε . At the initial stages of spreading process, a rapid increase of h_{\max} for times below $\bar{t} = 0.2$ is observed. For $\varepsilon = 0.01$ the rim height then effectively reaches a plateau value. At later times a pronounced increase of h_{\max} occurs for all studied aspect ratios. The gray dashed lines in Fig. 3.9 correspond to simulations with a width of the deposition region $\bar{x}_0 = 0.5$, which leads to a sub-phase expulsion process and thus to slightly higher values of the rim height h_{\max} . Numerical results for the case of $\bar{x}_0 = 0$ are represented by the solid line. The latter do not exhibit any sub-phase expulsion and are in perfect quantitative agreement with the experimental data in Fig. 3.9 (circles and squares) obtained for $\varepsilon \approx 0.01$. Both the onset time and amplitude of the peak height increase are in good agreement.

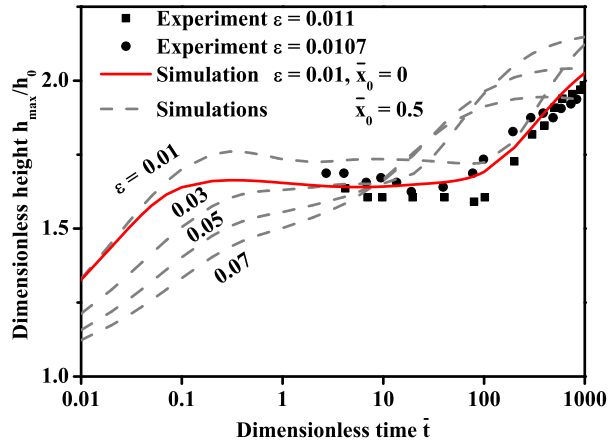


Figure 3.9: Dimensionless rim height $\bar{h}_{\max}(\bar{t})$ for different values of ε . The dashed lines correspond to numerical simulations for continuous supply of surfactant over a deposition region of length $\bar{x}_0 = 0.5$, while the solid line represents simulation with $\bar{x}_0 = 0$. Symbols represent experimental data obtained for $w = 1.5$ mm and aspect ratios of $\varepsilon = 0.011$ (squares) and $\varepsilon = 0.0107$ (circles), courtesy of David Sinz.

The increase in the rim height is the consequence of changes in the transverse rivulet height profile, which are caused by declining lateral surface tension gradients. The transverse height profile $\bar{h}(\bar{x}_{\text{rim}} - 1, \bar{y})$ at a distance of half of the rivulet width behind the rim position is shown in Fig. 3.10(a). A strong flattening in the middle of the rivulet is observed at $\bar{t} = 50$. At a later time $\bar{t} = 400$ this

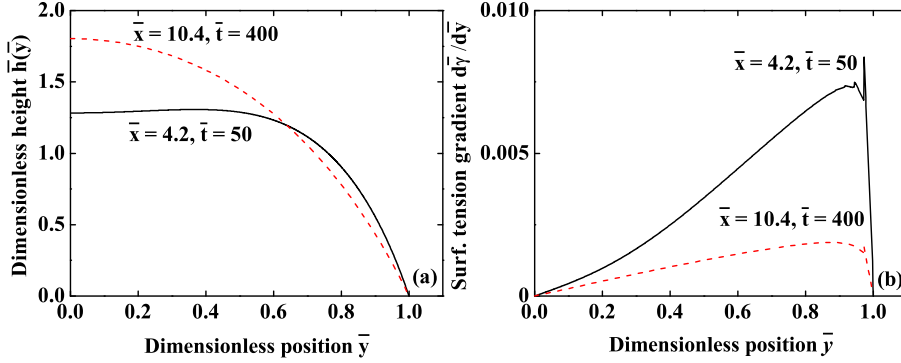


Figure 3.10: (a) Transverse height profile $\bar{h}(\bar{y}, \bar{t})$ for times $\bar{t} = 50$ and $\bar{t} = 400$ located at the distance $w/2$, behind the rim. (b) Surface tension gradient in y -direction $\partial\bar{\gamma}/\partial\bar{y}$ for $\bar{t} = 50$ and $\bar{t} = 400$ located at the distance of $w/2$, behind the rim. Input parameters are $\bar{x}_0 = 0.5$, $\text{Pe}_s = 1000$, $\varepsilon = 0.01$, and $\text{Bo} = 0$.

flattening has disappeared resulting in a parabolic transverse height profile. This qualitative difference in the height profiles is caused by lateral concentration gradients originating from the non-uniform surface velocity profile. Since the driving force of the spreading process is Marangoni stress, the flow velocity scales with the local film thickness. The stream-wise velocity is higher in the middle of the rivulet as compared to its edges, since the film thickness is 0 at the boundaries of the hydrophilic stripe. The lateral shear in the velocity distribution initially leads to a non-uniform surfactant distribution $\Gamma(y)$ at the surface.

Darhuber *et al.* [68] studied rivulet shape distortions as a consequence of transverse temperature gradients. The relevant non-dimensional number was identified to be $\tau/(\varepsilon p_{cap})$, where p_{cap} is the capillary pressure. When the value of $\tau = \nabla_{||}\gamma$ falls below a certain threshold, the shape distortion disappears and the parabolic cross-section is restored. We speculate that the same mechanism is the origin of the shape changes in Figs. 3.10, which is supported by the data presented in Fig. 3.10(b). A strong decay of the lateral surface tension gradient at positions and times corresponding to the curves in Fig. 3.10(a) is observed. The relaxation of the transverse height profile towards a parabolic shape leads to an increase in the center height, which explains the increase in rim height h_{max} observed in Fig. 3.9. Larger values of the aspect ratio ε are associated with higher lateral curvature and hence an increased capillary pressure, which acts as the restoring force for the transition in the height profile. Consequently, the transition occurs earlier for larger aspect ratios. We note that an increase in the peak height observed for one-dimensional spreading can only occur due to sub-phase expulsion [43]. The second increase in \bar{h}_{max} observed in Fig. 3.9 is a consequence of lateral confinement, since it is also present for the case of $\bar{x}_0 = 0$.

3.4 Summary and conclusions

We conducted a numerical study of surfactant spreading on non-flat liquid-air interfaces, in particular narrow rivulets. Using a numerical model based on the lubrication approximation, we monitored the evolution of the liquid height profile after deposition of an insoluble surfactant monolayer at the rivulet-air interface. The results were compared to experimental findings for oleic acid spreading along glycerol rivulets, defined by chemical surface patterning, and excellent agreement was achieved.

The spreading dynamics locally is well approximated by power-law $x \sim t^\alpha$. We conclude that for laterally uniform initial rivulet height profiles, the initial film thickness has little effect on the spreading exponents. Continuous, i.e. unlimited surfactant supply leads to higher exponents and increases the influence of the rivulet aspect ratio as compared to the case of limited supply. The spreading exponents determined from continuous-supply model and line source compare favorably with the experimental data. The lateral confinement induces non-uniform height- and surface velocity profiles, which manifest themselves in a pronounced transition of the evolving rivulet morphology.

Chapter 4

Soluble surfactant spreading at initially curved liquid-air interfaces

4.1 Introduction and system description for spreading along rivulet interface

Chapters 2 and 3 were devoted to the study of insoluble surfactant spreading. In technological applications, however, surfactants are often soluble in at least one liquid phase. Several experimental and numerical studies deal with soluble surfactant spreading [11, 73, 16, 74, 75, 34, 35, 76, 77, 78, 55, 79, 54, 27, 80]. Jensen and Grotberg, for instance, presented a one-dimensional model for the spreading of soluble surfactants [16] considering linearized Langmuir sorption kinetics and fast vertical diffusion across the film thickness. In this chapter we present a model for soluble surfactants spreading at curved liquid-air interfaces. The goal is to quantitatively compare numerical solutions with experimental results.

We consider the spreading of a soluble surfactant on a thin liquid film that is chemically confined to a hydrophilic stripe of width w and length L . The model geometry illustrated in Fig. 4.1 is fundamentally the same as that studied in Chapter 3, except that a soluble surfactant leads to a non-zero bulk concentration.

4.1.1 Equation of state

In order to quantify the spreading pressure due to surfactant concentration gradients, experimental data is required to determine the relation between surface tension γ and surfactant concentration Γ . The dependence of surface tension γ

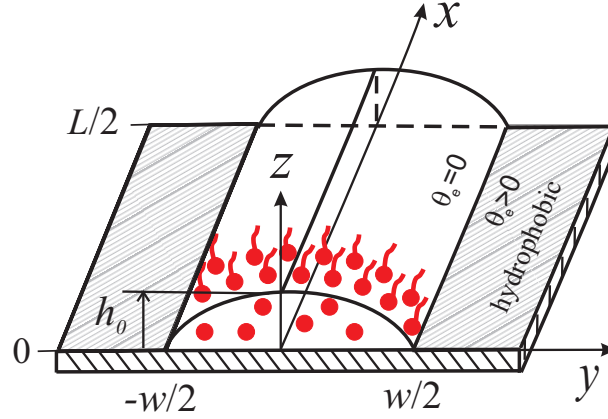


Figure 4.1: Sketch of the rivulet geometry illustrating the initial distribution of a soluble surfactant.

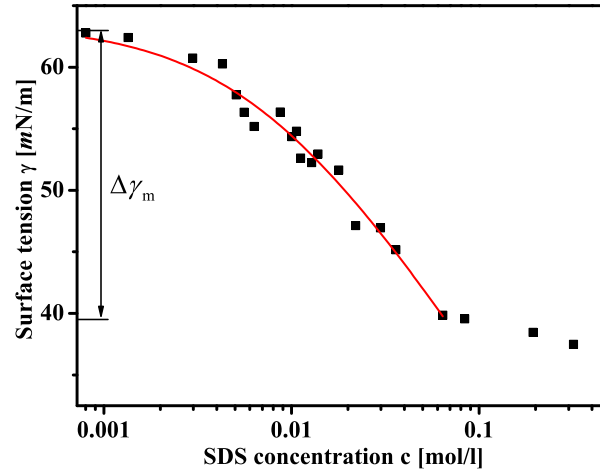


Figure 4.2: Surface tension of glycerol as a function of the SDS bulk concentration. The solid line represents a non-linear equation of state (4.1).

on bulk concentration c is measured experimentally. Equilibrium equation is then used to relate Γ and c . Our surfactant of choice is sodium dodecyl sulfate that is soluble in glycerol. The dependence of the glycerol surface tension γ on c was measured using a Wilhelmy plate technique [86], with the resulting data shown in Fig. 4.2. For concentrations c above 0.065 mol/l, a pronounced kink is visible in surface tension, which we ascribe to the formation of micelles. In this range, gelation of the liquid associated with a strong change in the rheology was observed, which made surface tension determination in this concentration region somewhat unreliable.

The non-linear equation of state derived from the Langmuir and Gibbs adsorp-

tion isotherm follows as

$$\gamma = \gamma_0 + RT\Gamma_\infty \ln \left(1 - \frac{c}{k_2\Gamma_\infty/k_1 + c} \right) \quad (4.1)$$

where γ_0 is the surface tension of pure glycerol, R is the universal gas constant and T the absolute temperature, k_1 and k_2 are the adsorption- and desorption rate constants, respectively, and Γ_∞ is the maximum surface concentration at complete coverage of the surface. We use Eqs. (4.1) to fit the experimental data in Fig. 4.2 for the dependance of surface tension on bulk concentration, $\gamma(C)$, which yielded the parameter values $\Gamma_\infty = 4.2 \cdot 10^{-6}$ mol/m² and $k_2/k_1 = 1.7 \cdot 10^6$ m⁻¹. The maximum spreading pressure $\Delta\gamma_m$ is also indicated in Fig. 4.2. Since we do not take into account the presence of surfactant micelles, the validity of this model is restricted to concentrations below the so-called critical micelle concentration.

For the comparison of the numerical results with the experimental data, we will use results of SDS spreading on glycerol confined to narrow rivulets by chemical patterning [86]. Liquid films of anhydrous glycerol with a center thickness of $h_0 = 2.5 - 10$ μm were deposited on the hydrophilic regions of the substrates using spin-coating. Two types of experiments were conducted. In the first type, termed *solution deposition*, a $0.1 - 0.2$ μl droplet of an SDS-glycerol solution was deposited onto the sub-phase film. In the second type termed *solid deposition*, a small pellet of compressed SDS powder was deposited. The dynamics following surfactant deposition were monitored by means of interference microscopy.

4.2 Mathematical model based on lubrication approximation and assumption of fast vertical diffusion

Based on the lateral aspect ratio $\varepsilon \equiv 2h_0/w \ll 1$, the small-slope approximation can be applied to derive evolution equation for the sub-phase height profile [38] that accounts for the influence of Marangoni stresses, hydrostatic and capillary pressure gradients. An equation for surfactant surface transport including the effects of convection by the liquid surface motion as well as surface diffusion is derived in [70, 71, 72, 69]. This equation is further transformed for thin liquid film systems [10, 12]. In the case of soluble surfactants an additional term J appears in this equation that accounts for bulk-surface exchange due to adsorption/desorption processes. Jensen and Grotberg developed a theoretical model for the dynamics of thin liquid films in the presence of non-uniform distributions of a soluble surfactant [16]. A very important assumption of the model is the so-called fast vertical diffusion

$$\frac{t_d}{t_M} \equiv \frac{h_0^2}{D_b} \frac{4h_0\Delta\gamma_m}{\mu w^2} \equiv \varepsilon^2 \cdot \text{Pe}_b \ll 1, \quad (4.2)$$

where t_d/t_M is the ratio of diffusion and Marangoni time scales, D_b is the bulk diffusion coefficient and Pe_b is the bulk Peclet number. The authors also assume a linear equation of state $\gamma = \gamma_0 - A\Gamma$ as well as a linear relation between the surfactant bulk concentration in the liquid film $c(x, y, z, t)$ and the equilibrium surface concentration Γ_{eq} . We generalize this model as to include the full non-linear Langmuir equation for bulk-surface exchange J as well as the corresponding equilibrium isotherm

$$J = k_1 c_s \left(1 - \frac{\Gamma}{\Gamma_\infty} \right) - k_2 \Gamma \quad (4.3)$$

$$\frac{\Gamma_{eq}}{\Gamma_\infty} = \frac{k_1 c_s}{k_2 \Gamma_\infty + k_1 c_s} \quad (4.4)$$

where J is the surfactant flux with units of mol/(m²s), $k_{1,2}$ are the adsorption- and desorption rate constants, and $c_s(x, y, t) = c(x, y, z = h, t)$ is the bulk concentration at the surface.

The bulk transport of surfactant is governed by the convection and diffusion equation

$$\frac{\partial c}{\partial t} + \mathbf{u} \cdot \nabla c = D_b \nabla^2 c \quad (4.5)$$

For thin films and fast vertical diffusion the concentration $c(x, y, z, t)$ can be decomposed into a component independent of z and a small fluctuation [16]

$$c = C(x, y, t) + \varepsilon^2 \text{Pe}_b C_1(x, y, z, t) \quad (4.6)$$

with

$$\frac{1}{h} \int_0^h C_1(x, y, z, t) dz = 0 \quad (4.7)$$

Averaging Eq. (4.5) with respect to z , one arrives at the convection-diffusion equation for the height-averaged bulk concentration $C(x, y, t)$, which is discussed below.

We introduce the dimensionless variables

$$\bar{x} \equiv \frac{2x}{w}, \quad \bar{y} \equiv \frac{2y}{w}, \quad \bar{h} \equiv \frac{h}{h_0}, \quad \bar{t} \equiv \frac{t}{t_M} \equiv t \frac{4h_0 \Delta \gamma_m}{\mu w^2} \quad (4.8)$$

$$\bar{p} \equiv \frac{p w^2}{4h_0 \Delta \gamma_m}, \quad \bar{\Gamma} \equiv \frac{\Gamma}{\Gamma_\infty}, \quad \bar{C} \equiv \frac{k_1 C}{k_2 \Gamma_\infty} \quad (4.9)$$

and arrive at the dimensionless system of equations

$$\frac{\partial \bar{h}}{\partial \bar{t}} + \bar{\nabla} \left[\frac{1}{2} (\bar{h}^2 \bar{\nabla} \bar{\gamma}) - \frac{\varepsilon^2}{3} \bar{h}^3 \bar{\nabla} \bar{p} \right] = 0 \quad (4.10)$$

$$\frac{\partial \bar{\Gamma}}{\partial \bar{t}} + \bar{\nabla} \left[\bar{h} \bar{\Gamma} \bar{\nabla} \bar{\gamma} - \frac{\varepsilon^2}{2} \bar{h}^2 \bar{\Gamma} \bar{\nabla} \bar{p} - \frac{1}{\text{Pe}_s} \bar{\nabla} \bar{\Gamma} \right] = K (\bar{C} (1 - \bar{\Gamma}) - \bar{\Gamma}) \quad (4.11)$$

$$\frac{\partial \bar{C}}{\partial \bar{t}} + \left[\frac{\bar{h}}{2} \bar{\nabla} \bar{\gamma} - \frac{\varepsilon^2}{3} \bar{h}^2 \bar{\nabla} \bar{p} \right] \bar{\nabla} \bar{C} - \frac{1}{\text{Pe}_b \bar{h}} \bar{\nabla} [\bar{h} \bar{\nabla} \bar{C}] = \frac{\beta K}{\bar{h}} (\bar{\Gamma} - \bar{C} (1 - \bar{\Gamma})) \quad (4.12)$$

$$\bar{p} = -\bar{\gamma} \bar{\nabla}^2 \bar{h} + \text{Bo} \bar{h} + \bar{\Pi} \quad (4.13)$$

$$\bar{\gamma} = \frac{1}{\Delta \gamma_m} (\gamma_0 + RT \Gamma_\infty \ln (1 - \bar{\Gamma})) \quad (4.14)$$

In the system of equations (4.10-4.14) the following dimensionless parameters are introduced

$$\varepsilon \equiv \frac{2h_0}{w}, \quad \text{Bo} \equiv \frac{\rho g w^2}{4 \Delta \gamma_m}, \quad \text{Pe}_s \equiv \frac{h_0 \Delta \gamma_m}{\mu D_s} \quad (4.15)$$

$$\text{Pe}_b \equiv \frac{h_0 \Delta \gamma_m}{\mu D_b}, \quad \beta \equiv \frac{k_1}{k_2 h_0}, \quad K \equiv k_2 t_M \quad (4.16)$$

Here, p is the augmented pressure [38], Π is the so-called disjoining pressure contribution that is relevant for ultrathin films [84], Bo is the Bond number, Pe_s and Pe_b are the Peclet numbers for surfactant surface and bulk transport, respectively, D_s the surface diffusion coefficient, $\Delta \gamma_m$ is the maximum spreading pressure as indicated in Fig. 4.2, K the ratio of the time scale of the flow and the time scale of desorption, and β is the surface-bulk partitioning parameter proportional to the ratio of adsorption/desorption rate constants.

The total amount of surfactant in a column of liquid with infinitesimal base area $dA = dx dy$ is $(Ch + \Gamma)dA$, where the first and second terms correspond to the surfactant amounts in the bulk and at the interface, respectively. If \bar{C} is small, Eq. (4.4) reduces to the linearized Langmuir isotherm $\Gamma \approx k_1 C / k_2$. Thus, $\beta \equiv k_1 / (k_2 h_0)$ quantifies the partitioning ratio of the surfactant amount adsorbed at the surface and dissolved in the bulk liquid. When $\beta \ll 1$ almost all the surfactant is dissolved in the bulk, whereas for $\beta \gg 1$ almost all of it resides at the interface.

In the following subsections, we present two separate sets of initial and boundary conditions (BCs), termed finite and continuous surfactant supply, that represent solution- and solid deposition, respectively, as used in the experiments.

4.2.1 Initial and boundary conditions for continuous surfactant supply

The deposition of solid SDS is represented in our model by a continuous supply of surfactant. A certain initial quantity of surfactant is distributed uniformly in

the region $0 \leq x \leq \bar{x}_0$. We consider two cases with respect to the length of the surfactant deposition region x_0 : a so-called area source with $\bar{x}_0 = 1$ and a so-called line source with $\bar{x}_0 = 0$. We define the initial surface and bulk concentrations

$$\bar{\Gamma}(\bar{x} > \bar{x}_0, 0) = b\bar{\Gamma}_0(1 - \tanh[B(\bar{x} - \bar{x}_0)]) \quad (4.17)$$

$$\bar{C}(\bar{x} > \bar{x}_0, 0) = b\bar{C}_0(1 - \tanh[B(\bar{x} - \bar{x}_0)]) \quad (4.18)$$

The parameter $B \equiv 20$ defines the steepness of the initial concentration curve. The initial concentrations $\bar{\Gamma}_0$ and \bar{C}_0 are assumed to be in equilibrium and, thus, are related through Eq. (4.4) as

$$\bar{C}_0(\bar{x}, \bar{t} = 0) = \bar{\Gamma}(\bar{x}, \bar{t} = 0)/(1 - \bar{\Gamma}(\bar{x}, \bar{t} = 0)) \quad (4.19)$$

For the case of $\bar{x}_0 = 1$ (area source), we impose constant surface and bulk concentrations in the region $0 \leq \bar{x} \leq \bar{x}_0$

$$\bar{\Gamma}(\bar{x} \leq \bar{x}_0, \bar{y}, \bar{t}) = \bar{\Gamma}_0, \quad \bar{C}(\bar{x} \leq \bar{x}_0, \bar{y}, \bar{t}) = \bar{C}_0 \quad (4.20)$$

and choose $b = 1/2$ in Eqs. (4.17,4.18).

For the case of $\bar{x}_0 = 0$ (line source), we impose constant surface and bulk concentrations at the boundary $\bar{x} = 0$,

$$\bar{\Gamma}(\bar{x} = 0, \bar{y}, \bar{t}) = \bar{\Gamma}_0, \quad \bar{C}(\bar{x} = 0, \bar{y}, \bar{t}) = \bar{C}_0 \quad (4.21)$$

and set $b = 1$ in Eqs. (4.17,4.18), which corresponds to a smooth transition from finite to vanishing concentration values.

The system of equations (4.10-4.14) is solved together with the following boundary conditions (BCs)

$$\frac{\partial \bar{h}}{\partial \bar{x}}(0, \bar{y}) = \frac{\partial \bar{p}}{\partial \bar{x}}(0, \bar{y}) = 0 \quad (4.22)$$

$$\frac{\partial \bar{h}}{\partial \bar{y}}(\bar{x}, 0) = \frac{\partial \bar{\Gamma}}{\partial \bar{y}}(\bar{x}, 0) = \frac{\partial \bar{C}}{\partial \bar{y}}(\bar{x}, 0) = \frac{\partial \bar{p}}{\partial \bar{y}}(\bar{x}, 0) = 0 \quad (4.23)$$

$$\bar{\Gamma}(\frac{L}{2}, \bar{y}) = \bar{C}(\frac{L}{2}, \bar{y}) = \frac{\partial \bar{p}}{\partial \bar{x}}(\frac{L}{2}, \bar{y}) = 0 \quad (4.24)$$

$$\bar{h}(\frac{L}{2}, \bar{y}) = \bar{f}(\bar{y}) \quad (4.25)$$

where $\bar{f}(\bar{y})$ is the boundary height profile corresponding to a rivulet in static equilibrium without surfactants adsorbed. If the influence of gravity is negligible, this profile is parabolic $\bar{f}(\bar{y}) = 1 - \bar{y}^2$. Equations (4.22-4.23) reflect the mirror symmetry of the system with respect to the planes $\bar{x} = 0$ and $\bar{y} = 0$. Boundary conditions (4.24,4.25) represent a clean, uncontaminated liquid surface at a large distance from the surfactant deposition region.

The chemical patterning is implemented by means of a discontinuous disjoining pressure, which is represented by the term $\bar{\Pi}$ in Eq. (4.13). On the hydrophilic

strip $0 < \bar{y} < 1$, where glycerol is deposited, we introduce a repulsive disjoining pressure

$$\Pi_i = A/h^3 \quad (4.26)$$

where $A > 0$ is a constant.

Since in our experiments the rivulet volume was sufficiently low such that the liquid remained confined to the hydrophilic region, we only include a narrow hydrophobic strip $1 < \bar{y} < 1.05$ adjacent to the hydrophilic strip in our model. In this region, we use the two-term disjoining pressure model introduced in [85]

$$\Pi_o = E \left[\left(\frac{h_*}{h} \right)^n - \left(\frac{h_*}{h} \right)^m \right] \quad (4.27)$$

where h_* is the constant thickness of an ultrathin precursor layer, $n > m > 1$ are integers,

$$E \equiv \frac{(n-1)(m-1)}{h_*(n-m)} \gamma (1 - \cos \theta_e) \quad (4.28)$$

and θ_e is the equilibrium contact angle. After non-dimensionalization, we obtain the expressions

$$\bar{\Pi}_i = -\bar{A}/\bar{h}^3 \quad \text{for } 0 < \bar{y} < 1 \quad (4.29)$$

$$\bar{\Pi}_o = \bar{E} \left[\left(\frac{\bar{h}_*}{\bar{h}} \right)^n - \left(\frac{\bar{h}_*}{\bar{h}} \right)^m \right] \quad \text{for } 1 < \bar{y} < 1.05 \quad (4.30)$$

where

$$\bar{A} \equiv \frac{A}{\Delta \gamma_m \varepsilon^2 h_0^2} \quad (4.31)$$

$$\bar{E} \equiv \bar{\gamma} \frac{w^2(n-1)(m-1)}{h_0^2 \bar{h}_*(n-m)} (1 - \cos \theta_e) \quad (4.32)$$

In our simulations we use the following values: $\bar{h}_* \equiv h_*/h_0 = 0.005$, $\theta_e = 10^\circ$, $n = 3$, $m = 2$ and $A = 7 \cdot 10^{-20}$ Nm.

The BCs at the outer boundary of the hydrophobic strip are represented by the no-flux conditions

$$\frac{\partial \bar{h}}{\partial \bar{y}}(\bar{x}, 1.05, \bar{t}) = 0 = \frac{\partial \bar{p}}{\partial \bar{y}}(\bar{x}, 1.05, \bar{t}) \quad (4.33)$$

$$\frac{\partial \bar{\Gamma}}{\partial \bar{y}}(\bar{x}, 1.05, \bar{t}) = 0 = \frac{\partial \bar{C}}{\partial \bar{y}}(\bar{x}, 1.05, \bar{t}) \quad (4.34)$$

The initial conditions for the film thickness in the hydrophobic and hydrophilic regions are prescribed as $\bar{h} = \bar{h}_*$ and $\bar{h}(\bar{x}, \bar{y}, 0) = \bar{h}_* + \bar{f}(\bar{y})$, respectively.

4.2.2 Initial and boundary conditions for finite surfactant supply

A model with finite surfactant supply can represent the deposition of a surfactant droplet onto a liquid rivulet. A limited initial quantity of surfactant is distributed uniformly in the region $0 \leq x \leq \bar{x}_0$, reflected by the initial conditions for surface concentration

$$\bar{\Gamma}(\bar{x}, 0) = \frac{\bar{\Gamma}_0}{2}(1 - \tanh [B(\bar{x} - \bar{x}_0)]) \quad (4.35)$$

and bulk concentration

$$\bar{C}(\bar{x}, 0) = \frac{\bar{C}_0}{2}(1 - \tanh [B(\bar{x} - \bar{x}_0)]) \quad (4.36)$$

which subsequently depletes during the spreading process.

In the experiments, the height of the deposited surfactant drop can be up to 10 times the center height of the rivulet. Consequently, we account for the presence of the droplet in the initial height profile, as sketched in Fig. 4.4(b),

$$\bar{h}(\bar{x} \leq \bar{x}_0, \bar{y}, 0) = \bar{f}(\bar{y}) + \bar{h}_{\text{drop}}\bar{f}(\bar{y})(\bar{x}_0^2 - \bar{x}^2) \quad (4.37)$$

$$\bar{h}(\bar{x} > \bar{x}_0, \bar{y}, 0) = \bar{f}(\bar{y}) \quad (4.38)$$

where the parameter \bar{h}_{drop} was varied between 0 and 10. Because of the spreading of the droplet, extreme film thinning - as observed for solid deposition - does not occur and disjoining pressure effects need not to be considered. Consequently, Eqs. (4.33,4.34) are replaced with

$$\bar{h}(\bar{x}, 1, \bar{t}) = 0 \quad (4.39)$$

$$\frac{\partial \bar{\Gamma}}{\partial \bar{y}}(\bar{x}, 1, \bar{t}) = 0 = \frac{\partial \bar{C}}{\partial \bar{y}}(\bar{x}, 1, \bar{t}) \quad (4.40)$$

The applicable BCs at $\bar{x} = 0$ are

$$\frac{\partial \bar{\Gamma}}{\partial \bar{x}}(0, \bar{y}) = \frac{\partial \bar{C}}{\partial \bar{x}}(0, \bar{y}) = 0 \quad (4.41)$$

The remaining BCs given in Eqs. (4.22-4.25) remain valid.

The system of equations (4.10-4.14) is solved, together with boundary and initial conditions, numerically with the finite element software Comsol Multiphysics 3.5, using transient analysis for the general form PDE equation mode.

4.3 Numerical results and discussion

4.3.1 Finite surfactant supply

In the case of finite surfactant supply, the surfactant depletes at the deposition region as time progresses and redistributes along the rivulet surface and into the

sub-phase, whereby the total surfactant amount

$$\int_0^{\frac{L}{2}} \int_{-\frac{w}{2}}^{\frac{w}{2}} \left(\Gamma + \int_0^h cz dz \right) dx dy = \int_0^{\frac{L}{2}} \int_{-\frac{w}{2}}^{\frac{w}{2}} (\Gamma + hC) dx dy \quad (4.42)$$

is conserved.

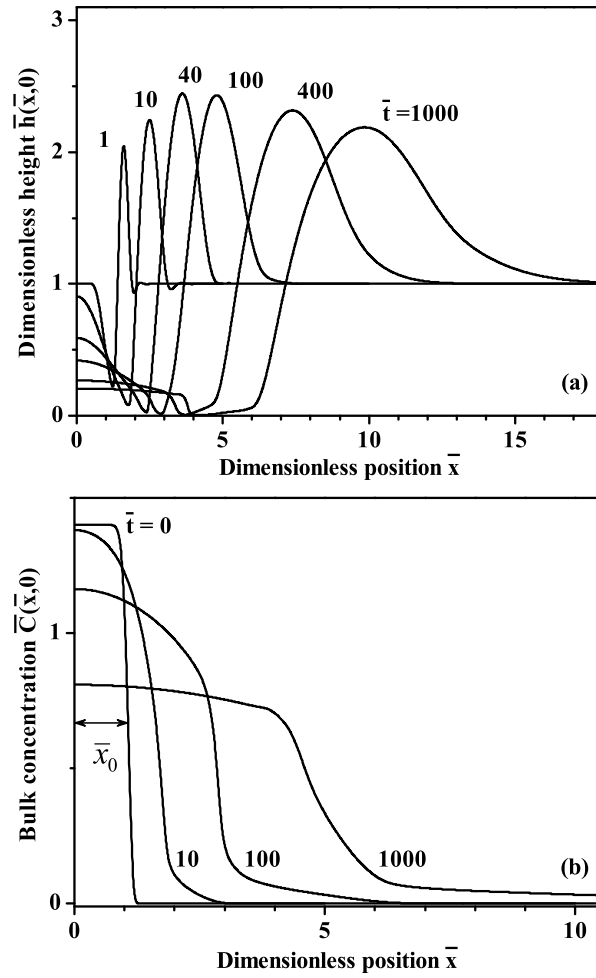


Figure 4.3: Time evolution of (a) the centerline height profile $\bar{h}(\bar{x}, \bar{y} = 0, \bar{t})$ and (b) the dimensionless surfactant bulk concentration $\bar{C}(\bar{x}, \bar{y} = 0, \bar{t})$ for the parameters settings $\bar{x}_0 = 1$, $\varepsilon = 0.01$, $h_0 = 10 \mu\text{m}$, $\bar{h}_{\text{drop}} = 0$, $\bar{C}_0 = 1.4$, $K = 1000$, $\beta = 0.06$, $\text{Pe}_s = 1000$, $\text{Pe}_b = 100$, and $\text{Bo} = 0$.

In Fig. 4.3(a,b) we present typical examples for the time evolution of the height profile $\bar{h}(\bar{x}, \bar{y} = 0, \bar{t})$ and surfactant bulk concentration $\bar{C}(\bar{x}, \bar{y} = 0, \bar{t})$ at the rivulet center line for $\bar{x}_0 = 1$, $\bar{C}_0 = 1.4$ and $\bar{h}_{\text{drop}} = 0$. The formation of a crater and a propagating rim is qualitatively similar to insoluble surfactant case.

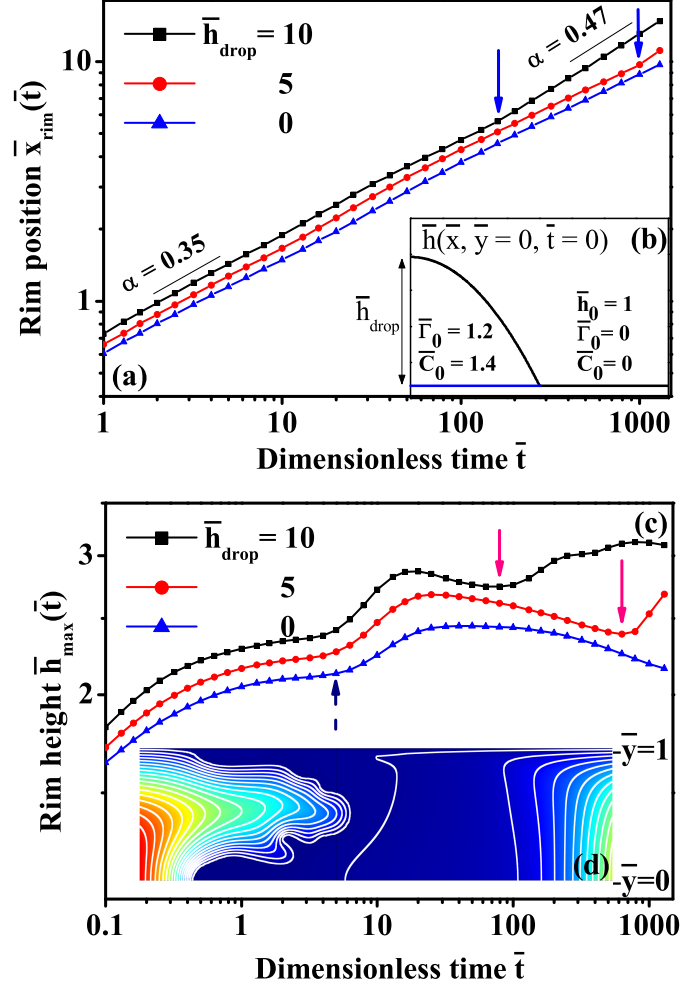


Figure 4.4: (a) Rim position $\bar{x}_{\text{rim}}(\bar{t})$ for different drop heights with parameter values $\bar{x}_0 = 1$, $\text{Pe}_s = 1000$, $\varepsilon = 0.01$, $\text{Bo} = 0$. (b) Initial conditions of the centerline height profile $\bar{h}(\bar{x}, \bar{t} = 0)$ and the surface- and bulk concentrations for different values of \bar{h}_{drop} . (c) Maximum height vs dimensionless time for rivulets with finite surfactant supply for different values of surfactant drop height with $\bar{x}_0 = 1$, $\varepsilon = 0.01$, $h_0 = 10 \mu\text{m}$, $\bar{C}_0 = 1.4$, $K = 1000$, $\beta = 0.06$, $\text{Pe}_s = 1000$, $\text{Pe}_b = 100$, $\text{Bo} = 0$. (d) Fingering instability observed for $\bar{h}_{\text{drop}} = 5$ at $\bar{t} = 790$.

The time evolution of the rim position \bar{x}_{rim} is presented in Fig. 4.4(a). Within certain time intervals, the rim position $\bar{x}_{\text{rim}}(t)$ is well approximated by a power law $\bar{x}_{\text{rim}} \sim \bar{t}^\alpha$. The spreading exponents α extracted from the data presented in Fig. 4.4(a) fall in the range 0.35-0.47, depending on the aspect ratio ε and the time interval for which a power law relation was fitted. For sufficiently large \bar{h}_{drop} , the numerically obtained spreading exponents are in excellent agreement with the experimental value of around 0.48 for solution deposition [86]. Moreover, we found that the spreading exponent is independent of the initial concentration \bar{C}_0 . Similar observation was reported for the experimental results.

The solid lines in Fig. 4.4(c) represent the time evolution of the rim height $\bar{h}_{\text{max}}(\bar{t})$ for different values of \bar{h}_{drop} . The rapid increase of $\bar{h}_{\text{max}}(\bar{t})$ for $\bar{t} \lesssim 2$ represents the rim formation in the early stage of the spreading process. Several local maxima in $\bar{h}_{\text{max}}(\bar{t})$ are observed. As in the case of insoluble surfactant discussed in Chapter 3, the maximum around $\bar{t} = 20$ is due to the decay of transverse surface tension gradients.

Figure 4.4(d) illustrates the occurrence of a fingering instability for $\bar{h}_{\text{drop}} = 5$ at time $\bar{t} = 790$. The general morphology and the formation of two main fingers is in good qualitative agreement with the experimental observation in Fig. 4.5.

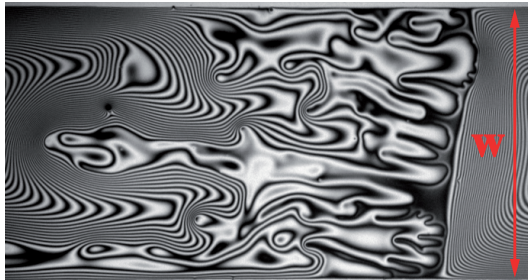


Figure 4.5: Microscope image of fingering instability observed after solution deposition of SDS onto glycerol rivulet for $h_0 = 1.63 \mu\text{m}$, $w = 1.5 \text{ mm}$ and $t = 542 \text{ s}$. Image taken from [86], courtesy of David Sinz.

For $\bar{h}_{\text{drop}} = 5$ time $\bar{t} = 790$ coincides with the onset of the late-stage increase of \bar{h}_{max} as indicated with the downward-oriented arrow in Fig. 4.4(c) for the curve with red circles. We therefore conclude that the spreading of the deposited droplet and the subsequent finger formation enhance the surfactant transport across the crater region and thereby boost the rim propagation. Larger values of \bar{h}_{drop} induce larger increases in \bar{h}_{max} , and this increase in the rim height is also observed sooner.

4.3.2 Continuous surfactant supply

Figure 4.6 (a,b) shows the time evolution of the height profile $\bar{h}(\bar{x}, \bar{y} = 0, \bar{t})$ and surfactant bulk concentration $\bar{C}(\bar{x}, \bar{y} = 0, \bar{t})$ at the rivulet center line, for param-

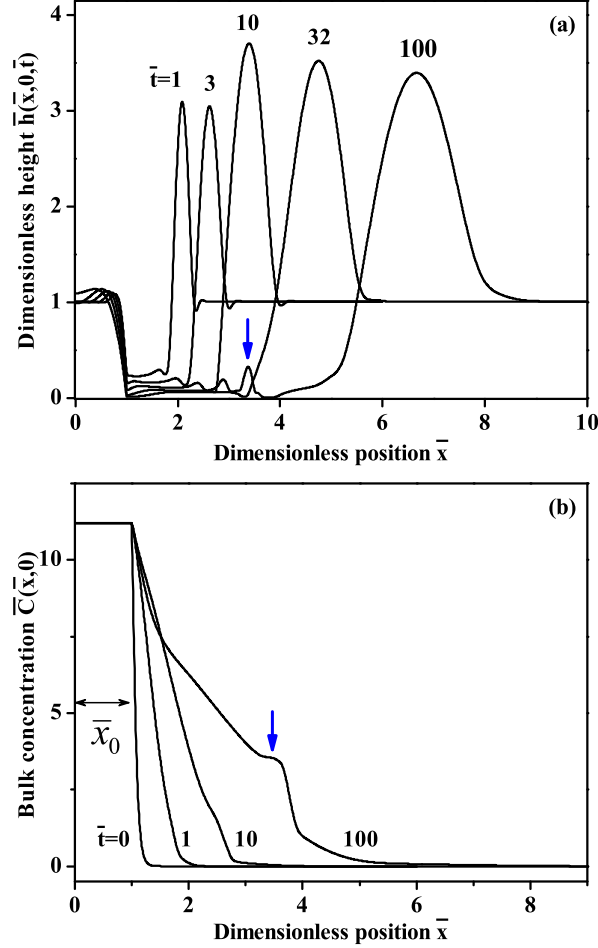


Figure 4.6: (a) Evolution of centerline height profile $\bar{h}(\bar{x}, \bar{y} = 0, \bar{t})$ for continuous surfactant supply. (b) Dimensionless surfactant bulk concentration $\bar{C}(\bar{x}, \bar{y} = 0, \bar{t})$. All results have been obtained for parameter values $\bar{x}_0 = 1$, $\varepsilon = 0.005$, $h_0 = 10 \mu\text{m}$, $\bar{C}_0 = 11.2$, $\bar{\Gamma}_0 = 0.92$, $K = 1000$, $\beta = 0.06$, $\text{Pe}_s = 1000$, $\text{Pe}_b = 100$, $\text{Bo} = 0$.

eters $\bar{x}_0 = 1$ and $\bar{C}_0 = 11.2$. In Fig. 4.7 we present the dimensionless position and maximum height of the rim for two different cases with values of $\bar{x}_0 = 0$ and $\bar{x}_0 = 1$. The essential difference between these two cases is the absence or presence of trapped liquid in the deposition region. In the case of $\bar{x}_0 = 1$ the spreading exponent $\alpha = 0.41$, fitted in the interval $500 < \bar{t} < 1000$, is in excellent agreement with the experimental results reported in [86].

The rim height evolution for $\bar{x}_0 = 1$ is qualitatively similar to the case of finite supply. However, the maximum rim height in Fig. 4.7(b) is significantly larger

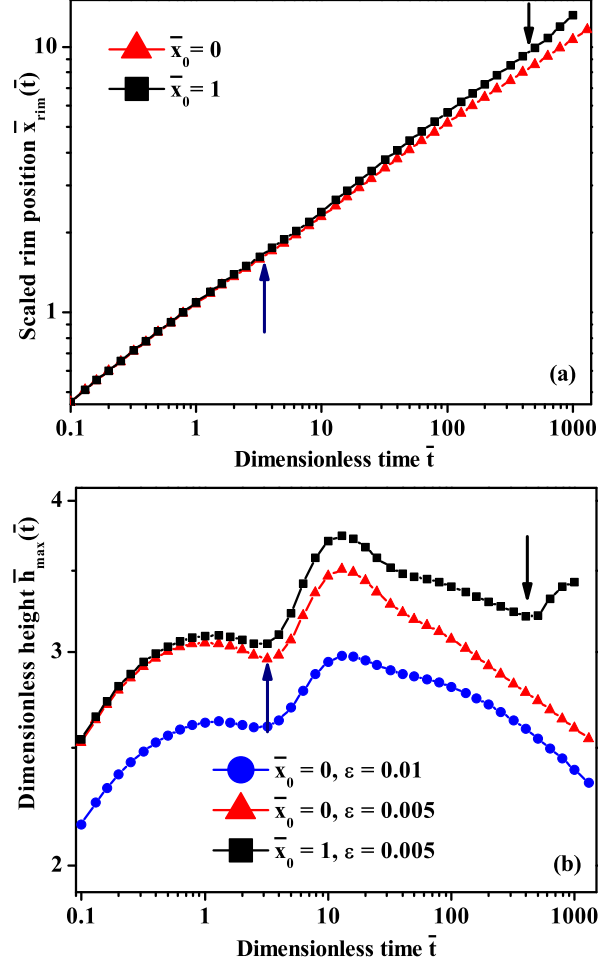


Figure 4.7: Dimensionless rim position and maximum height vs dimensionless time for rivulets with continuous supply of soluble surfactant with $h_0 = 10 \mu\text{m}$, $\bar{C}_0 = 11.2$, $\bar{\Gamma}_0 = 0.92$, $K = 1000$, $\beta = 0.06$, $\text{Pe}_s = 1000$, $\text{Pe}_b = 100$, $\text{Bo} = 0$.

than in the case of $\bar{h}_{\text{drop}} = 0$ in Fig. 4.4(c). The crater formation and extreme film thinning close to the perimeter of the surfactant deposition region at $\bar{x} = \bar{x}_0$ temporarily trap sub-phase liquid in that region [43]. Part of this trapped liquid is continuously released in the later stages of the spreading process, and undergoes a fingering instability as shown in Fig. 4.8. The rise in the rim height at $\bar{t} = 400$ in the case of $\bar{x}_0 = 1$ [as indicated by the downward-oriented arrow in Fig. 4.7(b)] is preceded by this expulsion and subsequent finger formation. This process is analogous to the phenomenon described in the previous section for the case of solution deposition, with the temporarily trapped liquid playing the role of the

deposited solution droplet.

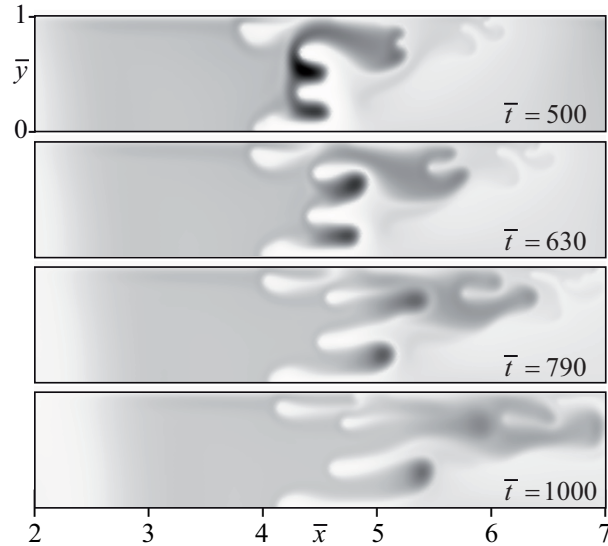


Figure 4.8: Numerical simulation of fingering instability for rivulets with continuous supply of soluble surfactant with $\bar{x}_0 = 1$, $\varepsilon = 0.01$, $h_0 = 10 \mu\text{m}$, $\bar{C}_0 = 11.2$, $\bar{\Gamma}_0 = 0.92$, $K = 1000$, $\beta = 0.06$, $\text{Pe}_s = 1000$, $\text{Pe}_b = 100$, $\text{Bo} = 0$.

In the case of $\bar{x}_0 = 0$, the spreading exponent $\alpha = 0.32$, extracted from the data in Fig. 4.7(a) in the interval $10 < \bar{t} < 1000$, is smaller than both for the case of continuous supply and the case of finite surfactant supply with $\bar{x}_0 = 1$. For $\bar{x}_0 = 0$, extreme thinning in the crater region near $\bar{x} = 0$ effectively cuts off the surfactant supply to the rivulet. As a consequence, no fingering instability occurs and no corresponding increase in the rim height is observed in Fig. 4.7(b).

As mentioned in Section 4.1, we aim at performing a quantitative comparison of the numerical and experimental results. The early stages of the spreading dynamics are influenced by initial conditions and type of surfactant supply used in the numerical model. The details of the surfactant deposition technique in the experiments is also an important factor. Due to these particular reasons, we focus on the later stages of the spreading dynamics. This choice is supported by the fact that exponents from the model with area source of continuous surfactant supply, extracted from the later stages are found to be in good agreement with the experimental results. Moreover, in experiments a fingering instability is observed almost directly after surfactant deposition, while in simulations the onset of its effect on the rim height and propagation rate occurs relatively late, as shown in Figs. 4.7(b) and 4.8. Thus, the early onset of the fingering instability in experiments may cause experimental exponents to be larger than numerical ones at early times.

Previously, we concluded that appropriately chosen initial conditions result in spreading exponents, e.g. derived from data in Fig. 4.7, that are comparable

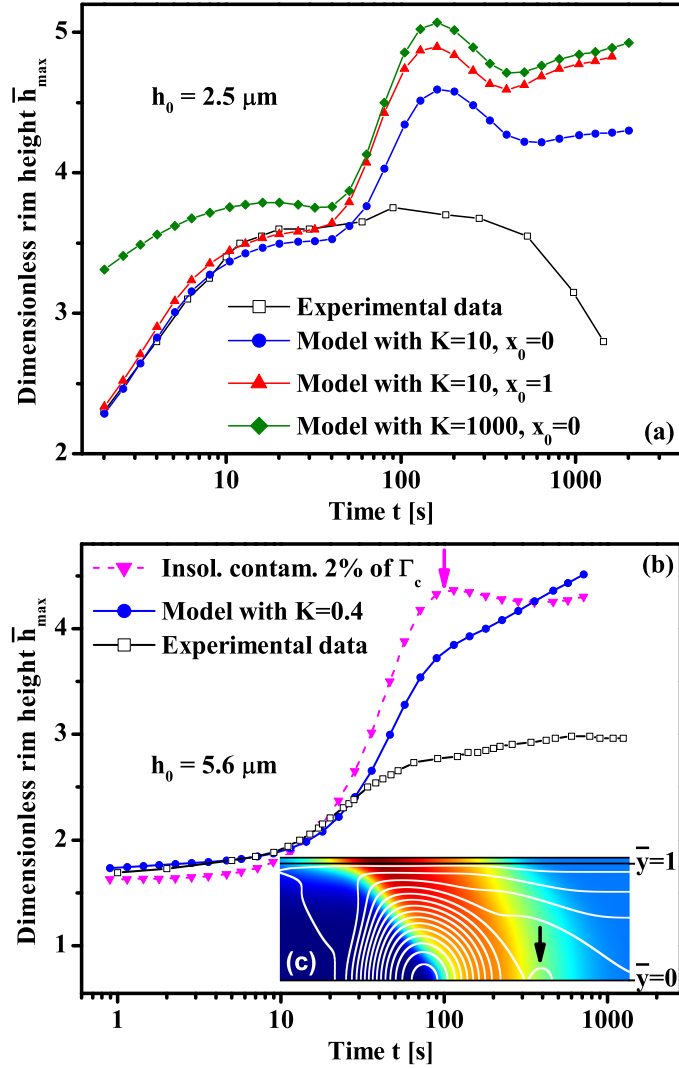


Figure 4.9: (a) Measurement (open symbols, courtesy of David Sinz) and simulations of the temporal evolution of the maximum film height for $h_0 = 2.5 \mu\text{m}$, $w = 1.5 \text{ mm}$, $\bar{C}_0 = 11.2$, $\bar{x}_0 = 1$, $\beta = 0.11$, $\text{Pe}_s = 1000$, $\text{Pe}_b = 1000$, $\text{Bo} = 0$. (b) Measurement (open symbols) and simulations of the temporal evolution of the maximum film height for $h_0 = 5.6 \mu\text{m}$, $w = 1.5 \text{ mm}$, $\bar{C}_0 = 11.2$, $\bar{x}_0 = 0$, $\beta = 0.24$, $K = 10$, $\text{Pe}_s = 1000$, $\text{Pe}_b = 1000$, $\text{Bo} = 0$. (c) False color plot of the insoluble contaminant concentration Γ_{cnt} at $t = 115$ s. The contour lines represent the height profile in the rim region. The parameters used are the same as in (a).

with the experimental results. We also compare the numerical and experimental rim height evolution and its non-monotonic variation. The open symbols in Fig. 4.9(a,b) represent measurements of the time-evolution of the rim height \bar{h}_{\max} for two different values of h_0 . For $h_0 = 5.6 \mu\text{m}$, a slow increase for $t < 10$ s is observed, followed by a more rapid increase around $t = 20$ s and flattening after $t = 400$ s. For $h_0 = 2.5 \mu\text{m}$, a strong increase in h_{\max} is observed for $t < 20$ s, followed by a plateau region with a value of $3.6 h_0 \leq h_{\max} \leq 3.75 h_0$ and a decline of the maximum film height for $t \gtrsim 200$ s.

Since there is no experimental data available for the values of sorption rate constants k_1 and k_2 , we use the sorption coefficient $K = k_2 t_M$ as a fit parameter in our model. Jensen and Grotberg report in [16] that rapidly soluble surfactant with $K = 1000$ induces a much higher rim height than surfactant with slow sorption kinetics, $K = 1$, in one-dimensional surfactant spreading. However, the comparison is limited to the very early stages of the spreading process. In Fig. 4.9(a) we observe that larger K yields higher \bar{h}_{\max} in the early stages of surfactant spreading along a rivulet. However, the effect of K diminishes at later times for $t \gtrsim 100$ s.

For suitably chosen K , the numerical results agree very well with the experimental data, indicated by the solid circles in Fig. 4.9(a,b), at early times. However, quantitative differences are observed later. The fitted values of K result in $k_2 = 1.24$ seconds for $h_0 = 2.5 \mu\text{m}$, and $k_2 = 0.11$ seconds $h_0 = 5.6 \mu\text{m}$, although k_2 as a material parameter should be independent of h_0 . An explanation for this discrepancy, as detailed in Chapter 5, is found in vertical concentration non-uniformities in the rim region that are not accounted for in the lubrication model.

4.3.3 Effect of pre-contamination

Since the presence of surface-active contamination often cannot be avoided during the experiments, Dussaud *et al.* [28] studied the influence of insoluble surface-active contaminants present at the liquid-air interface prior to the surfactant deposition. They found that a low level of pre-contamination has almost no effect on the spreading exponent for an axisymmetric geometry, but causes a noticeable reduction of the rim height.

We implemented pre-contamination in our model as an initially uniform concentration Γ_{cnt} . We assume that the contaminants exhibit the same equations of state as the soluble system SDS/glycerol or the insoluble system oleic acid/glycerol. We consider the following three cases:

- a contamination level of 1% of the CMC of SDS in glycerol;
- a contamination level of 10% of the CMC of SDS in glycerol;
- a contamination level of 2% of the surface concentration scale Γ_c , defined in Chapter 3, for oleic acid on glycerol.

Results for pre-contaminated surfactant spreading in a 1D planar geometry are presented in Fig. 4.10. A higher level of contamination lowers the peak value of

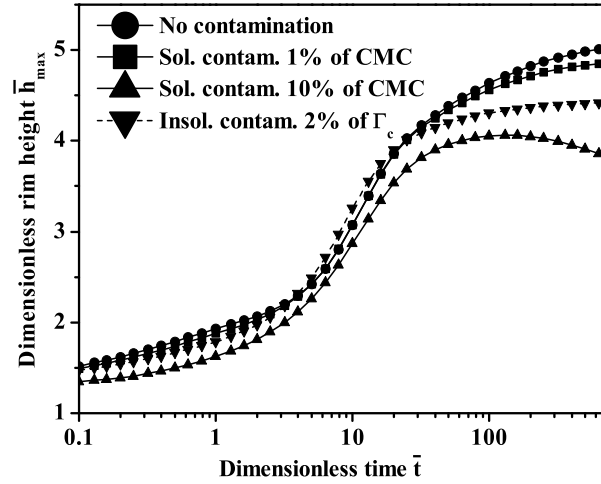


Figure 4.10: Rim height evolution $\bar{h}_{\max}(\bar{t})$ for surfactant spreading with pre-contamination in a one-dimensional Cartesian geometry for $h_0 = 5.6 \mu\text{m}$, $\bar{C}_0 = 11.2$, $\bar{x}_0 = 0$, $\beta = 0.11$, $\text{Pe}_s = 1000$, $\text{Pe}_b = 1000$, and $\text{Bo} = 0$.

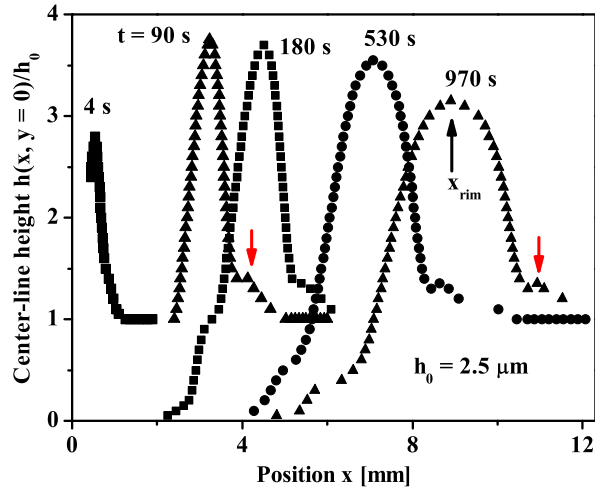


Figure 4.11: Experimental rivulet center-line height profiles for various times after deposition of a pellet of compressed SDS powder onto a glycerol rivulet of initial film height $h_0 = 2.5 \mu\text{m}$. Red arrows indicate the peak in front of the rim which is possible caused by contamination. Image taken from [86], courtesy of David Sinz.

the rim height at later times, whereby the insoluble contaminant has a stronger effect than the soluble one.

This finding motivated us to inquire whether surface-active contamination could

possibly explain the discrepancy between the experimental and numerical results for the rim evolution in Fig. 4.9. Indeed, the curves depicted with solid circles and triangles indicate that an insoluble pre-contamination slightly lowers the rim height at later stages in Fig. 4.9(b), but this is preceded by an overshoot in \bar{h}_{\max} as marked by the arrow.

Lateral surface tension gradients occur during surfactant spreading on uncontaminated rivulets as a consequence of the non-uniform transverse height profile. Liquid is pushed from the center of the rivulet to its edges, corresponding to a flattening of the height profile. When an insoluble contaminant is present, the contaminant concentration in the vicinity of the rim is higher near the rivulet edges than in the rivulet center, as illustrated in Fig. 4.9(c) for an initial insoluble contamination level of $0.02\Gamma_c$. This concentration profile induces a transverse surface tension gradient that pushes liquid from the edges towards the center of the rivulet and causes the overshoot in Fig. 4.9(b) marked by the arrow.

A shallow local maximum ahead of rim is observed in Fig. 4.9(c). This maximum is absent in simulations without contamination, but is frequently observed in experiments, as indicated by the red arrows in Fig. 4.11(a). Despite this qualitative agreement, we conclude, nevertheless, that contamination alone most probably cannot explain the difference between the experimental and numerical rim height profiles in Fig. 4.9.

4.4 Summary and conclusions

We studied the spreading of the soluble surfactant SDS on narrow glycerol rivulets, which experimentally can be made by chemical surface patterning. Our numerical model was based on the lubrication approximation and the assumption of vertically uniform concentration profiles. We monitored the evolution of the liquid height profile after surfactant deposition at the liquid-air interface.

The most prominent morphological feature of the spreading process is the formation of a local maximum in film thickness and its propagation along the rivulet. Its position is well approximated by power-laws $x \sim t^\alpha$. A proper choice of initial and boundary conditions in the numerical models resulted in spreading exponents that are in excellent agreement with the experimental results. The influence of fingering instabilities, commonly observed during the spreading process, on the rim shape and propagation rate was discussed.

The rim height profiles deduced from experiments are in excellent agreement with numerical simulations based on the lubrication approximation at early times, but systematically lower at later stages. The origin of this discrepancy resides in vertical concentration non-uniformities in the rim region that are not accounted for in the lubrication model.

Deformable-domain simulations, based on the full Navier-Stokes and convection-diffusion equations for the bulk liquid, are needed when utilization of lubrication

approximation is not possible. In the next chapter, we describe these simulations in details as well as the effects non-uniform vertical concentration profiles have on spreading dynamics.

Chapter 5

Slow-diffusion soluble surfactant spreading at initially flat liquid-air interfaces

5.1 System description for 1D rectilinear spreading

The assumption of fast vertical diffusion, used in Chapter 4 for modeling of soluble surfactant spreading,

$$\frac{t_d}{t_M} \equiv \frac{h_0^2}{D_b} \frac{4h_0\Delta\gamma_m}{\mu w^2} = \varepsilon^2 \cdot \text{Pe}_b \ll 1 \quad (5.1)$$

is only valid for sufficiently thin films and sufficiently large diffusion coefficients, such that the bulk concentration is, to a good approximation, independent of the vertical coordinate z . For a soluble surfactant, the rim height can be up to 5 times the initial rivulet height, such that Eq. (5.1) may not hold in the rim region even if it is fulfilled in the crater region.

Numerical methods for interfacial flows involving soluble surfactants are computationally quite challenging. A diffuse interface method is presented by Van der Smaan and Van der Graaf [89] for surfactant adsorption onto liquid interfaces. A diffuse-interface implementation including the effects of advection, diffusion and bulk-surface exchange of soluble surfactants was introduced by Teigen *et al.* [90] together with a finite difference technique to model two-phase flows. Their approach is limited to relatively low Peclet numbers. High Peclet numbers pose a

computational challenge due to the occurrence of concentration boundary layers. Recently, Booty and Siegel presented a hybrid numerical method incorporating a perturbation analysis of the layer and a full numerical solution of boundary problem [91].

We consider the one-dimensional spreading of a soluble surfactant, characterized by slow diffusion, on a Newtonian liquid film of the height h_0 . In the case of planar spreading, surfactant is deposited essentially uniformly in a strip of width $2L_0$ and infinite length. We adopt the rectilinear coordinates (x, y, z) with the origin taken at the solid-liquid interface in the center of the surfactant deposition area.

The material system studied in this chapter is the same as the one described in Chapter 4: sodium dodecyl sulfate spreading on glycerol. Consequently, the equation of state used here will be the same as previously

$$\gamma = \gamma_0 + RT\Gamma_\infty \ln \left(1 - \frac{\Gamma}{\Gamma_\infty} \right) \quad (5.2)$$

where $\gamma_0 = 63.5 \text{ mN/m}$ is the surface tension of pure glycerol, R is the universal gas constant, T the absolute temperature, and the maximum surfactant coverage at the interface is $\Gamma_\infty = 4.2 \cdot 10^{-6} \text{ mol/m}^2$.

5.2 Model with the Arbitrary Lagrangian-Eulerian method

To evaluate the impact of vertical concentration non-uniformities, we model surfactant spreading without utilizing the lubrication approximation. Thus, the resulting model can be used for any liquid film thickness and for soluble surfactants with arbitrary diffusion coefficients. We implement the deformability of the computational domain using the Arbitrary Lagrangian-Eulerian (ALE) method. This approach allows for a time-dependent mesh that is suitable for solving problems with moving interfaces. We implement a two-dimensional model for surfactant spreading at liquid-air interface using this method, since computational costs of three-dimensional ALE calculations are too high given the small aspect ratio of our systems.

The flow of the liquid sub-phase is modeled with the full Navier-Stokes and continuity equations for an incompressible Newtonian liquid

$$\rho \left(\frac{\partial \mathbf{u}}{\partial t} + \mathbf{u} \cdot \nabla \mathbf{u} \right) = -\nabla p + \mu \nabla^2 \mathbf{u} + \rho \mathbf{g} \quad (5.3)$$

$$\nabla \cdot \mathbf{u} = 0 \quad (5.4)$$

where $\mathbf{u} = (u_x, u_y, u_z)$ is the fluid velocity, p is the pressure, and ρ and μ are the fluid density and viscosity, respectively.

The surfactant bulk concentration $c(x, z, t)$ evolves according to the convection and diffusion equation

$$\frac{\partial c}{\partial t} + \mathbf{u} \cdot \nabla c = D_b \nabla^2 c \quad (5.5)$$

and surface transport of surfactant $\Gamma(x, z, t)$ adsorbed at the liquid-air interface is described by

$$\frac{\partial \Gamma}{\partial t} + \nabla_s \cdot (\Gamma \mathbf{u}) = D_s \nabla_s^2 \Gamma + J \quad (5.6)$$

where D_b and D_s are the bulk and interface diffusion coefficients, respectively, $J \equiv k_1 c_s - k_2 \Gamma$ is the surfactant flux, with $c_s(x) = c(z = h(x))$ being the bulk concentration evaluated at the surface, and $k_{1;2}$ are the adsorption- and desorption rate constants corresponding to a linearized Langmuir adsorption kinetics model.

Using the surface gradient operator ∇_s defined in Appendix A, Eq. (5.6) is reformulated for a one-dimensional domain $\zeta \in [0, \frac{L}{2}]$. This domain represents the interface via the parametrization

$$x = \zeta, \quad z = h(\zeta) \quad (5.7)$$

with outward unit normal vector

$$\mathbf{n} = \frac{1}{N} \left(-\frac{\partial h}{\partial \zeta}, 1 \right), \quad \text{where } N \equiv \sqrt{1 + \left(\frac{\partial h}{\partial \zeta} \right)^2} \quad (5.8)$$

Taking Eqs. (5.6-5.8) into account, we derive the one-dimensional evolution equation in the limit of vanishing surface diffusion

$$\frac{\partial \Gamma}{\partial t} + \frac{1}{N^2} \left[u_x \frac{\partial \Gamma}{\partial \zeta} + \Gamma \frac{\partial u_x}{\partial \zeta} \right] + \frac{1}{N^2} \frac{\partial h}{\partial \zeta} \left[u_z \frac{\partial \Gamma}{\partial \zeta} + \Gamma \frac{\partial u_z}{\partial \zeta} \right] = J \quad (5.9)$$

The velocity gradients are extruded from the interface $h(x, t)$ to the interval $[0, L/2]$ as follows

$$\frac{\partial u_x}{\partial \zeta} \equiv \left(\frac{\partial u_x}{\partial x} + \frac{\partial h}{\partial x} \frac{\partial u_x}{\partial z} \right) \Big|_{z=h} \quad (5.10)$$

$$\frac{\partial u_z}{\partial \zeta} \equiv \left(\frac{\partial u_z}{\partial x} + \frac{\partial h}{\partial x} \frac{\partial u_z}{\partial z} \right) \Big|_{z=h} \quad (5.11)$$

The BCs for the Navier Stokes equation are

$$u_x(z = 0) = 0 = u_z(z = 0) \quad (5.12)$$

$$u_x(x = 0) = 0 = u_x(x = \frac{L}{2}) \quad (5.13)$$

$$\frac{\partial u_z}{\partial x}(x = 0) = 0 = \frac{\partial u_z}{\partial x}(x = \frac{L}{2}) \quad (5.14)$$

representing no-slip and no-penetration at the solid-liquid interface as well as no flux or symmetry at the lateral domain boundaries. In addition, surface tension gradients at the interface are taken into account via the weak form boundary condition [92]

$$\int \mathbf{w} \cdot \underline{\underline{\sigma}} \cdot \mathbf{n} \, ds = \int \gamma \nabla_s \cdot \mathbf{w} \, ds \quad (5.15)$$

where γ is the surface tension, \mathbf{w} denotes a test function, and $\underline{\underline{\sigma}}$ is the stress tensor.

The BCs for the surfactant surface and bulk concentrations are

$$\frac{\partial c}{\partial z}(z=0) = 0 \quad (5.16)$$

$$-D_b(\mathbf{n} \cdot \nabla c) = k_1 c_s - k_2 \Gamma \quad \text{at } z = h \quad (5.17)$$

$$\frac{\partial c}{\partial x}(x=0) = 0 = \frac{\partial c}{\partial x}(x = \frac{L}{2}) \quad (5.18)$$

$$\frac{\partial \Gamma}{\partial \zeta}(\zeta=0) = 0 = \frac{\partial \Gamma}{\partial \zeta}(\zeta = \frac{L}{2}) \quad (5.19)$$

Equation (5.16) indicates that the surfactant does not adsorb at the solid-liquid interface, while Eq. (5.17) describes bulk-surface exchange. Equations (5.18-5.19) are no-flux or symmetry conditions at the lateral domain boundaries.

In addition, we define the initial surface and bulk concentrations for finite surfactant supply as follows

$$\Gamma(x, 0) = \Gamma_0(1 - \tanh[B(x - L_0)]) \quad (5.20)$$

$$c(x, 0) = c_0(1 - \tanh[B(x - L_0)]) \quad (5.21)$$

where the parameter $B \equiv 10$ defines the steepness of the initial concentration curve, and Γ_0 and c_0 are the initial surface and bulk concentrations in the deposition region.

The system of equations consisting of (5.3-5.5) and (5.10) is solved numerically with the finite element software Comsol Multiphysics 3.5, using transient analysis and ALE mode.

5.3 Weak-diffusion lubrication model

A model based on the lubrication approximation can still be utilized for modeling surfactant spreading subject to a weak diffusion assumption of $Pe_b \sim O(\varepsilon^{-2})$ [74]. A restriction of the model, however, is that the vertical concentration profile is of parabolic shape. We present this model here for comparison with the ALE model that fully resolves arbitrary concentration profiles across film thickness.

When soluble surfactant spreading is characterized by weak bulk diffusion with $Pe_b \sim O(\varepsilon^{-2})$, the convection and diffusion equation Eq. (5.5) is simplified, after

scaling, to [74]

$$\frac{\partial \bar{C}}{\partial \bar{t}} + \bar{u} \frac{\partial \bar{C}}{\partial \bar{x}} + \bar{w} \frac{\partial \bar{C}}{\partial \bar{z}} = \frac{1}{\varepsilon \text{Pe}_b} \frac{\partial^2 \bar{C}}{\partial \bar{z}^2} \quad (5.22)$$

with the boundary conditions

$$J = K(\bar{C} - \bar{\Gamma}) = -\frac{\partial \bar{C}}{\partial \bar{z}} \frac{1}{\varepsilon^2 \text{Pe}_b \beta}, \quad \text{at } \bar{z} = \bar{h}(x, t) \quad (5.23)$$

$$\frac{\partial \bar{C}}{\partial \bar{z}} = 0, \quad \text{at } \bar{z} = 0 \quad (5.24)$$

The scaling formulas used to derive the above equations are the following

$$\bar{x} \equiv \frac{x}{L_0}, \quad \bar{y} \equiv \frac{y}{L_0}, \quad \bar{t} \equiv \frac{t}{t_M} \equiv t \frac{h_0 \Delta \gamma_m}{\mu L_0^2} \quad (5.25)$$

$$\bar{p} \equiv \frac{p L_0^2}{h_0 \Delta \gamma_m}, \quad \bar{\Gamma} \equiv \frac{\Gamma}{\Gamma_\infty}, \quad \bar{C} \equiv \frac{k_1 C}{k_2 \Gamma_\infty} \quad (5.26)$$

The surfactant concentration is expanded into a sum of two components

$$\bar{C} = \bar{a}_0(\bar{x}, \bar{t}) + \bar{a}_2(\bar{x}, \bar{t}) \left(\frac{\bar{z}^2}{\bar{h}^2} - \frac{1}{3} \right) \quad (5.27)$$

where the first component is independent of z , thus represents the vertically averaged concentration, and the second component yields zero when vertically averaged.

Applying boundary conditions (5.24), we obtain

$$\bar{a}_2(\bar{x}, \bar{t}) = \frac{K(\bar{\Gamma} - \bar{a}_0)}{2 [K/3 + 1/(\varepsilon^2 \text{Pe}_b \beta \bar{h})]} \quad (5.28)$$

An evolution equation for \bar{a}_0 is then derived, and together with the remaining lubrication equations, similarly as in Chapter 4, it forms the following system

$$\frac{\partial \bar{h}}{\partial \bar{t}} + \bar{\nabla} \left[\frac{1}{2} (\bar{h}^2 \bar{\nabla} \bar{\gamma}) - \frac{\varepsilon^2}{3} \bar{h}^3 \bar{\nabla} \bar{p} \right] = 0 \quad (5.29)$$

$$\begin{aligned} \frac{\partial \bar{\Gamma}}{\partial \bar{t}} + \bar{\nabla} \left[\bar{h} \bar{\Gamma} \bar{\nabla} \bar{\gamma} - \frac{\varepsilon^2}{2} \bar{h}^2 \bar{\Gamma} \bar{\nabla} \bar{p} - \frac{1}{\text{Pe}_s} \bar{\nabla} \bar{\Gamma} \right] \\ = K (\bar{a}_0 - \bar{\Gamma}) + \frac{K^2 (\bar{\Gamma} - \bar{a}_0)}{3 [K/3 + 1/(\varepsilon^2 \text{Pe}_b \beta \bar{h})]} \end{aligned} \quad (5.30)$$

$$\begin{aligned} \frac{\partial \bar{a}_0}{\partial \bar{t}} + \left[\frac{\bar{h}}{2} \bar{\nabla} \bar{\gamma} - \frac{\varepsilon^2}{3} \bar{h}^2 \bar{\nabla} \bar{p} \right] \bar{\nabla} \bar{a}_0 \\ = \frac{K (\bar{\Gamma} - \bar{a}_0)}{\varepsilon^2 \text{Pe}_b \bar{h}^2 [K/3 + 1/(\varepsilon^2 \text{Pe}_b \beta \bar{h})]} \end{aligned} \quad (5.31)$$

$$\bar{p} = -\bar{\gamma} \bar{\nabla}^2 \bar{h} + \text{Bo} \bar{h} + \bar{\Pi} \quad (5.32)$$

$$\bar{\gamma} = \frac{1}{\Delta \gamma_m} (\gamma_0 + RT \Gamma_\infty \ln(1 - \bar{\Gamma})) \quad (5.33)$$

where we introduced dimensionless parameters

$$\varepsilon \equiv \frac{h_0}{L_0}, \quad \text{Bo} \equiv \frac{\rho g L_0^2}{\Delta \gamma_m}, \quad \text{Pe}_s \equiv \frac{h_0 \Delta \gamma_m}{\mu D_s} \quad (5.34)$$

$$\text{Pe}_b \equiv \frac{h_0 \Delta \gamma_m}{\mu D_b}, \quad \beta \equiv \frac{k_1}{k_2 h_0}, \quad K \equiv k_2 t_M \quad (5.35)$$

The boundary conditions are

$$\frac{\partial \bar{\Gamma}}{\partial \bar{x}}(0, \bar{t}) = 0, \quad \frac{\partial \bar{h}}{\partial \bar{x}}(0, \bar{t}) = 0, \quad \frac{\partial \bar{p}}{\partial \bar{x}}(0, \bar{t}) = 0 \quad (5.36)$$

$$\bar{\Gamma}(\bar{L}, \bar{t}) = \bar{\Gamma}_d, \quad \bar{h}(\bar{L}, \bar{t}) = 1, \quad \bar{p}(\bar{L}, \bar{t}) = 0 \quad (5.37)$$

where \bar{L} is the right boundary of the computational domain.

Similarly to Chapter 2, equations from weak-diffusion lubrication model is solved numerically with the finite element software Comsol Multiphysics 3.5, using transient analysis for the general form PDE equation mode.

5.4 Results and discussion: Effect of vertical concentration profile

To elucidate the influence of non-uniform vertical concentration profiles on the rim height evolution, we perform two-dimensional simulations of surfactant spreading accounting for domain deformability using the ALE method. First, we validate the model results by comparing them to lubrication model for which the assumption of fast vertical diffusion $\varepsilon^2 \cdot \text{Pe}_b \ll 1$ holds. Figure 5.1 reveals a perfect agreement of the two models for an initial film height of 10 microns and several values of the bulk diffusion coefficient D_b .

Figure 5.2 shows the height profile $h(x, t = 10 \text{ s})$ and concentration distribution $c(x, z, t = 10 \text{ s})$ for different values of the bulk diffusion coefficient D_b and finite surfactant supply obtained from the ALE based model. A smaller coefficient D_b results in a significantly reduced rim height. Figure 5.2(c) shows the bulk concentration profiles at the rim positions $c(x_{\text{rim}}, z, t = 10 \text{ s})$ for $D_b = 10^{-9}$ and $10^{-11} \text{ m}^2/\text{s}$, which is essentially uniform for the larger and strongly non-uniform for the smaller value of D_b .

In the case of an initial film thickness of $h_0 = 10 \text{ }\mu\text{m}$, the assumption of fast vertical diffusion $\varepsilon^2 \cdot \text{Pe}_b \ll 1$ is not valid anymore for diffusion coefficients smaller than $D_b \approx 3 \cdot 10^{-10} \text{ m}^2/\text{s}$. We want to evaluate whether the lubrication model based on assumption of $\text{Pe}_b \sim O(\varepsilon^{-2})$ and parabolic vertical concentration, defined in Eq. (5.27), provides an accurate description of spreading dynamics. A limitation of this model is that vertical concentration gradients are permitted only when there is a non-zero flux J . In other words, the moment interface and sub-surface are equilibrated, concentration gradients in the bulk disappear.

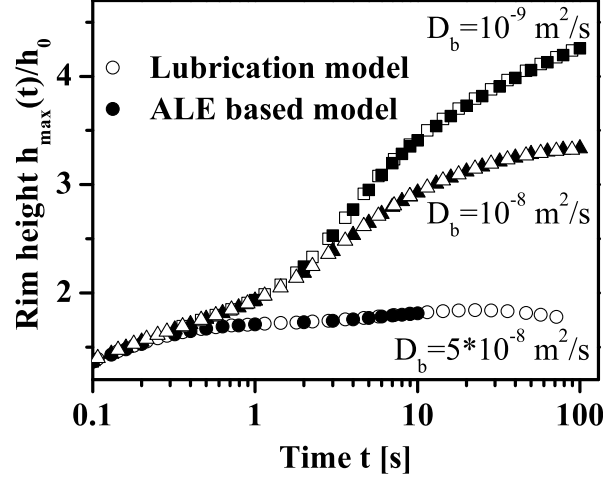


Figure 5.1: Dimensionless rim height $\bar{h}_{\max}(\bar{t})$ as extracted from 2D ALE simulations (solid symbols) and 1D simulations using the lubrication approximation (open symbols) for different values of D_b with parameters $h_0 = 10 \mu\text{m}$, $x_0 = 1 \text{ mm}$, $c_0 = 0.08 \text{ mol/l}$, $k_2 = 1.4 \text{ s}$, $k_1 = 8.2 \cdot 10^{-7} \text{ m/s}$.

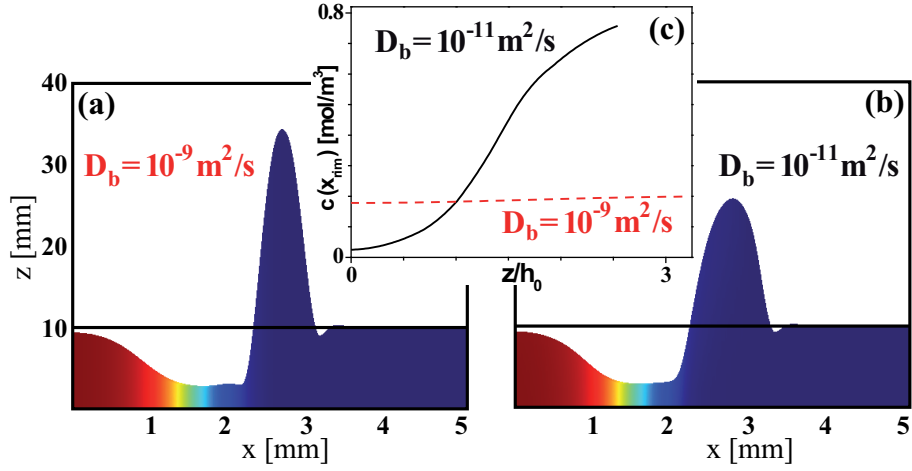


Figure 5.2: (a,b) Height profile and concentration distribution (superimposed colors) at $t = 10 \text{ s}$ as extracted from 2D ALE simulations for (a) $D_b = 10^{-9} \text{ m}^2/\text{s}$ and (b) $D_b = 10^{-11} \text{ m}^2/\text{s}$ and parameter settings $h_0 = 10 \mu\text{m}$, $k_2 = 1.4 \text{ s}^{-1}$ and $k_1 = 8 \cdot 10^{-7} \text{ m/s}$. (c) Vertical concentration profile $c(x = x_{\text{rim}}, z)$ at the rim position at $t = 10 \text{ s}$ extracted from 2D ALE simulations for $D_b = 10^{-9} \text{ m}^2/\text{s}$ and $10^{-11} \text{ m}^2/\text{s}$.

A comparison of the rim height evolution extracted from 2D ALE and 1D lubrication simulations with parabolic vertical bulk concentration is illustrated in Fig. 5.3 for $D_b = 10^{-11} \text{ m}^2/\text{s}$. For comparison, we also include results from the

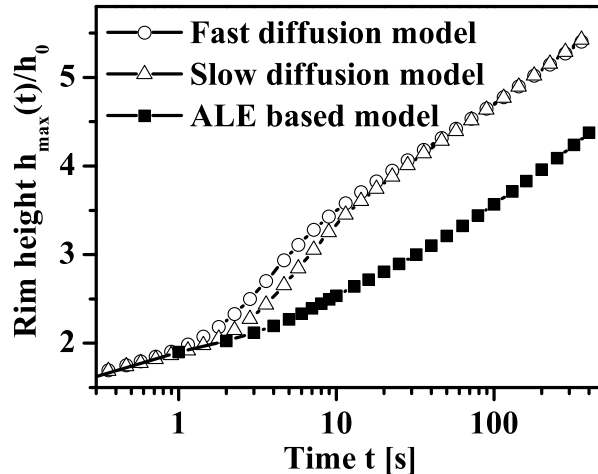


Figure 5.3: Dimensionless rim height $\bar{h}_{\max}(\bar{t})$ as extracted from 2D ALE simulations (solid symbols) and 1D simulations using the lubrication approximation (open symbols) for $D_b = 10^{-11}$ m²/s and parameter settings $h_0 = 10$ μ m, $k_2 = 1.4$ s⁻¹ and $k_1 = 8 \cdot 10^{-7}$ m/s.

lubrication model based on uniform vertical concentration, although this model is not valid for a diffusion coefficient of such a low value. A significant reduction in \bar{h}_{\max} is observed for the full ALE solution relative to the lubrication results for $D_b = 10^{-11}$ m²/s. Thus, lubrication model with parabolic vertical bulk concentration is not capable of reproducing the ALE based model results.

When the value of D_b is sufficiently large such that the vertical diffusion time scale $t_d = h_0^2/D_b$ is smaller than the Marangoni time scale, the bulk concentration remains essentially uniform in the vertical direction. This allows surfactant from the interface to effectively desorb into the entire sub-phase film thickness. On the other hand, for small values of D_b , the bulk concentration has insufficient time to equilibrate, which leads to vertical concentration gradients as shown in Fig. 5.2(c). Consequently, the bulk concentration at the surface is higher, and the amount of surfactant desorbed from the interface is reduced for smaller D_b . This means that for dynamical reasons the surfactant effectively partitions less into the bulk, and exhibits, similarly to insoluble surfactants, significantly lower rim height.

Assuming uniform vertical concentration profiles, Jensen and Grotberg [16] studied the effect of the surface-bulk partitioning parameter β , which they termed degree of solubility, on the rim height for the two cases of β . First case with $\beta \rightarrow \infty$ – an effectively insoluble surfactant, and second case with $\beta = 1$ – a ‘highly soluble’ surfactant. They observed that changing the value of $\beta = 1$ to ∞ induced a significant reduction in the rim height \bar{h}_{\max} .

In our simulations, the parameter β varies only due to varying initial height h_0 , since the ratio k_1/k_2 is fixed for a specific surfactant. However, we argue

that the imbalance in time-scales $t_d > t_M$ in our ALE-based simulations 'dynamically' induces a similar effect as increasing β and thus leads to a reduction in the rim height. We thus conclude that accounting for vertical concentration non-uniformities may significantly improve the agreement between numerical and experimental rim height profiles for a soluble surfactant spreading at non-flat liquid-air interfaces.

5.5 Summary and conclusions

In this chapter, we discussed the spreading of a soluble surfactant with slow diffusion coefficient on a liquid-air interfaces by employing two different numerical models. The first model is based on the full Navier-Stokes equation and convection-diffusion equations for bulk- and surface surfactant transport, accounts for domain deformability and allows for vertically non-uniform concentration profiles. The second model is based on the lubrication approximation and the assumption of vertically parabolic concentration profiles. We monitored the evolution of the liquid height profile after non-uniform surfactant deposition at the liquid-air interface.

The most prominent morphological feature of the spreading process is the formation of a local maximum in film thickness and its propagation along the rivulet. The two studied models give different results with respect to height morphology. The origin of this discrepancy was identified with the help of deformable-domain simulations and resides in vertical concentration non-uniformities in the rim region that are not accurately accounted for in the lubrication model.

Chapter 6

Soluble surfactant spreading at liquid-liquid interfaces

6.1 System description

After our study of insoluble/soluble surfactant spreading at liquid-air interfaces, the next step is to consider surfactant spreading at liquid-liquid interfaces. As a first step towards accounting for confinement in porous media, we study two liquids between flat solid plates and assume that surfactant is soluble in the lower liquid phase. For sufficiently thin films and surfactants with fast diffusion, we employ a similar approach as in the lubrication model used for the spreading along liquid-air interface (Chapter 4). For thicker films and/or slow diffusion the Arbitrary Lagrangian-Eulerian (ALE) method is used (Chapter 5).

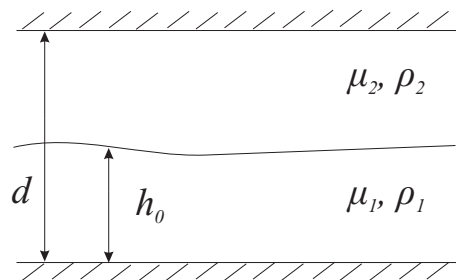


Figure 6.1: Geometry for two immiscible liquids between flat solid plates.

In this chapter we consider two systems: 1D rectilinear spreading along an initially planar liquid-liquid interface and 2D spreading with the lower liquid confined to a hydrophilic stripe in a form of a rivulet. Figure 6.1 depicts the 1D geometry

of two liquids with continuous interface between parallel and flat solid plates. We denote the viscosity of the lower liquid as μ_1 , and the viscosity of the upper liquid as μ_2 . The ratio of the viscosities of the liquids is defined as $\mu_{21} \equiv \mu_2/\mu_1$. Analogously, we define the density ratio $\rho_{21} \equiv \rho_2/\rho_1$. The distance between the solid plates is d . We assume that the liquid-liquid interface is flat initially with the film thickness of the lower liquid denoted by h_0 . Surfactant is deposited as a strip of width $2L_0$ and infinite length.

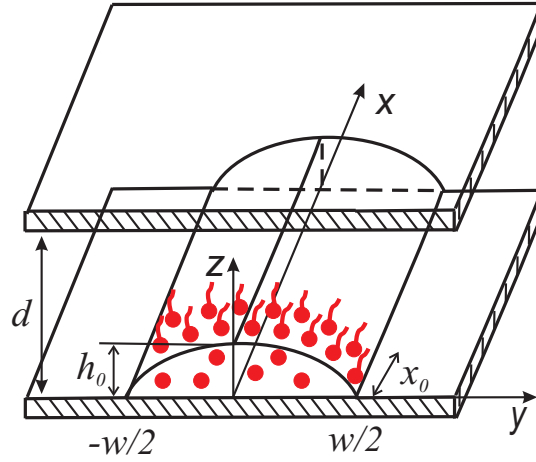


Figure 6.2: Sketch of the rivulet geometry with initial soluble surfactant distribution for two liquids between solid plates. For symmetry reasons only half of the rivulet is shown.

To study the effect of spatial confinement, we consider a thin liquid film (rivulet) that is chemically confined to a hydrophilic stripe of width w and length L on a substrate as shown in Fig. 6.2. A second flat and parallel substrate is located at a distance d and the space between lower liquid surface and second substrate is filled with an immiscible liquid. Surfactant is deposited in the center region of the rivulet, i.e. $[-x_0, x_0] \times [-w/2, w/2]$.

For comparison with experimental data, we consider the following material system: glycerol as the lower liquid and dodecane as the upper liquid. The viscosity ratio for this system is $\mu_{21} = 0.002$, while the density ratio is $\rho_{21} = 0.8$. Our surfactant of choice is sodium dodecyl sulfate (SDS) that is soluble in glycerol. The non-linear equation of state derived from the Gibbs adsorption isotherm follows as

$$\gamma = \gamma_0 + RT\Gamma_\infty \ln \left(1 - \frac{C}{k_2\Gamma_\infty/k_1 + C} \right) \quad (6.1)$$

where C is the equilibrated bulk concentration, R is the universal gas constant and T the absolute temperature, Γ_∞ is the maximum surface coverage, and $k_{1,2}$ are adsorption and desorption rate constants, respectively.

We use Eq. (6.1) to fit the experimental data in Fig. 6.3 for the dependence of surface tension on bulk concentration, $\gamma(C)$, which yields the parameter values $\Gamma_\infty = 4 \cdot 10^{-6} \text{ mol/m}^2$ and $k_2/k_1 = 2.27 \cdot 10^6 \text{ m}^{-1}$. Since we do not take into account the presence of surfactant micelles, the validity of this model is restricted to concentrations below the so-called critical micelle concentration. The maximum spreading pressure is determined as $\Delta\gamma_m = 20 \text{ mN/m}$.

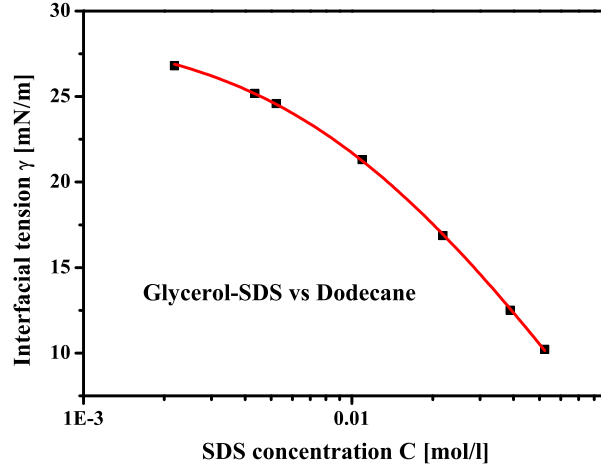


Figure 6.3: Interfacial tension of glycerol/dodecane as a function of bulk concentrations of SDS in glycerol. Symbols represent experimental data by David Sinz. The solid line represents the fit using Eq. (6.1).

6.2 Governing equations and boundary conditions

6.2.1 Lubrication model

A derivation of the lubrication equation for the liquid-liquid interface $h(x, t)$ in the absence of surfactants is presented in [87]. The model is valid for systems with small aspect ratio $\varepsilon \equiv h_0/L_0 \ll 1$, where L_0 is the length-scale of the surfactant deposition area. For the rivulet geometry the characteristic length-scale is chosen to be $L_0 = w/2$. As in the case of a liquid-air interface, we extend the model by adding convection-diffusion equations for surfactant surface and bulk transport and a constitutive relation for dependence of surface tension on concentration.

Using the scaled variables

$$\bar{x} \equiv \frac{x}{L_0}, \quad \bar{y} \equiv \frac{y}{L_0}, \quad \bar{h} \equiv \frac{h}{h_0}, \quad \bar{t} \equiv \frac{t}{t_M} \equiv t \frac{h_0 \Delta\gamma_m}{\mu_1 L_0^2} \quad (6.2)$$

$$\bar{p} \equiv \frac{p L_0^2}{h_0 \Delta\gamma_m}, \quad \bar{\Gamma} \equiv \frac{\Gamma}{\Gamma_\infty}, \quad \bar{C} \equiv \frac{k_1 C}{k_2 \Gamma_\infty} \quad (6.3)$$

the dimensionless system of equations for rectilinear surfactant spreading at liquid-liquid interface is

$$\frac{\partial \bar{h}}{\partial \bar{t}} + \bar{\nabla} [Q_2 \bar{\nabla} \bar{\gamma} + Q_1 \varepsilon^2 \bar{\nabla} \bar{p}] = 0 \quad (6.4)$$

$$\begin{aligned} \frac{\partial \bar{\Gamma}}{\partial \bar{t}} + \bar{\nabla} \left[R_2 \bar{\Gamma} \bar{\nabla} \bar{\gamma} - R_1 \varepsilon^2 \bar{\Gamma} \bar{\nabla} \bar{p} - \frac{1}{\text{Pe}_s} \bar{\nabla} \bar{\Gamma} \right] \\ = K (\bar{C} (1 - \bar{\Gamma}) - \bar{\Gamma}) \end{aligned} \quad (6.5)$$

$$\begin{aligned} \frac{\partial \bar{C}}{\partial \bar{t}} + [Q_2 \bar{\nabla} \bar{\gamma} + Q_1 \varepsilon^2 \bar{h}^2 \bar{\nabla} \bar{p}] \bar{\nabla} \bar{C} - \frac{1}{\text{Pe}_b \bar{h}} \bar{\nabla} [\bar{h} \bar{\nabla} \bar{C}] \\ = \frac{\beta K}{\bar{h}} (\bar{\Gamma} - \bar{C} (1 - \bar{\Gamma})) \end{aligned} \quad (6.6)$$

$$\bar{p} = -\bar{\gamma} \bar{\nabla}^2 \bar{h} + \text{Bo} (1 - \rho) \bar{h} + \bar{\Pi} \quad (6.7)$$

$$\bar{\gamma} = \frac{1}{\Delta \gamma_m} (\gamma_0 + RT \Gamma_\infty \ln (1 - \bar{\Gamma})) \quad (6.8)$$

where $\bar{\Pi}$ is the disjoining pressure described in Section 4.2, and the following functions have been introduced

$$Q_1(\bar{h}) \equiv \bar{h}^3 (d - \bar{h})^3 (d + \bar{h}(\mu_{21} - 1)) / (3D) \quad (6.9)$$

$$Q_2(\bar{h}) \equiv R_1(\bar{h}) = \bar{h}^2 (d - \bar{h})^2 (\bar{h}^2 (\mu_{21} - 1) - d(d - 2\bar{h})) / (2D) \quad (6.10)$$

$$R_2(\bar{h}) \equiv \bar{h} (d - \bar{h}) ((d - \bar{h})^3 + \bar{h}^3 \mu_{21}) / D \quad (6.11)$$

$$D \equiv (d - \bar{h})^4 + h \mu_{21} (\bar{h}^3 (\mu_{21} - 2) + 4d\bar{h}^2 - 6d^2\bar{h} + 4d^3) \quad (6.12)$$

The dimensionless parameters were introduced above

$$\varepsilon \equiv \frac{h_0}{L_0}, \quad \text{Bo} \equiv \frac{\rho g L_0^2}{\Delta \gamma_m}, \quad \text{Pe}_s \equiv \frac{h_0 \Delta \gamma_m}{\mu_1 D_s} \quad (6.13)$$

$$\text{Pe}_b \equiv \frac{h_0 \Delta \gamma_m}{\mu_1 D_b}, \quad \beta \equiv \frac{k_1}{k_2 h_0}, \quad K \equiv k_2 t_M \quad (6.14)$$

As boundary and initial conditions we use the same expressions as for finite supply or continuous supply defined in Section 4.2.1 and Section 4.2.2 for soluble surfactant spreading at liquid-air interface.

6.2.2 Model with Arbitrary Lagrangian-Eulerian method

The assumption of fast vertical diffusion $t_{\text{diffusion}}/t_{\text{Marangoni}} \ll 1$ is only valid for sufficiently thin films and large diffusion coefficients, such that the bulk concentration is, to a good approximation, independent of the vertical coordinate z . To evaluate the consequences of vertical concentration non-uniformities, we model surfactant spreading without utilizing the lubrication approximation.

Systems with domain deformability are modeled in Comsol Multiphysics using the Arbitrary Lagrangian-Eulerian (ALE) method. This approach allows moving meshes suitable for solving problems with moving liquid-liquid interface. Using this method, we implement a two-dimensional model for surfactant spreading at liquid-liquid interfaces for systems with small aspect ratio, since computational costs of three-dimensional ALE calculations are too high. However, 3D modeling of thicker films is possible with this method.

The flow of the liquid sub-phases are modeled with the full Navier-Stokes equations

$$\rho \left(\frac{\partial \mathbf{u}}{\partial t} + \mathbf{u} \cdot \nabla \mathbf{u} \right) = -\nabla p + \mu \nabla^2 \mathbf{u} + \rho \mathbf{g} \quad (6.15)$$

$$\nabla \cdot \mathbf{u} = 0 \quad (6.16)$$

where $\mathbf{u} = (u_x, u_y, u_z)$ is the fluid velocity, p is the pressure, and $\rho = \rho_{1,2}$ and $\mu = \mu_{1,2}$ are the upper or lower fluid density and viscosity, respectively.

The surfactant bulk concentration in the lower liquid evolves according to the convection and diffusion equation

$$\frac{\partial c}{\partial t} + \mathbf{u} \cdot \nabla c = D_b \nabla^2 c, \quad (6.17)$$

where D_b is the bulk diffusion coefficient, and surface transport of surfactant adsorbed at the liquid-air interface is described by

$$\frac{\partial \Gamma}{\partial t} + \nabla_s \cdot (\Gamma \mathbf{u}) = D_s \nabla_s^2 \Gamma + J \quad (6.18)$$

where D_b and D_s are the bulk and interface diffusion coefficients, J is the surfactant flux between interface and bulk, and ∇_s is the surface gradient operator.

If liquid-liquid interface is represented via a parametrization of the form $\{x = \zeta, z = h(\zeta)\}$, which precludes overhanging multi-valued interface locations described by a slope of the interface smaller than 90° everywhere, then equation (6.18) can be reformulated for a one-dimensional domain $\zeta \in [0, \frac{L}{2}]$ as following

$$\frac{\partial \Gamma}{\partial t} + \frac{1}{N^2} \left[u_x \frac{\partial \Gamma}{\partial \zeta} + \Gamma \frac{\partial u_x}{\partial \zeta} \right] + \frac{1}{N^2} \frac{\partial h}{\partial \zeta} \left[u_z \frac{\partial \Gamma}{\partial \zeta} + \Gamma \frac{\partial u_z}{\partial \zeta} \right] = J \quad (6.19)$$

The velocity gradients are extruded from the interface $h(x, t)$ to the interval $[0, \frac{L}{2}]$ as follows

$$\frac{\partial u_x}{\partial \zeta} \equiv \left(\frac{\partial u_x}{\partial x} + \frac{\partial h}{\partial x} \frac{\partial u_x}{\partial z} \right) \Big|_{z=h} \quad (6.20)$$

$$\frac{\partial u_z}{\partial \zeta} \equiv \left(\frac{\partial u_z}{\partial x} + \frac{\partial h}{\partial x} \frac{\partial u_z}{\partial z} \right) \Big|_{z=h} \quad (6.21)$$

If the above mentioned parametrization of the free interface is not possible, we apply a weak formulation, i.e an integral form, of the interface equation

$$\int_{\partial\Omega(t)} \tilde{\Gamma} \frac{\partial\Gamma}{\partial t} ds = \int_{\partial\Omega(t)} \nabla_s \tilde{\Gamma} \cdot (\Gamma \mathbf{u} - D_s \nabla_s \tilde{\Gamma}) ds$$

where $\partial\Omega(t)$ represents the liquid-liquid interface, and $\tilde{\Gamma}$ is a test function in Comsol Multiphysics. Details of the weak form implementation of convective-diffusive transport at free interfaces in Comsol can be found in [88]. Even though the work is limited to insoluble surfactants at liquid-air interface, we can use the approach in our modeling.

The boundary conditions for the Navier Stokes equation are

$$u_x(z=0) = 0 = u_z(z=0) = u_x(z=d) = 0 = u_z(z=d) \quad (6.22)$$

$$u_x(x=0) = 0 = u_x(x=\frac{L}{2}) \quad (6.23)$$

$$\frac{\partial u_z}{\partial x}(x=0) = 0 = \frac{\partial u_z}{\partial x}(x=\frac{L}{2}) \quad (6.24)$$

representing no-slip and no-penetration at the solid-liquid interface as well as no flux or symmetry at the lateral domain boundaries. In addition, surface tension gradients at the interface are taken into account via the weak form boundary condition

$$\int \mathbf{w} \cdot (\underline{\sigma}_1 - \underline{\sigma}_2) \cdot \mathbf{n} ds = \int \gamma \nabla_s \cdot \mathbf{w} ds \quad (6.25)$$

where γ is the surface tension, \mathbf{w} denotes a test function, and $\underline{\sigma}_{1,2}$ are the stress tensors for liquid 1 and liquid 2, respectively.

The BCs for the surfactant surface and bulk concentrations are

$$\frac{\partial c}{\partial z}(z=0) = 0 \quad (6.26)$$

$$-D_b(\mathbf{n} \cdot \nabla c) = k_1 c_s - k_2 \Gamma \quad \text{at } z = h \quad (6.27)$$

$$\frac{\partial c}{\partial x}(x=0) = 0 = \frac{\partial c}{\partial x}(x=\frac{L}{2}), \quad \frac{\partial \Gamma}{\partial \zeta}(\zeta=0) = 0 = \frac{\partial \Gamma}{\partial \zeta}(\zeta=\frac{L}{2}) \quad (6.28)$$

Equation (6.26) implies no adsorption at the solid-liquid interface, Eq. (6.27) describes bulk-surface exchange. Equations (6.28) are no-flux or symmetry conditions at the lateral domain boundaries.

For initial conditions we use the same expressions as for finite supply or continuous supply defined in Section 4.2.1 and Section 4.2.1 for soluble surfactant spreading at liquid-air interface.

6.3 Results and discussion

We begin with one-dimensional spreading at the interface of two liquids between parallel plates. Figure 6.4 shows the time evolution of the height profile for a system with finite surfactant supply of length $x_0 = 0.75$ mm and input parameters: $h_0 = 10 \mu\text{m}$, $d = 10h_0$, $\rho_{21} = 0.8$ and $\mu_{21} = 0.2$, which means that liquid 2 is less viscous than liquid 1. We use the same diffusion coefficient D for interface and bulk of about $2.3 \cdot 10^{-10} \text{ m}^2/\text{s}$.

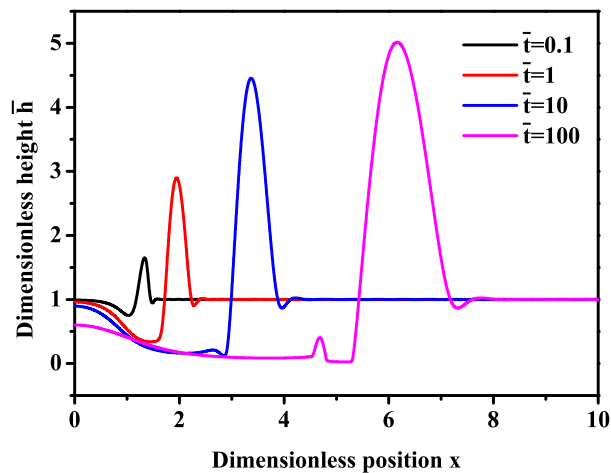


Figure 6.4: Dimensionless height profile for liquid-liquid interface with finite surfactant supply and $h_0 = 10 \mu\text{m}$, $d = 10$, $\mu = 0.2$, $\rho_{21} = 0.8$, $x_0 = w/2$, $C_0 = 0.055 \text{ mol/l}$ and $\Gamma_0 = 2.4 \cdot 10^{-5} \text{ mol/m}^2$, $k_2 = 1.4 \text{ 1/s}$.

If we make the upper liquid less viscous, the behavior of the height profile changes. When viscosity of liquid 2 is smaller, the advancing rim at a certain time becomes wider. For a more systematic study, we plot in Fig. 6.5 the speed of advance of the rim and in Fig. 6.6 the rim height for different values of μ_{21} and both finite and continuous at the interface surfactant supply.

We also conclude that at later stage of height evolution, the initial film height h_0 has no effect on the power law behavior of the rim position, but smaller initial height results in a slightly higher rim. Larger values of μ_{21} give slightly lower spreading exponents. The model with continuous surfactant supply of length $x_0 = 0.75$ mm only at the interface (and no surfactant present in the bulk at $t = 0$) yields a higher spreading exponent at the later stage and a lower rim height overall. At early times there is a distinct plateau region in both rim position and height, which we attribute to the effects of surfactant desorption from the interface into the bulk, where no surfactant was present initially.

To elucidate the influence of non-uniform vertical concentration profiles on the rim height evolution, we perform two-dimensional simulations of surfactant spread-

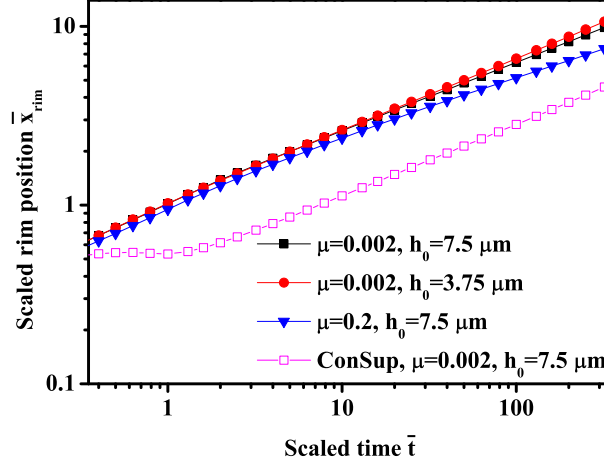


Figure 6.5: Rim position (closed symbols) as a function of dimensionless time for liquid-liquid interface with finite surfactant supply and $d = 10h_0$, $\rho_{21} = 0.8$, $C_0 = 0.055$ mol/l and $\Gamma_0 = 2.4 \cdot 10^{-5}$ mol/m², $k_2 = 1.4$ s⁻¹. Open symbols represent rim position for continuous surfactant supply of length x_0 at the interface as defined by Eq. (4.17) and no surfactant present in the bulk at $t = 0$.

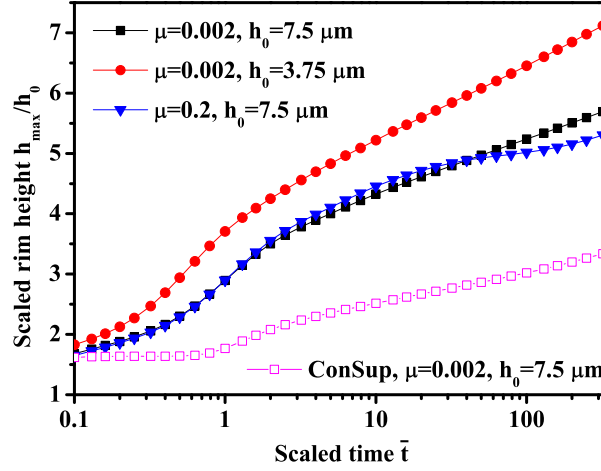


Figure 6.6: Rim height (closed symbols) as a function of dimensionless time for liquid-liquid interface with finite surfactant supply and $d = 10h_0$, $\rho_{21} = 0.8$, $C_0 = 0.055$ mol/l and $\Gamma_0 = 2.4 \cdot 10^{-5}$ mol/m², $k_2 = 1.4$ s⁻¹. Open symbols represent rim height for continuous surfactant supply of length x_0 at the interface as defined by Eq. (4.17) and no surfactant present in the bulk at $t = 0$.

ing accounting for domain deformability using the ALE method. We use the value $\mu_{21} = 0.002$ for viscosity ratio, which represents the material system of glycerol

as lower liquid and dodecane as upper liquid. For such low viscosity ratio we expect results similar to surfactant spreading at a liquid-air interface presented in Chapter 5.

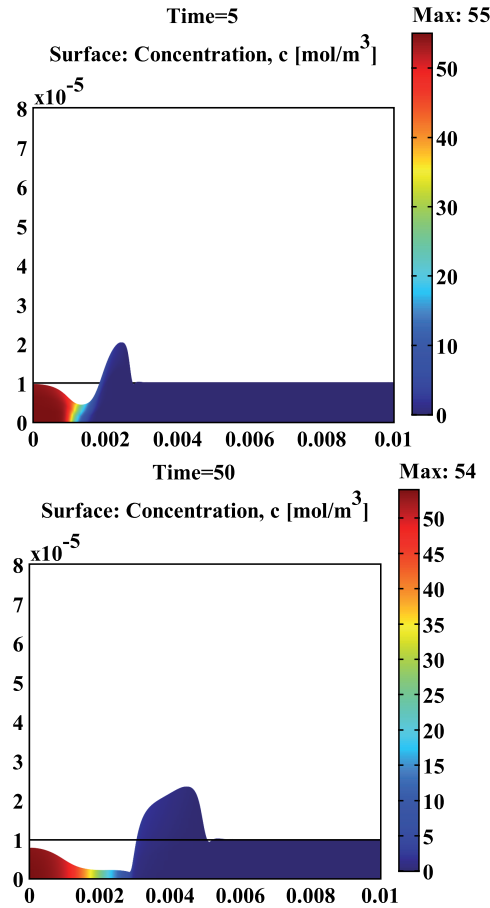


Figure 6.7: Height profile and concentration distribution (superimposed colors) at $t = 5$ and 50 s as extracted from 2D ALE simulations with finite surfactant supply and parameter settings $D_b = 10^{-12}$ m²/s, $h_0 = 10$ μ m, $k_2 = 1.4$ s⁻¹.

Figure 6.7 shows the height profile $h(x)$ and concentration distribution $c(x, z)$ at times $t = 5$ s and $t = 50$ s for the bulk diffusion coefficient $D_b = 10^{-12}$ m²/s. The complete rim height evolution extracted from 2D ALE is depicted in Fig. 6.8 for two values of diffusion coefficient, namely, $D_b = 10^{-12}$ m²/s and $D_b = 10^{-11}$ m²/s. Again, we notice that the rim height is significantly smaller than the typical values observed in Fig. 6.6, which is a consequence of vertical concentration non-uniformities. The smaller diffusion coefficient value yields significantly lower rim height in Fig. 6.8.

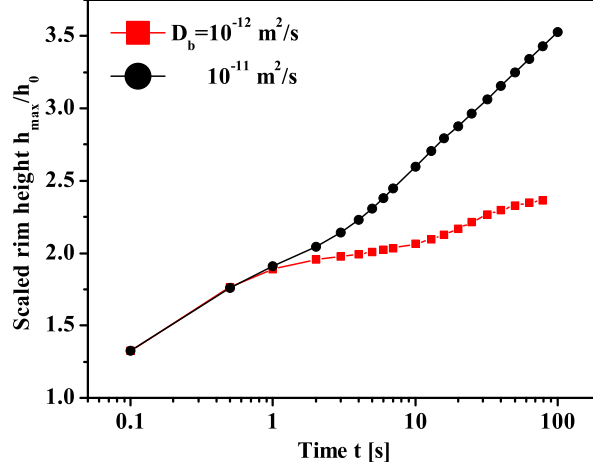


Figure 6.8: Dimensionless rim height $\bar{h}_{\max}(\bar{t})$ as extracted from 2D ALE simulations of surfactant spreading at liquid-liquid interface with $D_b = 10^{-12} \text{ m}^2/\text{s}$ and $D_b = 10^{-11} \text{ m}^2/\text{s}$, $h_0 = 10 \text{ }\mu\text{m}$, $k_2 = 1.4 \text{ s}^{-1}$.

The effect of spatial confinement is taken into account in the model for surfactant spreading at liquid-liquid rivulet geometry. The model utilizes the lubrication approximation and, thus, is only suitable for thin liquid films and sufficiently fast bulk diffusion. Two different initial height values, $h_0 = 11.2 \text{ }\mu\text{m}$ and $h_0 = 5.6 \text{ }\mu\text{m}$ are used in our simulations with finite surfactant supply.

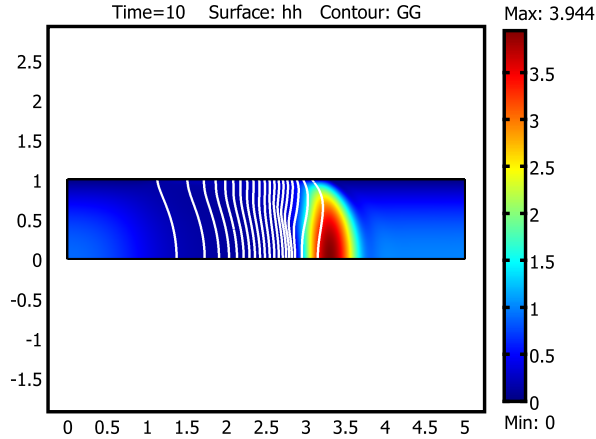


Figure 6.9: Rim formation at $\bar{t} = 10$ for liquid-liquid rivulet interface with finite surfactant supply and $h_0 = 5.6 \text{ }\mu\text{m}$, $d = 80 \text{ }\mu\text{m}$, $\mu_{21} = 0.002$, $\rho_{21} = 0.8$, $x_0 = w/2$, $C_0 = 0.055 \text{ mol/l}$ and $\Gamma_0 = 2.4 \cdot 10^{-5} \text{ mol/m}^2$, $k_2 = 1.4 \text{ s}^{-1}$.

An example of the rim formation at $\bar{t} = 10$ for the initial height of $h_0 = 5.6 \mu\text{m}$ is shown in Fig. 6.9 with superimposed contours of surface concentration.

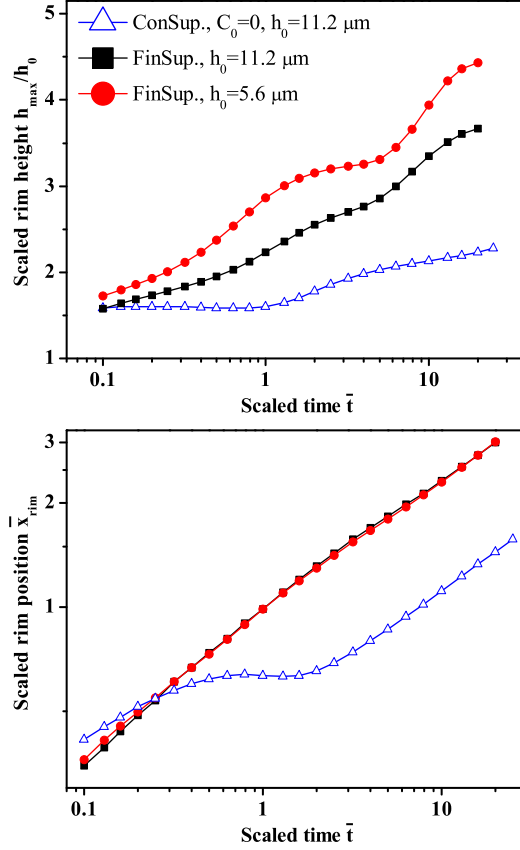


Figure 6.10: Rim height and position as a function of dimensionless time for liquid-liquid rivulet interface with finite surfactant supply (closed symbols) and continuous supply at the interface (open symbols) with $d = 80 \mu\text{m}$, $\mu_{21} = 0.002$, $\rho_{21} = 0.8$, $w = 1.5 \text{ mm}$, $x_0 = w/2$, $C_0 = 0.055 \text{ mol/l}$ and $\Gamma_0 = 2.4 \cdot 10^{-5} \text{ mol/m}^2$, $k_2 = 1.4 \text{ s}^{-1}$, and $\text{Pe}_s = \text{Pe}_b = 1000$.

In Fig. 6.10 we observe that smaller initial height results in larger rim height. The rim position on the other hand is independent of initial height.

Figure 6.10 also shows the results of continuous surfactant supply at the interface, while initial bulk concentration is defined as zero, $\bar{C}_0 = 0$. As time progresses, surfactant desorbs from the interface into the bulk and diffuses there. Initially, this situation results in lower spreading exponent since we lose surfactant from the interface into the bulk due to desorption. Later on, for $\bar{t} > 3$, it is characterized by the same value of spreading exponent as the finite surfactant supply case. The

most profound effect is observed in the rim height value. Continuous supply at the interface, with initially no surfactant in the bulk, yields much lower rim height values, as shown in Fig. 6.10.

Next, we compare the numerical and experimental rim height evolution and its non-monotonic variation. Numerical results are obtained for continuous supply at the interface and finite supply in the bulk with initial concentration

$$\bar{C}(\bar{x}, 0) = \frac{\bar{C}_0^f}{2}(1 - \tanh[B(\bar{x} - \bar{x}_0)]) \quad (6.29)$$

The choice of surfactant supply is motivated by the results for spreading at liquid-air interfaces. Numerical values for the rim height are higher at the later stage compared to the experimental results obtained for systems with similar aspect ratio. Our findings indicate that diffusion of SDS in the glycerol bulk is much slower than consistent with the assumption of a uniform vertical concentration profile that our lubrication model is based upon. We try to compensate it by introducing lower averaged concentration in the bulk.

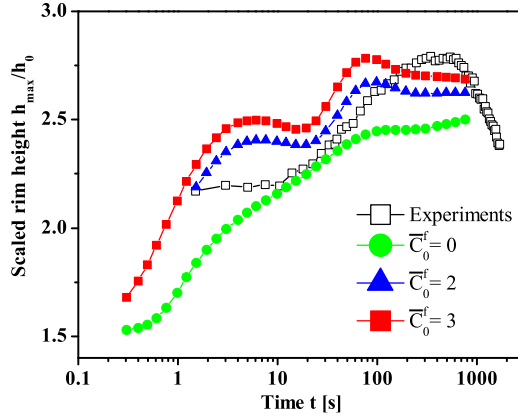


Figure 6.11: Measurement and simulations of the temporal evolution of the maximum film height for rivulet with $h_0 = 7.9 \mu\text{m}$, $w = 1.5 \text{ mm}$, $\bar{x}_0 = 1$, $\bar{\Gamma}_0 = 0.92$, $\beta = 0.056$, $\text{Pe}_s = 183$, $\text{Pe}_b = 183$, $k_2 = 2 \text{ s}^{-1}$. Numerical results were obtained for continuous supply at the interface and finite supply in the bulk with initial concentration defined in Eq. 6.29.

Figure 6.11 shows comparison of the numerical (closed symbols) and experimental (open symbols) rim height \bar{h}_{max} for initial rivulet center-height of $h_0 = 7.9 \mu\text{m}$. While the differences are not drastic for certain values of \bar{C}_0^f , good quantitative agreement can not be reached with the proposed lubrication model and the type of surfactant supply.

6.4 Summary and conclusions

In this chapter, we studied the spreading of a soluble surfactant at liquid-liquid interfaces. Two systems were studied: 1) an initially flat liquid-liquid interface between parallel plates and 2) narrow glycerol rivulets surrounded by dodecane, again in the gap space between parallel plates. We developed two different numerical models. The first model is based on the lubrication approximation and the assumption of vertically uniform concentration profiles. The second model is based on the full Navier-Stokes equation and convection-diffusion equations for bulk- and surface surfactant transport and allows for vertically non-uniform concentration profiles. The novel ALE based model allows us to simulate systems with very slow diffusion, i.e. for values of the Peclet number up to approximately 10^5 .

We monitored the evolution of the liquid height profile after surfactant deposition. Similarly to surfactant spreading at air-liquid interfaces, the most prominent feature of the process is the formation of a local maximum in film thickness and its propagation away from the deposition region. Its position is well approximated by power-laws $x \sim t^\alpha$. We conclude that the larger the difference between lower and upper liquid viscosity, the higher the spreading exponent and rim height.

A comparison of experiment rivulet height profiles with the lubrication type simulations yielded similar conclusions as for spreading at liquid-air interface, because in both cases the material system used in the experiments was characterized by a very small viscosity ratio. Relatively good agreement between experimental and numerical results can be obtained with the lubrication model that combines continuous surfactant supply at the interface with finite supply in the bulk.

Chapter 7

Surfactant-induced delay of leveling of inkjet-printed patterns

7.1 Introduction and system description

The leveling dynamics of thickness variations in thin liquid films has been studied extensively in the context of ripples and other irregularities in solution-deposited coatings and molten glass films, as well as brush marks in paint layers [93, 44, 94, 95, 96, 97, 98, 99, 100, 101, 102, 103, 104, 105, 106, 108, 107, 109, 110, 111, 112, 113]. Orchard presented a Fourier series solution of the Stokes equation for the leveling process, considering both surface tension and gravity as the driving forces and allowing for temporal variations of surface tension and viscosity [93, 44]. Retaining the time-derivatives in the Navier-Stokes equation, Woo considered one-dimensional and axisymmetric disturbances on molten glass surfaces [95]. Degani and Gutfinger in addition conducted time-resolved measurements of the leveling dynamics [99] and presented a numerical solution of governing equations for the case of large amplitudes [100]. Khesghi and Scriven focused their attention on large amplitude disturbances and performed a disturbance expansion up to second order aside from numerical simulations [104]. Stillwagon and Larson studied the leveling of thin films deposited on topographically patterned substrates [105]. Overdiep [101, 102] Wilson [107] and Eres *et al.* [113] considered the influence of evaporation as well as concentration- and surface tension gradients on the leveling process. The effect of surfactants has been studied by Schwartz *et al.* [109, 110].

In the past decade inkjet printing has matured as a flexible deposition technique for laterally structured coatings of solvent- or melt-based ink formulations [114, 115, 116, 117, 118, 119, 120, 121, 122]. For many applications it is desirable to

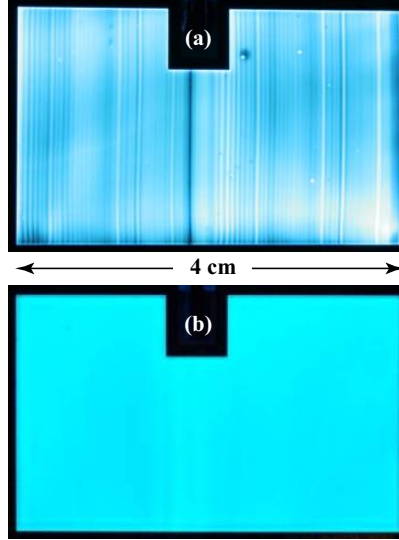


Figure 7.1: Inkjet-printed organic light emitting diode devices based on Merck LiviluxTM light emitting polymer and an (a) large and (b) optimized linepitch. (Image taken from [129], courtesy of Maosheng Ren.)

obtain a smooth film without ripples or other morphological traces of the individual droplets that had originally been deposited. The degree of leveling and the final ink morphology that are crucial for print quality typically improves with time. On the other hand, ink redistribution effects, e.g. due to equilibration of capillary pressure or surface energy differences on the substrate, are usually unwanted. As an illustrative example, Fig. 7.1 shows the light emission pattern of two organic light emitting diode (OLED) devices fabricated by inkjet printing using an Agfa OrgaconTM hole injection layer and Merck LiviluxTM light emitting polymer. A large line-pitch d_l in Fig. 7.1(a) caused the occurrence of striations, i.e. individual printed lines are distinguishable in the light output. After process optimization a perfectly homogeneous light emission is visible in Fig. 7.1(b).

A piezoelectrically actuated inkjet printhead with a certain diameter and a nozzle-pitch can be used for deposition. The drop volume V_d and drop ejection frequency f_d are kept constant. The distance between individual inkjetted droplets along the y -direction is denoted $d_d = U_{\text{sub}}/f_d$. The cross-sectional area (volume per unit length) $A_{sl} = V_d/d_d = V_d f_d / U_{\text{sub}}$ of a *single* inkjet-printed line can be adjusted by means of the substrate speed U_{sub} . The width of a *single* printed line w_{sl} depends on the ink-substrate contact angle θ as illustrated in Fig. 7.2(a). For uniform, narrow *single* lines $w_{sl} \ll \ell_c \equiv \sqrt{\gamma/(\rho g)}$, the equilibrium line-width is given by [123] $w_{sl} = 2 \sin \theta \sqrt{A_{sl}/(\theta - \sin \theta \cos \theta)}$. For narrow and *thin* single lines, i.e. if $h_{sl} \ll w_{sl}$, the cross-sectional profile is to good approximation parabolic and thus $A_{sl} = \frac{2}{3} h_{sl} w_{sl}$. The lateral separation d_l of neighboring inkjet-printed lines

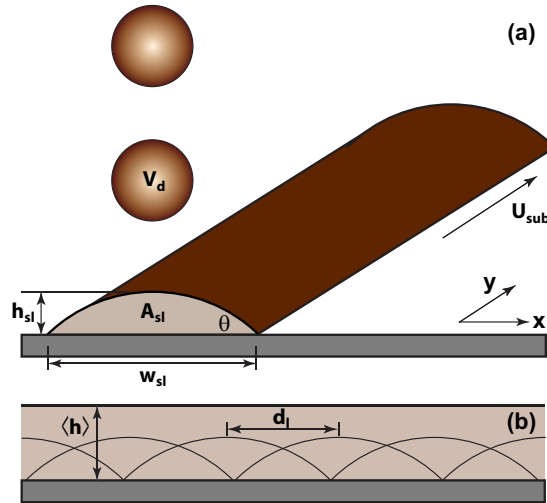


Figure 7.2: Definition of geometric parameters. (a) Inkjet droplets of volume V_d impinge on an impenetrable substrate moving with velocity U_{sub} in the y -direction to form a single line of width w_{sl} , centerline height h_{sl} and cross-sectional area A_{sl} . (b) Wide lines and thin films of average film thickness $\langle h \rangle$ can be formed by controlled coalescence of single lines deposited with a spacing $d_l < w_{sl}$. (Image taken from [129], courtesy of Anton A. Darhuber.)

is varied by adjusting the azimuthal orientation of the printhead with respect to the direction of substrate motion. Disregarding end effects, the average height of a multi-line is given by $\langle h \rangle = A_{sl}/d_l$. Here, h_{sl} is the center height of a printed *single* line, g the gravitational acceleration and ℓ_c the so-called capillary length, a material parameter that typically ranges between 1.5 and 3 mm. For dimensions below ℓ_c , the influence of gravity on the leveling and redistribution process can to good approximation be neglected for horizontally oriented substrates.

Generally, patterns are printed such that the center-to-center distance of neighboring lines is smaller than the line-width, $d_l < w_{sl}$, which guarantees a certain minimum overlap [Fig. 7.2(b)]. Moreover, d_d is kept much smaller than d_l , such that the leveling dynamics in the printing direction (y -axis) proceed much faster than perpendicular to it. For this reason, only the lateral leveling along the x -axis will be considered and the ink thickness profile $h(x, y, t)$ is assumed to be independent of y . For industrial applications it is desirable to maximize d_l and U_{sub} , since then a larger area can be patterned with the same number of nozzles in shorter time.

In order to optimize the layer formation, quantitative models are desirable. In Section 7.2 we introduce the theoretical models we applied for the description of the ink redistribution dynamics in the presence of insoluble and soluble surfactants. In Section 7.3.1 we first consider their influence on the leveling rate of one-dimensional ripples and striations. Subsequently we discuss the equilibration

dynamics of inkjet-printed multi-lines in Section 7.3.2.

7.2 Theoretical models and numerical simulations

The two principal stages of the leveling process of a multi-line are illustrated qualitatively in Fig. 7.3. The initial configuration is approximated by a linear superposition of truncated parabolas

$$h(x, t=0) = \sum_{n=-4}^4 \max \left(0, h_{sl} \left[1 - \frac{4(x-nd_l)^2}{w_{sl}^2} \right] \right), \quad (7.1)$$

which exhibits thickness variations corresponding to approximately 20% of the average film thickness $\langle h \rangle$. After a time t_{lev} the ripples in the initial ink thickness profile have leveled and the central part of the multi-line has an essentially uniform thickness. After a time t_{red} the height profile has adopted an approximately parabolic shape (if the total linewidth $w < \ell_c$), which corresponds to the liquid equilibrium conformation characterized by an x -independent pressure inside the line.[124] We define the leveling time t_{lev} as the time when the ripple amplitude has decayed to 10% of its initial value. The definition of the redistribution time t_{red} will be given in Section 7.3.2. The aim of this manuscript is to identify the process window, such that leveling can be achieved while redistribution is avoided, resulting in inkjet-printed multi-lines with a homogeneous layer thickness.

The width of a multi-line w depends on the number of lines N , d_l and w_{sl} and may change in time as a consequence of ink spreading or retraction. We shall assume, however, that the contact lines remain pinned e.g. as a consequence of contact angle hysteresis. Moreover, although the viscosity gradually increases during the solvent evaporation process, we consider the case of a constant Newtonian viscosity and neglect any influence of the solvent volatility.

7.2.1 Insoluble surfactants

In the case of small aspect ratios $\varepsilon \equiv h_{sl}/w_{sl} \ll 1$, the so-called lubrication approximation [38] can be applied to describe the leveling dynamics. In this limit, the equations describing the evolution of the height profile and the surfactant surface distribution of an *insoluble* surfactant are [125, 12]

$$\frac{\partial h}{\partial t} + \frac{\partial}{\partial x} \left(\frac{h^2}{2\mu} \frac{\partial \gamma}{\partial \Gamma} \frac{\partial \Gamma}{\partial x} - \frac{h^3}{3\mu} \frac{\partial p}{\partial x} \right) = 0 \quad (7.2)$$

$$\frac{\partial \Gamma}{\partial t} + \frac{\partial}{\partial x} \left(\frac{h\Gamma}{\mu} \frac{\partial \gamma}{\partial \Gamma} \frac{\partial \Gamma}{\partial x} - \frac{h^2\Gamma}{2\mu} \frac{\partial p}{\partial x} - D_s \frac{\partial \Gamma}{\partial x} \right) = 0 \quad (7.3)$$

$$p = -\gamma \frac{\partial^2 h}{\partial x^2} + \rho gh, \quad (7.4)$$

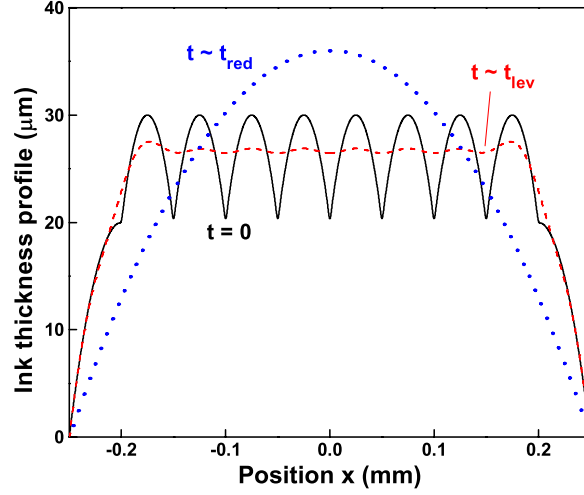


Figure 7.3: Exemplary ink thickness profile of $N = 9$ overlapping inkjetted lines for parameters $w_{sl} = 100 \mu\text{m}$, $d_l = 50 \mu\text{m}$, $h_{sl} = 20 \mu\text{m}$, and $\Gamma(x, t=0) = 0$. The black solid line represents the initial distribution immediately after deposition ($t=0$). The dashed and dotted lines represent after the height profile after leveling ($t \approx t_{lev}$) and after capillary redistribution ($t \approx t_{red}$), respectively.

where Γ is the surfactant surface concentration, p the augmented pressure [38] and D_s the surface diffusion constant. An assumption implicit in Eqs. (7.2-7.4) is that the substrate is oriented horizontally with its surface normal parallel to the positive z -direction, whereas gravity acts in the negative z -direction. This formalism can be applied when the ink-substrate contact angle is not too large, an upper limit [126] is on order of 30° .

For the evaluation of the surface tension γ , we have used the equation of state

$$\gamma = \gamma_\infty + \Pi_{\max} \exp\left(-A \left[\frac{\Gamma}{\Gamma_c}\right]^2\right) \quad (7.5)$$

depicted in Fig. 7.4. The parameter values were chosen as $\gamma_\infty = 39 \text{ mN/m}$, $\Pi_{\max} = 24 \text{ mN/m}$, $\Gamma_c = 3.5 \mu\text{l/m}^2$ and $A = 6.125$, which to good approximation resembles the equation of state of oleic acid on glycerol [127, 43].

For numerical simulations of the leveling dynamics we first use the initial conditions

$$h(x, t=0) = \langle h \rangle + a_0 \cos\left(\frac{2\pi}{\lambda} x\right) \quad (7.6)$$

$$\Gamma(x, t=0) = \Gamma_0, \quad (7.7)$$

i.e. we initially consider only the center region close to $x=0$ as sketched in Fig. 7.3. In a second step we discuss end-effects in the vicinity of the contact lines in Sec-

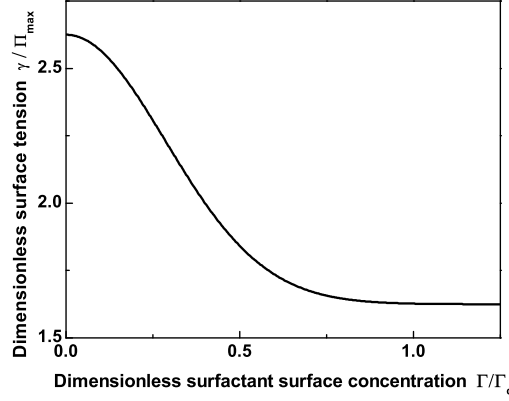


Figure 7.4: Non-dimensional equation of state of an exemplary insoluble surfactant.

tion 7.3.2. Here a_0 is the amplitude of the ink thickness variations and λ the ripple wavelength, which is determined by d_l . Equation (7.7) corresponds to a uniform initial surfactant concentration along the surface, which means that Marangoni stresses are *induced* by the leveling process. Although non-uniform initial surfactant distributions after ink-jet deposition are conceivable, the authors are not aware of any existing experimental, theoretical or numerical data regarding $\Gamma(x, t=0)$.

Equations (7.2)-(7.5) were non-dimensionalized using the following scales

$$\bar{x} \equiv x/\lambda, \quad \bar{h} \equiv h/\langle h \rangle, \quad \bar{\Gamma} \equiv \Gamma/\Gamma_c, \quad (7.8)$$

$$\bar{p} \equiv p/p_0, \quad \bar{\gamma} \equiv \gamma/\Pi_{\max}, \quad \bar{t} \equiv t/t_O, \quad (7.9)$$

where $p_0 \equiv \gamma a_0/\lambda^2$ and t_O is defined in Eq. (7.10).

7.2.2 Perturbation analysis for small amplitudes and insoluble surfactants

Using a Fourier series solution of the Stokes equation, Orchard [44] derived the expression

$$t_O = \frac{3}{16\pi^4} \frac{\mu}{\gamma} \frac{\lambda^4}{\langle h \rangle^3} \frac{1}{1 + \frac{\rho g \lambda^2}{4\pi^2 \gamma}} \quad (7.10)$$

for the leveling time of long-wavelength ripples on thin liquid films, i.e. in the limit $2\pi\langle h \rangle/\lambda \ll 1$, in the absence of surfactants. This result can also be derived from a linearization of Eqs. (7.2) and (7.4) for the case when the ripple amplitude $a_0 \ll \langle h \rangle$ in Eq. (7.6).

Schwartz *et al.* [109, 110] considered the effects of surfactants on the leveling dynamics for the case of an idealized linear equation of state and when gravitational effects are negligible. We follow their procedure to derive an expression for the

leveling time scale in the presence of surfactants for a realistic, non-linear equation of state and with gravitational effects included. We consider the following harmonic variations of the height profile and surfactant concentration

$$h(x, t) = \langle h \rangle + h_1(t) \cos kx \quad (7.11)$$

$$\Gamma(x, t) = \Gamma_0 + \Gamma_1(t) \cos kx \quad (7.12)$$

$$\gamma(x, t) = \gamma(\Gamma_0) + \frac{\partial \gamma}{\partial \Gamma}(\Gamma_0) \Gamma_1(t) \cos kx \quad (7.13)$$

and determine the time dependence of the amplitudes h_1 and Γ_1 from linearized versions of Eqs. (7.2-7.4), i.e. for the case when $h_1 \ll \langle h \rangle$ and $\Gamma_1 \ll \Gamma_0$. We point out that the Orchard time t_O from Eq. (7.10), which we use for non-dimensionalizing time in Eqs. (7.9), depends on surface tension $\gamma(\Gamma_0)$ and thus on Γ_0 , i.e. the linearization point in Eqs. (7.12, 7.13). The following system of linear and homogeneous ordinary differential equations results

$$\frac{\partial \bar{h}_1}{\partial \bar{t}} + \frac{1}{2} \frac{-3 \frac{\partial \bar{\gamma}}{\partial \bar{\Gamma}}(\bar{\Gamma}_0)}{(\bar{\gamma}(\bar{\Gamma}_0)k^2 + \rho g / \Pi_{\max})} \bar{\Gamma}_1 + \bar{h}_1 = 0 \quad (7.14)$$

$$\frac{\partial \bar{\Gamma}_1}{\partial \bar{t}} + \frac{-3 \bar{\Gamma}_0 \frac{\partial \bar{\gamma}}{\partial \bar{\Gamma}}(\bar{\Gamma}_0)}{(\bar{\gamma}(\bar{\Gamma}_0)k^2 + \rho g / \Pi_{\max})} \bar{\Gamma}_1 + \frac{3 \bar{\Gamma}_0}{2} \bar{h}_1 + Z \bar{\Gamma}_1 = 0, \quad (7.15)$$

which we solve for the initial conditions $\bar{h}_1(\bar{t}=0) = \bar{a}_0$ and $\bar{\Gamma}_1(\bar{t}=0) = 0$ and find

$$\frac{1}{\bar{a}_0} \bar{h}_1 = \frac{1 + N_-}{N_- - N_+} \exp(N_+ \bar{t}) - \frac{1 + N_+}{N_- - N_+} \exp(N_- \bar{t}) \quad (7.16)$$

$$\bar{\Gamma}_1 = \frac{3 \bar{\Gamma}_0}{2} \frac{\bar{a}_0}{N_- - N_+} (\exp(N_+ \bar{t}) - \exp(N_- \bar{t})), \quad (7.17)$$

where the rate constants N_{\pm} are given by

$$N_{\pm} \equiv -\frac{1}{2} \left(S \pm \sqrt{S^2 - Q \bar{\Gamma}_0 - 4Z} \right) \quad (7.18)$$

and we defined

$$Q \equiv \frac{-3 \frac{\partial \bar{\gamma}}{\partial \bar{\Gamma}}(\bar{\Gamma}_0)}{(\bar{\gamma}(\bar{\Gamma}_0)k^2 + \rho g / \Pi_{\max})} \langle h \rangle^2 \quad (7.19)$$

$$S \equiv 1 + Q \bar{\Gamma}_0 + Z \quad (7.20)$$

$$Z \equiv t_O D_s k^2. \quad (7.21)$$

We note that for $Q = 0$, Eq. (7.16) reduces to the Orchard solution $\bar{h}_1 = \bar{a}_0 \exp(-\bar{t})$. Had we chosen a locally non-uniform initial surfactant distribution $\bar{\Gamma}_1(\bar{t}=0) \neq 0$, then the numerical prefactors of the exponential terms in Eqs. (7.16) and (7.17) would be different, but the rate-constants would remain unaffected.

For most surfactant systems $\frac{\partial \bar{\gamma}}{\partial \Gamma} \leq 0$, which implies that $Q \geq 0$ and that the rate constants N_{\pm} are negative (semi)definite, $N_{\pm} \leq 0$. This corresponds to a decay of both the ripples in the height profile and the surfactant concentration variations in the limit of long times. Since $|N_-| < |N_+|$, the rate constant N_- determines the long-time behavior.

7.2.3 Soluble surfactants

Jensen and Grotberg [15] presented a theoretical model for the dynamics of thin liquid films in the presence of non-uniform distributions of a soluble surfactant. They assumed a linear equation of state $\gamma = \gamma_0 - B\Gamma$ with a positive constant B as well as a linear relation between the surfactant bulk concentration in the liquid film $c(x, y, z, t)$ and the equilibrium surface concentration

$$\Gamma_{\text{eq}} = \frac{k_1}{k_2} c_s(x, y, t) \equiv \frac{k_1}{k_2} c(x, y, z=h, t). \quad (7.22)$$

Here, the adsorption- and desorption rate constants $k_{1,2}$ are defined by a linearized Langmuir equation describing the bulk-surface exchange of surfactant as $J = k_1 c_s - k_2 \Gamma$, where J is the surfactant flux with units of mol/(m²s). Jensen and Grotberg [15] simplified the equation for bulk transport of surfactant

$$\frac{\partial c}{\partial t} + \mathbf{u} \cdot \nabla c = D_b \nabla^2 c, \quad (7.23)$$

for the case of fast vertical diffusion in thin liquid films considering Marangoni stresses as the only driving force

$$\frac{\partial C}{\partial t} - B \frac{h}{2\mu} \frac{\partial \Gamma}{\partial x} \frac{\partial C}{\partial x} = \frac{D_b}{h} \frac{\partial}{\partial x} \left(h \frac{\partial C}{\partial x} \right) - \frac{J}{h}. \quad (7.24)$$

Here \mathbf{u} is the flow velocity, D_b is the bulk diffusion coefficient, and $C \equiv \frac{1}{h} \int_0^h c dz$ the height-averaged bulk concentration. The corresponding surface concentration fulfills the equation

$$\frac{\partial \Gamma}{\partial t} + \frac{\partial}{\partial x} \left[-\frac{h\Gamma}{\mu} B \frac{\partial \Gamma}{\partial x} - D_s \frac{\partial \Gamma}{\partial x} \right] = J, \quad (7.25)$$

with D_s the surfactant surface diffusivity.

We have extended this model by including flows due to pressure gradients, the full non-linear Langmuir equation for bulk-surface exchange as well as the corresponding non-linear equilibrium isotherm

$$J = k_1 C \left(1 - \frac{\Gamma}{\Gamma_{\infty}} \right) - k_2 \Gamma \quad (7.26)$$

$$\frac{\Gamma_{\text{eq}}}{\Gamma_{\infty}} = \frac{k_1 C}{k_2 \Gamma_{\infty} + k_1 C}, \quad (7.27)$$

where Γ_∞ is the maximum surface concentration at complete coverage of the surface. The non-linear equation of state derived from the Gibbs adsorption isotherm[128] follows as

$$\gamma = \gamma(0) + RT\Gamma_\infty \ln \left(1 - \frac{\Gamma}{\Gamma_\infty} \right), \quad (7.28)$$

where R is the universal gas constant and T the absolute temperature. We used Eqs. (7.26) and (7.27) to fit experimental data for the dependence of surface tension on bulk concentration, $\gamma(C)$, for the soluble surfactant sodiumdodecylsulfate (SDS) in glycerol,[86] which yielded the parameters $\Gamma_\infty = 4.2 \cdot 10^{-6}$ mol/m², $k_2/k_1 = 1.7 \cdot 10^6$ m⁻¹ as well as the maximum spreading pressure $\Pi_{\max} = 23.7$ mN/m. Since we do not take the presence of surfactant micelles into account, the validity of this model is restricted to concentrations below the so-called critical micelle concentration (cmc).

We introduce the following scaled variables

$$\hat{p} = \frac{p\lambda^2}{\langle h \rangle \Pi_{\max}}, \quad \hat{\Gamma} = \frac{\Gamma}{\Gamma_s} \quad (7.29)$$

$$\hat{C} = \frac{k_1 C}{k_2 \Gamma_\infty}, \quad \hat{t} = \frac{t}{t_M} = t \frac{\langle h \rangle \Pi_{\max}}{\mu \lambda^2}. \quad (7.30)$$

The scale Γ_s is chosen such that a non-dimensional bulk concentration $\hat{C} = 1$ corresponds to a non-dimensional surface concentration $\hat{\Gamma} = 1$ in the scaled version of Eq. (7.27), i.e. $\Gamma_s = \frac{1}{2}\Gamma_\infty$. We arrive at the following dimensionless equations

$$\begin{aligned} \frac{\partial \hat{\Gamma}}{\partial \hat{t}} + \frac{\partial}{\partial \hat{x}} \left[\bar{h} \hat{\Gamma} \frac{\partial \bar{\gamma}}{\partial \hat{\Gamma}} \frac{\partial \hat{\Gamma}}{\partial \hat{x}} - \frac{\epsilon^2 \text{Bo} \bar{h}^2 \hat{\Gamma}}{2} \frac{\partial \bar{h}}{\partial \hat{x}} - \frac{\epsilon^2 \bar{h}^2 \hat{\Gamma}}{2} \frac{\partial \hat{p}_c}{\partial \hat{x}} \right. \\ \left. - \frac{1}{\text{Pe}_s} \frac{\partial \hat{\Gamma}}{\partial \hat{x}} \right] = K \left[\hat{C} (2 - \hat{\Gamma}) - \hat{\Gamma} \right] \end{aligned} \quad (7.31)$$

$$\begin{aligned} \frac{\partial \hat{C}}{\partial \hat{t}} + \left[\frac{\bar{h}}{2} \frac{\partial \bar{\gamma}}{\partial \hat{\Gamma}} \frac{\partial \hat{\Gamma}}{\partial \hat{x}} - \frac{\epsilon^2 \text{Bo} \bar{h}^2}{3} \frac{\partial \bar{h}}{\partial \hat{x}} - \frac{\epsilon^2 \bar{h}^2}{3} \frac{\partial \hat{p}_c}{\partial \hat{x}} \right] \frac{\partial \hat{C}}{\partial \hat{x}} \\ - \frac{1}{\text{Pe}_b \bar{h}} \frac{\partial}{\partial \hat{x}} \left[\bar{h} \frac{\partial \hat{C}}{\partial \hat{x}} \right] = \frac{\beta K}{2\bar{h}} \left[\hat{\Gamma} - \hat{C} (2 - \hat{\Gamma}) \right] \end{aligned} \quad (7.32)$$

$$\bar{\gamma} = \frac{1}{\Pi_{\max}} \left[\gamma(0) + RT\Gamma_\infty \ln \left(1 - \frac{\hat{\Gamma}}{2} \right) \right]. \quad (7.33)$$

Here, we introduced the capillary pressure $\hat{p}_c \equiv -\bar{\gamma} \frac{\partial^2 \bar{h}}{\partial \hat{x}^2}$ and the following dimen-

sionless parameters

$$\begin{aligned} \epsilon &\equiv \frac{\langle h \rangle}{\lambda}, & \text{Bo} &\equiv \frac{\rho g \lambda^2}{\Pi_{\max}}, & \text{Pe}_s &\equiv \frac{\langle h \rangle \Pi_{\max}}{\mu D_s} \\ \text{Pe}_b &\equiv \frac{\langle h \rangle \Pi_{\max}}{\mu D_b}, & \beta &\equiv \frac{k_1}{k_2 \langle h \rangle}, & K &\equiv k_2 t_M. \end{aligned} \quad (7.34)$$

The Bond number Bo quantifies the relative importance of hydrostatic and capillary pressure gradients, whereas the Peclet numbers Pe_s and Pe_b compare the effects of convective and diffusive surfactant transport at the liquid-air interface and in the bulk, respectively.

The initial conditions for the film thickness and surfactant surface concentration are the same as in the case of insoluble surfactants, Eqs. (7.6,7.7). We assumed that the height-averaged bulk concentration is initially uniform and in equilibrium with the surface concentration. Using the non-dimensional version of Eq. (7.27) we find $\hat{C}(\bar{x}, \hat{t} = 0) = \hat{\Gamma}_0 / (2 - \hat{\Gamma}_0)$.

7.3 Results and discussion

7.3.1 Leveling dynamics

During leveling, liquid locally flows from the elevated regions towards the regions of reduced film thickness, which leads to a converging flow in the valleys and surface expansion on the hills. Considering an initially uniform surfactant concentration distribution, this surface compression and expansion induces Marangoni stresses, which oppose flow driven by capillary and hydrostatic pressure gradients and thereby slow down the leveling dynamics.

We solved Eqs. (7.2-7.5) and (7.31-7.33) numerically with the finite element software Comsol Multiphysics 3.5 using quadratic basis functions. Figure 7.5 illustrates the relative increase of the leveling time $t_{\text{lev}}/t_{\text{lev}}(\bar{\Gamma}_0 = 0)$ when an insoluble surfactant is present at the air-liquid interface. The solid lines correspond to numerical solutions for different values of \bar{a}_0 . The crosses indicate the results of the perturbation analysis according to Eq. (7.16) for $\bar{a}_0 = 0.01$, which agrees very well with the corresponding numerical solution.

When $\bar{\Gamma}_0 = 0$, the leveling time ratio is unity by definition. For $\bar{\Gamma}_0 \gg 1$, i.e. in the saturation regime of the equation of state, a small change in the surfactant surface concentration has no effect on the surface tension. Consequently, $t_{\text{lev}}/t_{\text{lev}}(\bar{\Gamma}_0 = 0)$ becomes independent of $\bar{\Gamma}_0$ in the limit $\bar{\Gamma}_0 \gg 1$. The saturation value corresponds to capillary/hydrostatic leveling with the reduced surface tension γ_∞ . In the intermediate regime $0 < \bar{\Gamma}_0 \lesssim 1$, the influence of flow-induced surfactant concentration gradients substantially increases t_{lev} above $t_{\text{lev}}(\bar{\Gamma}_0 = 0)$. The addition of surfactants thus can significantly slow down the leveling dynamics by more than a factor of 8.

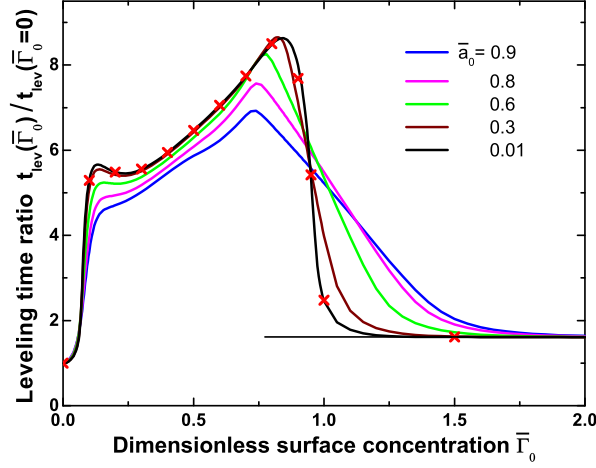


Figure 7.5: Leveling time ratio $t_{\text{lev}}(\bar{\Gamma}_0)/t_{\text{lev}}(\bar{\Gamma}_0 = 0)$ as a function of non-dimensional initial surfactant concentration $\bar{\Gamma}_0$ for different topographical amplitudes $a_0/\langle h \rangle$ ranging from 0.01 to 0.9 as listed in the legend. The following parameter values were assumed: $\text{Pe}_s = 1000$, $\epsilon^2 \text{Bo} = 0.004$, and $\epsilon = 0.1$. Crosses correspond to results of the perturbation analysis for the case $\bar{a}_0 = 0.01$.

Larger values of the ripple amplitude induce larger overall variations of the surfactant surface concentration $\Delta\bar{\Gamma} \equiv \max(\bar{\Gamma}) - \min(\bar{\Gamma})$. This tends to flatten the dependence of $t_{\text{lev}}/t_{\text{lev}}(\bar{\Gamma}_0 = 0)$, because a larger fraction of the concentration range relevant for the equation of state is involved in determining the dynamics. These larger variations are also the reason why the leveling time ratio increases with the ripple amplitude for $\bar{\Gamma}_0 \gtrsim 1$, although $\bar{\gamma}(\bar{\Gamma}_0)$ is already in the flat region of Fig. 7.4. We note that although the ratio $t_{\text{lev}}/t_{\text{lev}}(\bar{\Gamma}_0 = 0)$ primarily decreases for increasing ripple amplitudes above 0.5 in the region $\bar{\Gamma}_0 \lesssim 1$, the absolute leveling time t_{lev} typically *increases* due to a reduced mobility of the liquid film in the thin regions.

In order to illustrate the leveling dynamics we plotted the dimensionless ripple amplitude $\bar{h}(\bar{x} = 0, \bar{t}) - 1$ for $a_0/\langle h \rangle = 0.01$ and different initial surfactant concentrations $\bar{\Gamma}_0$ in Fig. 7.6(a). The straight, black solid line corresponds to purely capillary leveling, i.e. $\Gamma = 0$, for which the globally fastest leveling is observed. The remaining curves all exhibit two distinct time-scales corresponding to the rate constants N_{\pm} given in Eq. (7.18). The non-monotonic behavior visible in Fig. 7.5 is a consequence of the superposition of these two processes. The curve for $\bar{\Gamma}_0 = 0.3$ shows the fastest asymptotic decay rate N_- , since the equation of state (7.5) attains its maximum slope $\partial\gamma/\partial\bar{\Gamma}$ approximately at $\bar{\Gamma} \approx 0.3$ (see Fig. 7.4) and Q in Eq. (7.19), thus, its maximum value.

Figure 7.6(b) shows the variation of the surfactant surface concentration $\bar{\Gamma}(\bar{x} = 0, \bar{t}) - \bar{\Gamma}_0$ for $a_0/\langle h \rangle = 0.01$ and the same initial surfactant concentrations $\bar{\Gamma}_0$ as

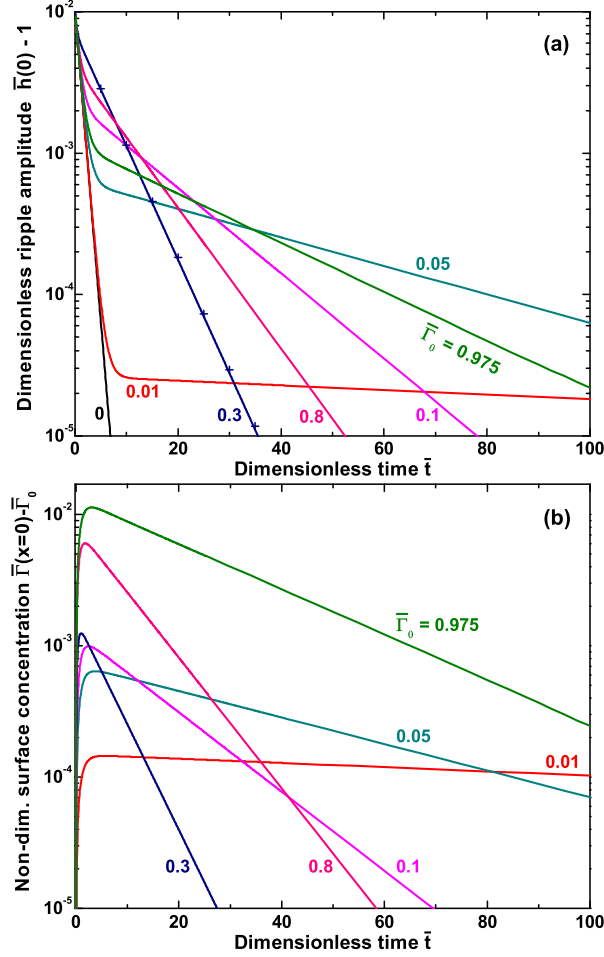


Figure 7.6: (a) Dimensionless ripple amplitude $\bar{h}(\bar{x}=0, \bar{t}) - 1$ for $\bar{a}_0 = 0.01$ and different initial surfactant concentrations $\bar{\Gamma}_0$. Crosses correspond to results of the perturbation analysis for the case $\bar{\Gamma}_0 = 0.3$. (b) Dimensionless surface concentration $\bar{\Gamma}(\bar{x} = 0, \bar{t}) - \bar{\Gamma}_0$ for $a_0/\langle h \rangle = 0.01$ and different initial surfactant concentrations $\bar{\Gamma}_0$. In both plots the parameters $\epsilon \equiv \lambda/\langle h \rangle$, $\epsilon^2 \text{Bo}$ and Pe_s were assumed to be 0.1, 0.004 and 1000, respectively.

plotted in Fig. 7.6(a). The maximum concentration variation appears to increase with increasing $\bar{\Gamma}_0$. According to Eqs. (7.16) and (7.17), the asymptotic slopes of the curves are identical with the corresponding ones in Fig. 7.6(a).

Figure 7.7(a,b) shows the relative increase of the leveling time when a soluble surfactant is present in the bulk liquid as well as at the liquid-air interface. A small value of the adsorption rate parameter K corresponds to a surfactant that is effectively insoluble on the timescale of the leveling process. As in the case of

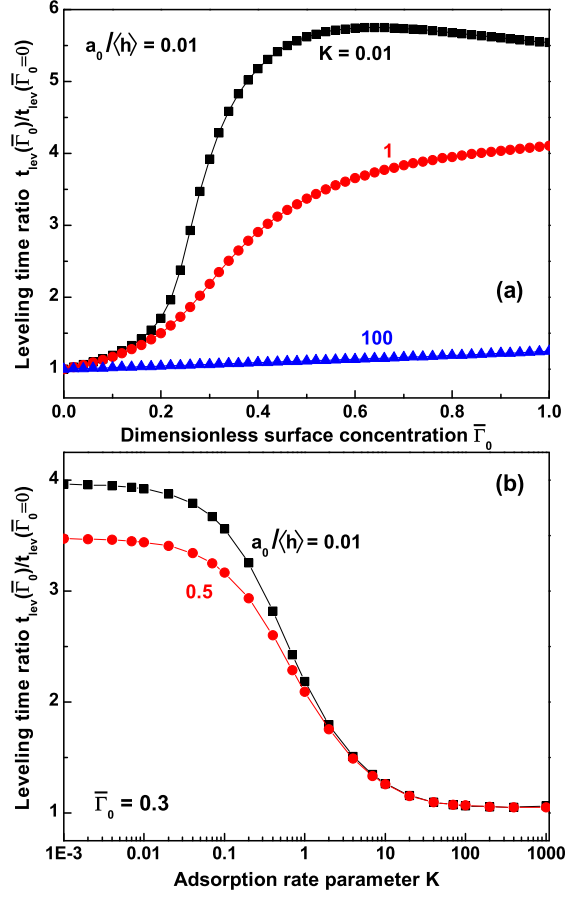


Figure 7.7: (a) Leveling time ratio $t_{lev}(\bar{\Gamma}_0)/t_{lev}(\bar{\Gamma}_0 = 0)$ as a function of non-dimensional surfactant concentration for $a_0/\langle h \rangle = 0.01$ and different values of the adsorption rate parameter K . (b) Leveling time ratio $t_{lev}(\bar{\Gamma}_0)/t_{lev}(\bar{\Gamma}_0 = 0)$ as a function of the adsorption rate parameter K for $\bar{\Gamma}_0 = 0.3$ and two values of $a_0/\langle h \rangle$. In both plots the following parameter values were assumed: $\epsilon = 0.1$, $\epsilon^2 Bo = 0.004$, $Pe_s = 1000$, $Pe_b = 100$ and $\beta = 0.059$.

insoluble surfactants a significantly longer leveling time results. A large value of K implies that on the timescale of the flow the surfactant is always in equilibrium with the underlying bulk liquid, which strongly reduces its influence on the leveling process. In addition for sufficiently thick films, the height-averaged bulk concentration does not change much as a consequence of adsorption or desorption and Marangoni-stresses are strongly diminished. In this case the capillary leveling dynamics are effectively recovered and the only effect of the surfactant is to reduce the overall surface tension. For an equation of state like SDS in glycerol, this

slows down leveling by a factor of up to about 1.5, but for other surfactant/solvent combinations by typically no more than a factor of 2-3.

Figure 7.7(b) also illustrates the effect of the ripple amplitude. As in the case of insoluble surfactants, a larger ripple amplitude tends to somewhat lessen the retarding effect for small values of $K \lesssim 1$ and provided Γ remains considerably below Γ_s . For large values of $K \gtrsim 1$, Marangoni stresses are diminished and any remaining influence of the surfactant on the leveling time ratio becomes independent of the ripple amplitude.

7.3.2 Redistribution time of inkjet printed multi-lines

So far we have considered the leveling dynamics in the interior of a line array. If a uniform thickness is desired then the overall redistribution time t_{red} constitutes an upper bound for the device fabrication process. In this section we discuss how t_{red} depends on the width of the multi-line w and the lateral linepitch d_l in the presence of insoluble surfactants.

For $\lambda < \ell_c$, the capillary leveling time scales as $t_{\text{lev}} \sim \lambda^4 / \langle h \rangle^3$ [Eq. (7.10)], where λ and $\langle h \rangle$ had been considered as independent parameters. For inkjet-printed structures, they are both, however, determined by the line pitch, $\lambda \sim d_l$ and $\langle h \rangle \sim 1/d_l$, such that we expect the leveling time to scale as $t_{\text{lev}} \sim d_l^7$. Provided that $w < \ell_c$, an equivalent scaling is expected for the multi-line redistribution time, if the wavelength λ is replaced by the width of the multi-line $w = (N - 1)d_l + w_{\text{sl}}$, leading to $t_{\text{red}} \sim w^4 d_l^3$. The exact definition of t_{red} that we have used is illustrated in Fig. 7.8(a), where we plotted the time-evolution of the center height of a multi-line array $\hat{h}(\bar{x}=0, \hat{t})$. Here, \hat{h} is defined as $\hat{h} \equiv h/h_{\text{sl}}$. For $\hat{t} > \hat{t}_{\text{lev}}$ and sufficiently large $N \gg 1$, $\hat{h}(0, \hat{t})$ reaches a first plateau value which we denote \hat{h}_{lev} . After completion of the redistribution, $\hat{h}(0, \hat{t})$ reaches a second plateau value denoted as \hat{h}_{red} . The redistribution time \hat{t}_{red} is defined as the instant when the center height reaches a value halfway between the two plateau values, $\hat{h}(0, \hat{t}_{\text{red}}) = \frac{1}{2}(\hat{h}_{\text{lev}} + \hat{h}_{\text{red}})$.

Numerical results obtained for initial conditions equivalent to Eqs. (7.1) and (7.7) are presented in Fig. 7.8(b,c) and reproduce the expected scalings very well, both with and without an insoluble surfactant being present. The (small) deviations from the expected scaling behavior for small d_l/w_{sl} and small N are attributed to end-effects.

7.3.3 Implications for printing process windows

The effect of initially uniform surfactant distributions is to delay leveling and redistribution by a factor of up to approximately 8. Due to the highly nonlinear dependence of the leveling time t_{lev} on the linepitch d_l , the most crucial parameter for the leveling process is d_l . The redistribution time for narrow linewidths $w < \ell_c$ scales as $t_{\text{red}} \sim w^4 \sim N^4$, i.e. the process window for achieving leveling while avoiding significant redistribution effects becomes wider for larger N . For wide

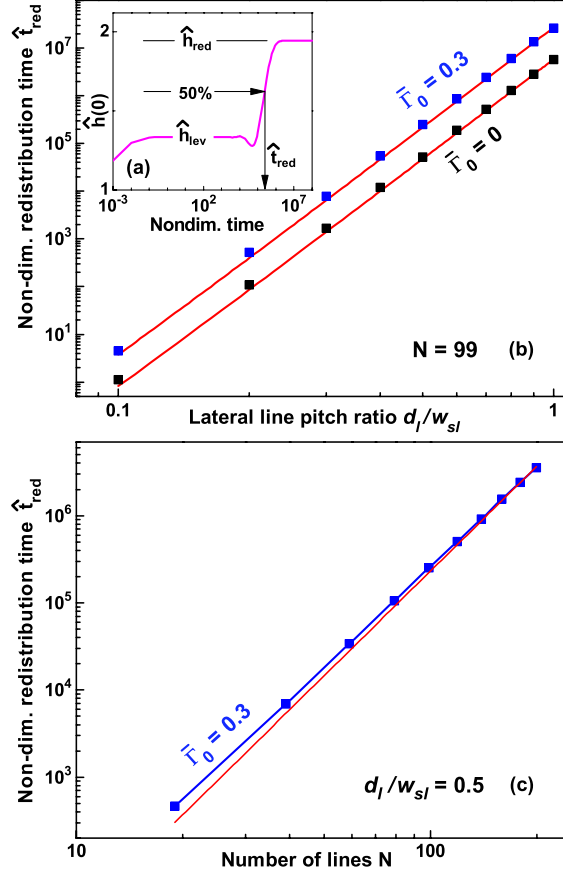


Figure 7.8: (a) Definition of the redistribution time \hat{t}_{red} . (b) Redistribution time \hat{t}_{red} as a function of d_l/w_{sl} for $N = 99$ and insoluble surfactant concentrations of $\bar{\Gamma}_0 = 0$ and 0.3. The symbols represent numerical data, the red straight lines powerlaw relations $\hat{t}_{\text{red}} = B_1 w^4 d_l^3$ with fitted coefficients B_1 . (c) Redistribution time $\hat{t}_{\text{red}}(\bar{\Gamma}_0 = 0.3)$ as a function of the number of inkjet-printed lines N for a surfactant concentration of $\bar{\Gamma}_0 = 0.3$ and $d_l = 50 \mu\text{m}$. The symbols represent numerical data, the red straight line a powerlaw relation $\hat{t}_{\text{red}} = B_2 ((N-1)d_l + w_{sl})^4$ with fitted coefficient B_2 . In all plots the following parameter values were used: $\widehat{\text{Pe}}_s \equiv h_{sl} \Pi_{\text{max}} / (\mu D_s) = 1000$, $\widehat{\text{Bo}} \equiv \rho g w_{sl}^2 / \Pi_{\text{max}} = 0.0041$, $\varepsilon = 0.1$, $h_{sl} = 10 \mu\text{m}$, and $w_{sl} = 100 \mu\text{m}$.

lines $w \gg \ell_c$, we expect a different scaling owing to Eq. (7.10), however, for typical parameter values t_{red} then becomes so large that this regime may not be of practical relevance.

Two obvious strategies for avoiding or minimizing surfactant related leveling delays is to either not add surfactants at all or to increase the surfactant concentration well beyond Γ_c , i.e. $\bar{\Gamma}_0 > 1$, since then the leveling time ratio $t_{\text{lev}}/t_{\text{lev}}(\bar{\Gamma}_0 = 0)$

plotted in Fig. 7.5 is both reduced and remains unaffected by small processing-related variations in $\bar{\Gamma}_0$. In the case of soluble surfactants, rapid adsorption and desorption rates effectively eliminate Marangoni-stress related effects for thick enough films, and the only retardation left is due to the reduced value of the surface tension, which amounts to typically no more than a factor of 2 or 3.

Whether these are viable solutions that are beneficial for the entire printing process, depends not only on the functionality of the coating, but also on the influence of the surfactant on e.g. solvent evaporation and the wettability of the solution on the substrate. For instance in the context of organic electronic devices, the device performance and efficiency may be adversely affected by a high surfactant concentration.

Our results have been obtained with two particular, yet typical and representative equations of state. In the case of soluble surfactants, we considered the regime where surface adsorption is kinetics-limited as described by a Langmuir equation [Eqs. (7.26, 7.27)], but not limited by diffusion in the bulk liquid, i.e. we implicitly assumed that vertical concentration equilibration occurs rapidly compared to the leveling time-scale, which is appropriate for thin films.

7.4 Summary

We have studied the leveling and redistribution dynamics of inkjet-printed multi-lines in the presence of soluble and insoluble surfactants. While insoluble surfactants can slow down the leveling process up to a factor of approximately 8, the retarding effect of soluble surfactants can be lower in the case of fast rates of surfactant bulk-surface exchange. Our results are representative of typical equation of state and in the case of soluble surfactants for the regime when surfactant adsorption is kinetics limited as described by a Langmuir equation. We presented numerical simulations as well as scaling relations for both the leveling and redistribution times of multi-lines as a function of the number of individual lines, the lateral pitch, the average line height and width, which provide a basis for estimating optimal process conditions.

Chapter 8

Conclusions and outlook

During the work with the present thesis we have conducted an extensive numerical study of surfactant spreading dynamics. We have investigated several types of material systems for surfactants spreading at liquid-air and liquid-liquid interfaces. We monitored the evolution of the liquid height profile after non-uniform surfactant deposition at the interface. The most prominent morphological feature of the spreading process is the formation of a local maximum in film thickness, called rim, and its propagation away from the deposition region. The rim dynamics can be well approximated by power-law $x_{\text{rim}} \sim t^\alpha$, where α is called spreading exponent.

We have studied the spreading dynamics of insoluble surfactants on thin liquid films with initially uniform height. Numerical simulations based on the lubrication approximation of the far-field axisymmetric spreading dynamics compare very favorably with the experimental results reported in the literature for oleic acid spreading on glycerol. The corresponding non-linear equation of state, which provides an excellent fit for the experimental dependence of surface tension on surfactant concentration, was shown to influence spreading rates considerably compared with a linear one. A fingering instability was observed, which is induced by the temporary entrapment of sub-phase liquid in the surfactant deposition area and its subsequent release. Acting as an excellent method of surfactant transport, the expulsion has a direct effect by increasing the spreading exponent. The model could be possibly improved by including the deformation of the surfactant droplet in the vicinity of the three-phase contact line.

A study of an insoluble surfactant spreading at curved liquid-air interfaces was also conducted. Using a numerical model based on the lubrication approximation, we monitored the evolution of the liquid height profile after deposition of an insoluble surfactant monolayer at rivulet-air interface. The spreading dynamics is well characterized by a power-law. Continuous, i.e. unlimited surfactant supply led to higher exponents and increased the influence of the rivulet aspect ratio as

compared to the case of limited supply. The results were compared with experimental findings for oleic acid spreading on glycerol rivulets defined by chemical surface patterning. The spreading exponents determined from the continuous-supply model and line source compare favorably with the experimental data. We found that the initial center-line film thickness has little effect on the spreading exponents. The lateral confinement induces non-uniform height- and surface velocity profiles, which manifest themselves in a pronounced transition of the evolving rivulet morphology.

We investigated the spreading of a soluble surfactant at curved liquid-air interfaces. Our numerical model was based on the lubrication approximation and the assumption of vertically uniform concentration profiles. A proper choice of initial and boundary conditions in the numerical models resulted in spreading exponents that are in excellent agreement with the experimental results for sodium dodecyl sulfate spreading on narrow glycerol rivulets. The influence of fingering instabilities, commonly observed during the spreading process, on the rim shape and propagation rate was studied. The rim height profiles deduced from experiments were in excellent agreement with numerical data at early times, but systematically lower at later stages. The origin of this discrepancy resides in vertical concentration non-uniformities, caused by surfactant slow diffusion, that are not accounted for in the lubrication model.

The spreading of soluble slow-diffusion surfactants at liquid-air interfaces was studied by employing two different numerical models. The first model is based on the full Navier-Stokes equation and convection-diffusion equations for bulk- and surface surfactant transport. It accounts for domain deformability and allows for vertically non-uniform concentration profiles. The second model is based on the lubrication approximation and the assumption of vertically *parabolic* concentration profiles. The two studied models gave considerably different results with respect to film thickness evolution for diffusion coefficients below a certain value. The difference originates in vertical concentration non-uniformities in the sub-phase liquid that are not accurately represented by parabolic profile in the lubrication model. The model based on the full Navier-Stokes equation would be a perfect candidate to compare with the experimental data for SDS spreading on rivulets, but computational costs of three-dimensional calculations at the moment are too high given the small aspect ratio of the systems. This model could also be used to model systems with discontinuous interfaces in order to extend the current work focused on continuous interfaces.

In addition, we studied the spreading of soluble surfactant at liquid-liquid interfaces between parallel solid plates. Two systems were considered: a flat interface with initially uniform height and narrow rivulets with initially curved interface. We developed two different numerical models. The first is based on the lubrication approximation and vertically uniform concentration profiles. The second model is based on the full Navier-Stokes equation and allows for vertically non-uniform concentration profiles. The novel model based on the Arbitrary Lagrangian Eule-

rian method allows us to simulate systems characterized by a very slow diffusion, i. e. large Peclet numbers, or large film thicknesses. We conclude that viscosity difference closer to 1 between the two liquids lowers the spreading rates and the rim height. Comparison of rivulet height profiles from experiments for a material system characterized by a very small viscosity ratio with the lubrication model data yielded similar conclusions as for spreading at liquid-air interfaces. Good quantitative agreement can be obtained with the lubrication model with combination of continuous surfactant supply at the interface and finite supply in the bulk.

We also investigated how soluble or insoluble surfactants affect the leveling dynamics of inkjet-printed lines. Surfactants cause surface tension gradients that oppose capillary leveling of ripples initially present at the surface. Insoluble surfactants can slow down the leveling process by up to a factor of eight. The retarding effect of soluble surfactants can be smaller in the case of fast rates of bulk-surface exchange. Our results were obtained for a non-linear equations of state and in the case of soluble surfactants for surfactant adsorption kinetics described by a Langmuir equation. We presented numerical results as well as scaling relations for both the leveling and redistribution times of multi-lines as a function of the number of individual lines, the lateral pitch, the average line height and width. This provides a basis for estimating optimal process conditions.

Appendix A. Derivation of lubrication equations for thin liquid films

Lubrication equation for height evolution

We consider a thin Newtonian liquid film with the initial film thickness distribution $h_0(x, y)$. Depending on the shape of surfactant deposition region and initial profile of the sub-phase liquid, two system of coordinates can be considered. In the case of rectilinear spreading, we adopt Cartesian system of coordinates (x, y, z) with the origin located at the solid-liquid interface in the center of the film, see Fig. 8.1. Surfactant is deposited in a region of length $2L$ and width $2W$. In the case of axisymmetric spreading, we assume that the surfactant is deposited as a drop of radius L and the liquid film is initially flat with $h = h_0$. We adopt cylindrical coordinates (r, θ, z) with the origin located at the solid-liquid interface on the symmetry axis of the surfactant droplet. The derivations presented in this chapter are only carried out for the rectilinear geometry, since the axisymmetric case can be easily deduced from it.

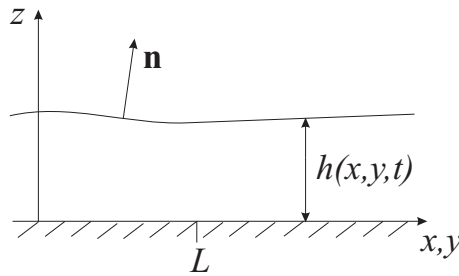


Figure 8.1: Schematic presentation of the geometry.

We introduce interface surface $z = h(x, y, t)$, with \mathbf{n} and \mathbf{t} being normal and

tangential vectors respectively. The normal vector is defined as

$$\mathbf{n} = \frac{1}{N} \left(-\frac{\partial h}{\partial x}, -\frac{\partial h}{\partial y}, 1 \right), \quad \text{where } N \equiv \sqrt{1 + \left(\frac{\partial h}{\partial x} \right)^2 + \left(\frac{\partial h}{\partial y} \right)^2} \quad (8.1)$$

The dynamics of the liquid film is described by the Navier-Stokes equation

$$\rho \left(\frac{\partial \mathbf{u}}{\partial t} + \mathbf{u} \nabla \mathbf{u} \right) = -\nabla p + \mu \nabla^2 \mathbf{u} \quad (8.2)$$

and continuity equation for incompressible liquid

$$\nabla \cdot \mathbf{u} = 0 \quad (8.3)$$

where $\mathbf{u} = (u_x, u_y, u_z)$ is the fluid velocity, p is the pressure, and ρ and μ are the fluid density and viscosity.

We use the following scaled variables

$$\begin{aligned} \bar{x} &\equiv \frac{x}{L}, & \bar{y} &\equiv \frac{y}{L}, & \bar{z} &\equiv \frac{y}{H}, & \bar{u}_x &\equiv \frac{u_x}{U_0}, & \bar{u}_y &\equiv \frac{u_y}{U_0}, \\ & & & & & & \bar{u}_z &\equiv \frac{u_z}{W_0}, & \bar{t} &\equiv \frac{U_0 t}{L}, & \bar{p} &\equiv \frac{H^2 p}{\mu U_0 L} \end{aligned} \quad (8.4)$$

In this chapter we consider systems with thin liquid films, for which the aspect ratio $\varepsilon = \frac{H}{L} \ll 1$ is small.

After introducing the scaled variables, the continuity equation becomes

$$0 = \nabla \cdot \mathbf{u} = \frac{U_0}{L} \frac{\partial \bar{u}_x}{\partial \bar{x}} + \frac{U_0}{L} \frac{\partial \bar{u}_y}{\partial \bar{y}} + \frac{W_0}{H} \frac{\partial \bar{u}_z}{\partial \bar{z}} \Rightarrow \frac{\partial \bar{u}_x}{\partial \bar{x}} + \frac{\partial \bar{u}_y}{\partial \bar{y}} + \frac{W_0 L}{U_0 H} \frac{\partial \bar{u}_z}{\partial \bar{z}} = 0 \quad (8.5)$$

Assuming that all the terms in the continuity equation are of the same order, yields the scale for the z -component of fluid velocity $W_0 = \varepsilon U_0$.

The scaled x -component of Navier-Stokes equation is

$$\begin{aligned} \rho \left(\frac{U_0^2}{L} \frac{\partial \bar{u}_x}{\partial \bar{t}} + \frac{U_0^2}{L} \bar{u}_x \frac{\partial \bar{u}_x}{\partial \bar{x}} + \frac{U_0^2}{L} \bar{u}_y \frac{\partial \bar{u}_x}{\partial \bar{y}} + \frac{\varepsilon U_0^2}{H} \bar{u}_z \frac{\partial \bar{u}_x}{\partial \bar{z}} \right) = \\ - \frac{\mu U_0 L}{H^2 L} \frac{\partial \bar{p}}{\partial \bar{x}} + \mu \left(\frac{U_0}{L^2} \frac{\partial^2 \bar{u}_x}{\partial \bar{x}^2} + \frac{U_0}{L^2} \frac{\partial^2 \bar{u}_x}{\partial \bar{y}^2} + \frac{U_0}{H^2} \frac{\partial^2 \bar{u}_x}{\partial \bar{z}^2} \right) \end{aligned} \quad (8.6)$$

$$\begin{aligned} \frac{\rho U_0 H}{\mu} \frac{H}{L} \left(\frac{\partial \bar{u}_x}{\partial \bar{t}} + \bar{u}_x \frac{\partial \bar{u}_x}{\partial \bar{x}} + \bar{u}_y \frac{\partial \bar{u}_x}{\partial \bar{y}} + \bar{u}_z \frac{\partial \bar{u}_x}{\partial \bar{z}} \right) = \\ - \frac{\partial \bar{p}}{\partial \bar{x}} + \frac{\partial^2 \bar{u}_x}{\partial \bar{z}^2} + \varepsilon^2 \left(\frac{\partial^2 \bar{u}_x}{\partial \bar{x}^2} + \frac{\partial^2 \bar{u}_x}{\partial \bar{y}^2} \right) \end{aligned} \quad (8.7)$$

Typical parameters values for our system are: $H \approx 10^{-5}$ m, $\rho \approx 1000$ kg/m³, $U_0 \approx 10^{-4}$ m/s for $\mu \approx 1$ Pa s, which yields the typical value of the Reynolds

number $Re = \frac{\rho U_0 H}{\mu} \sim 10^{-6}$. Thus, assuming $Re\varepsilon \ll 1$ and $\varepsilon^2 \ll 1$, we derive to first order in ε

$$-\frac{\partial \bar{p}}{\partial \bar{x}} + \frac{\partial^2 \bar{u}_x}{\partial \bar{z}^2} = 0 \quad (8.8)$$

In a similar way we derive the other components of the Navier-Stokes equation. The dimensional version of the resulting equations is then to the first order in ε

$$-\frac{\partial p}{\partial x} + \mu \frac{\partial^2 u_x}{\partial z^2} = 0 \quad (8.9)$$

$$-\frac{\partial p}{\partial y} + \mu \frac{\partial^2 u_y}{\partial z^2} = 0 \quad (8.10)$$

$$-\frac{\partial p}{\partial z} = 0 \quad (8.11)$$

Equation (8.11) shows that the pressure $p = p(x, y)$ is independent of z -coordinate. We have the no-slip conditions at the solid-liquid interface $u_x(z=0) = u_y(z=0) = 0$. The following conditions can be specified at the interface $z = h(x, y, t)$

$$p - p_a + \underline{\tau}_{nn_a} - \underline{\tau}_{nn} + 2\mathcal{H}\gamma = 0 \quad (8.12)$$

$$\underline{\tau}_{nt_a} - \underline{\tau}_{nt} + \mathbf{t} \cdot \nabla_s \gamma = 0 \quad (8.13)$$

where $\underline{\tau}$ is the viscous stress tensor, γ is the surface tension and $2\mathcal{H} = \nabla_s \cdot \mathbf{n}$ is twice the mean curvature. Assuming that the viscous normal stresses are negligible at a liquid-air interface yields $p - p_a = -\gamma \nabla_s \cdot \mathbf{n}$. The surface gradient operator ∇_s can be applied to any function defined at the surface $z = h(x, y)$ and is defined as

$$\nabla_s = (\mathbb{I} - \mathbf{nn})\nabla = \quad (8.14)$$

$$\frac{1}{N^2} \left(\begin{array}{c} \left[1 + \left(\frac{\partial h}{\partial y} \right)^2 \right] \frac{\partial}{\partial x} - \frac{\partial h}{\partial x} \frac{\partial h}{\partial y} \frac{\partial}{\partial y} \\ - \frac{\partial h}{\partial x} \frac{\partial h}{\partial y} \frac{\partial}{\partial x} + \left[1 + \left(\frac{\partial h}{\partial x} \right)^2 \right] \frac{\partial}{\partial y} \\ \frac{\partial h}{\partial x} \frac{\partial}{\partial x} + \frac{\partial h}{\partial y} \frac{\partial}{\partial y} \end{array} \right) \quad (8.15)$$

The mean curvature follows as

$$\nabla_s \cdot \mathbf{n} = \frac{\left[1 + \left(\frac{\partial h}{\partial y} \right)^2 \right] \frac{\partial^2 h}{\partial x^2} + \left[1 + \left(\frac{\partial h}{\partial x} \right)^2 \right] \frac{\partial^2 h}{\partial y^2} - 2 \frac{\partial h}{\partial x} \frac{\partial h}{\partial y} \frac{\partial^2 h}{\partial x \partial y}}{\left(1 + \left(\frac{\partial h}{\partial x} \right)^2 + \left(\frac{\partial h}{\partial y} \right)^2 \right)^{3/2}} \quad (8.16)$$

After using the scaling (8.4) and neglecting terms of order ε , we obtain $\nabla_s \cdot \mathbf{n} = \frac{\partial^2 h}{\partial x^2} + \frac{\partial^2 h}{\partial y^2}$. Thus, the equation for capillary pressure p becomes

$$p = -\gamma \left(\frac{\partial^2 h}{\partial x^2} + \frac{\partial^2 h}{\partial y^2} \right) \quad (8.17)$$

Neglecting viscous stresses in the gas phase, the remaining surface conditions from (8.13) result in

$$\mu \frac{\partial u_x}{\partial z}(z=h) = \frac{\partial \gamma}{\partial x} \quad (8.18)$$

$$\mu \frac{\partial u_y}{\partial z}(z=h) = \frac{\partial \gamma}{\partial y} \quad (8.19)$$

The liquid-air interface is defined by the scalar function $f(x, y, z, t) = z - h(x, y, t) = 0$. For non-volatile liquid the surface is a material surface and thus the following holds

$$\frac{Df}{Dt} = \frac{\partial f}{\partial t} + \mathbf{u} \cdot \nabla f = 0 \quad (8.20)$$

or equivalently

$$-\frac{\partial h}{\partial t} - \frac{\partial h}{\partial x} u_x|_{z=h(x,y,t)} - \frac{\partial h}{\partial y} u_y|_{z=h(x,y,t)} + u_z|_{z=h(x,y,t)} = 0 \quad (8.21)$$

We integrate the continuity equation Eq. (8.5) with respect to z from 0 to h

$$\int_0^h \left(\frac{\partial u_x}{\partial x} + \frac{\partial u_y}{\partial y} \right) dz + u_z|_{z=h} - u_z|_{z=0} = 0 \quad (8.22)$$

Using Leibnitz rule for integration and considering that $u_z(z=0) = 0$ as a consequence of no-penetration condition, we arrive at

$$-u_z|_{z=h(x,y,t)} = \frac{\partial}{\partial x} \int_0^h u_x dz - \frac{\partial h}{\partial x} u_x|_{z=h} + \frac{\partial}{\partial y} \int_0^h u_y dz - \frac{\partial h}{\partial y} u_y|_{z=h} \quad (8.23)$$

Using this equality, we transform equation (8.21) into

$$\frac{\partial h}{\partial t} + \frac{\partial}{\partial x} \int_0^h u_x dz + \frac{\partial}{\partial y} \int_0^h u_y dz = 0 \quad (8.24)$$

We integrate Navier-Stokes equation using the above specified boundary conditions Eqs. (8.18,8.18) taking into account that p and consequently $\frac{\partial p}{\partial x}$ and $\frac{\partial p}{\partial y}$ do not depend on z . The resulting velocities are

$$u_x(x, y, z) = \frac{1}{\mu} \frac{\partial p}{\partial x} \left(\frac{z^2}{2} - hz \right) + \frac{1}{\mu} \frac{\partial \gamma}{\partial x} z \quad (8.25)$$

$$u_y(x, y, z) = \frac{1}{\mu} \frac{\partial p}{\partial y} \left(\frac{z^2}{2} - hz \right) + \frac{1}{\mu} \frac{\partial \gamma}{\partial y} z \quad (8.26)$$

We then substitute integrated velocities into Eq. (8.24) and obtain an equation for the height evolution, which is known as the lubrication equation,

$$\frac{\partial h}{\partial t} + \nabla \left[\frac{1}{2\mu} (h^2 \nabla \gamma) - \frac{1}{3\mu} h^3 \nabla p \right] = 0 \quad (8.27)$$

$$p = -\gamma \nabla^2 h + \rho g h \quad (8.28)$$

where $\nabla \equiv \left(\frac{\partial}{\partial x}, \frac{\partial}{\partial y} \right)$ for rectilinear spreading. The derivations presented in this section were extensively reviewed in [38].

Convection-diffusion equation at the interface

The surfactant transport at the interface $z = h(x, y, t)$ is governed by the surface convection and diffusion equation [70, 71, 72, 69].

$$\frac{\partial \Gamma}{\partial t} + \nabla_s \cdot (\Gamma \mathbf{u}|_{z=h(x,y)}) = J + D_s \nabla_s^2 \Gamma \quad (8.29)$$

where Γ is the interface concentration, D_s is the surface diffusion coefficient and J is describing flux term between the interface and the bulk. In the case of an insoluble surfactant the flux J is zero. Using expression defined in (8.15) for the surface gradient operator and neglecting terms of order ε^2 , the second term on the left-hand side becomes

$$\nabla_s \cdot (\mathbf{u}\Gamma) = \frac{\partial}{\partial x} (\Gamma u_x(x, y, z = h)) + \frac{\partial}{\partial y} (\Gamma u_y(x, y, z = h)) \quad (8.30)$$

Taking into account velocities (8.25) evaluated at the surface

$$u_x(x, y, z = h) = \frac{1}{\mu} \frac{\partial p}{\partial x} \left(-\frac{h^2}{2} \right) + \frac{1}{\mu} \frac{\partial \gamma}{\partial x} h \quad (8.31)$$

$$u_y(x, y, z = h) = \frac{1}{\mu} \frac{\partial p}{\partial y} \left(-\frac{h^2}{2} \right) + \frac{1}{\mu} \frac{\partial \gamma}{\partial y} h \quad (8.32)$$

we obtain convection-diffusion equation at the interface $z = h(x, y, t)$

$$\frac{\partial \Gamma}{\partial t} + \nabla \left[\frac{1}{\mu} h \Gamma \nabla \gamma - \frac{1}{2\mu} h^2 \Gamma \nabla p - D_s \nabla \Gamma \right] = J \quad (8.33)$$

where two-dimensional gradient is $\nabla \equiv \left(\frac{\partial}{\partial x}, \frac{\partial}{\partial y} \right)$.

Bibliography

- [1] P. M. Schweizer and S. F. Kistler, *Liquid Film Coating*, Chapman & Hall, London, 1997.
- [2] J. B. Grotberg, *Pulmonary flow and transport phenomena*, *Annu. Rev. Fluid Mech.*, 1994, **26**, 529-571.
- [3] L. W. Lake, *Enhanced oil recovery*, Prentice-Hall, New Jersey, 1989.
- [4] D. O. Shan and R. S. Schechter, *Improved oil recovery by surfactant and polymer flooding*, Academic Press Inc., New York, 1977.
- [5] L. L. Schramm, *Surfactants: fundamentals and applications in the petroleum industry*, Cambridge University Press, Cambridge, 2000.
- [6] V. G. Levich, *Physicochemical Hydrodynamics*, Prentice-Hall, Englewood Cliffs, 1962.
- [7] C. S. Yih, *Fluid motion induced by surface tension variation*, *Phys. Fluids*, 1968, **11**, 477-480.
- [8] J. Adler and L. Sowerby, *Shallow three-dimensional flows with variable surface tension*, *J. Fluid Mech.*, 1970, **42**, 549-560.
- [9] J. Ahmad and R. S. Hansen, *A simple quantitative treatment of the spreading of monolayers on thin liquid films*, *J. Colloid Interface Sci.*, 1972, **38**, 601-604.
- [10] M. S. Borgas and J. B. Grotberg, *Monolayer flow on a thin film*, *J. Fluid Mech.*, 1988, **193**, 151-170.
- [11] S. M. Troian, X. L. Wu and S. A. Safran, *Fingering instability in thin wetting films*, *Phys. Rev. Lett.*, 1989, **62**, 1496-1499.
- [12] S. M. Troian, E. Herbolzheimer and S. A. Safran, *Model for the Fingering Instability of Spreading Surfactant Drops*, *Phys. Rev. Lett.*, 1990, **62**, 333-336.
- [13] D. P. Gaver and J. B. Grotberg, *The dynamics of a localized surfactant on a thin film*, *J. Fluid Mech.*, 1990, **213**, 127-148.
- [14] D. P. Gaver and J. B. Grotberg, *Droplet spreading on a thin viscous film*, *J. Fluid Mech.*, 1992, **235**, 399-414.
- [15] O. E. Jensen and J. B. Grotberg, *Insoluble surfactant spreading on a thin viscous film: shock evolution and film rupture*, *J. Fluid Mech.*, 1992, **240**,

- 259-288.
- [16] O. E. Jensen and J. B. Grotberg, *The spreading of heat or soluble surfactant along a thin liquid film*, Phys. Fluids A, 1993, **5**, 58-68.
 - [17] O. E. Jensen, *Self-similar, surfactant-driven flows*, Phys. Fluids, 1994, **6**, 1084-1094.
 - [18] V. M. Starov, A. de Ryck and M. G. Velarde, *On the spreading of an insoluble surfactant over a thin viscous liquid layer*, J. Colloid Interface Sci., 1997, **190**, 104-113.
 - [19] O. K. Matar and S. M. Troian, *Growth of nonmodal transient structures during the spreading of surfactant coated films*, Phys. Fluids, 1998, **10**, 1234-1236.
 - [20] O. K. Matar and S. M. Troian, *The development of transient fingering patterns during the spreading of surfactant coated films*, Phys. Fluids, 1999, **11**, 3232-3246.
 - [21] J. L. Bull, L. K. Nelson, J. T. Walsh, Jr., M. R. Glucksberg, S. Schürch and J. B. Grotberg, *Surfactant spreading and surface compression disturbance on a thin viscous film*, J. Biomed. Eng., 1999, **121**, 89-98.
 - [22] P. L. Evans, L. W. Schwartz and R. V. Roy, *A mathematical model for crater defect formation in a drying paint layer*, J. Colloid Interface Sci., 2000, **227**, 191-205.
 - [23] B. J. Fischer and S. M. Troian, *Growth and decay of localized disturbances on a surfactant coated spreading film*, Phys. Rev. E, 2003, **67**, 016309.
 - [24] B. J. Fischer and S. M. Troian, *Thinning and disturbance growth in liquid films mobilized by continuous surfactant delivery*, Phys. Fluids, 2003, **15**, 3837-3845.
 - [25] M. R. E. Warner, R. V. Craster and O. K. Matar, *Fingering phenomena associated with insoluble surfactant spreading on thin liquid films*, J. Fluid Mech., 2004, **510**, 169-200.
 - [26] O. E. Jensen and S. Naire, *The spreading and stability of a surfactant-laden drop on a prewetted substrate*, J. Fluid Mech., 2006, **554**, 5-24.
 - [27] O. K. Matar and R.V. Craster, *Dynamics of surfactant-assisted spreading*, Soft Matter, 2009, **5**, 3801-3809.
 - [28] A. D. Dussaud, O. K. Matar and S. M. Troian, *Spreading characteristics of an insoluble surfactant film on a thin liquid layer: comparison between theory and experiment*, J. Fluid Mech., 2005, **544**, 23-51.
 - [29] B. Frank and S. Garoff, *Origins of complex motion of advancing surfactant solutions*, Langmuir, 1995, **11**, 87-93.
 - [30] S. He and J. B. Ketterson, *Surfactant-driven spreading of a liquid on a vertical surface*, Phys. Fluids, 1995, **7**, 2640-2647.
 - [31] M. Cachile and A. M. Cazabat, *Spontaneous spreading of surfactant solutions on hydrophilic surfaces: CnEm in ethylene and diethylene glycol*, Langmuir, 1999, **15**, 1515-1521.

- [32] M. Cachile, M. Schneemilch, A. Hamraoui and A.M. Cazabat, *Films driven by surface tension gradients*, Adv. Colloid Interface Sci., 2002, **96**, 59-74.
- [33] A. B. Afsar-Siddiqui, P. F. Luckham and O. K. Matar, *Unstable spreading of aqueous anionic surfactant solutions on liquid films. Part 1. Sparingly soluble surfactant*, Langmuir, 2003, **19**, 696-702.
- [34] A. B. Afsar-Siddiqui, P. F. Luckham and O. K. Matar, *Unstable spreading of aqueous anionic surfactant solutions on liquid films. Part 2. Highly soluble surfactant*, Langmuir, 2003, **19**, 703-708.
- [35] A. B. Afsar-Siddiqui, P. F. Luckham and O. K. Matar, *The spreading of surfactant solutions on thin liquid films*, Adv. Colloid Interface Sci., 2003, **106**, 183-236.
- [36] R. V. Craster and O. K. Matar, *Numerical simulations of fingering instabilities in surfactant-driven thin films*, Phys. Fluids, 2006, **18**, 032103.
- [37] B. D. Edmonstone, R. V. Craster and O. K. Matar, *Surfactant-induced fingering phenomena beyond the critical micelle concentration*, J. Fluid Mech., 2006, **564**, 105138.
- [38] A. Oron, S. H. Davis and S. G. Bankoff, *Long-scale evolution of thin liquid films*, Rev. Mod. Phys., 1997, **69**, 931-980.
- [39] R. V. Craster and O. K. Matar, *Dynamics and stability of thin liquid films*, Rev. Mod. Phys., 2009, **81**, 1131-1198.
- [40] B. J. Fischer, *Non-modal linear stability analysis of thin film spreading by Marangoni stresses*, PhD thesis, Princeton University, 2003.
- [41] A.-M. Cazabat, F. Heslot, S. M. Troian and P. Carles, *Fingering instability of thin spreading films driven by temperature gradients*, Nature (London), 1990, **346**, 824-826.
- [42] D. E. Kataoka and S. M. Troian, *A theoretical study of instabilities at the advancing front of thermally driven coating films*, J. Colloid Interface Sci., 1997, **192**, 350-362.
- [43] D. K. N. Sinz, M. Hanyak and A. A. Darhuber, *Immiscible surfactant droplets on thin liquid films: Spreading dynamics, subphase expulsion and oscillatory instabilities*, J. Colloid Interface Sci., 2011, **364**, 519-529.
- [44] S. E. Orchard, *On surface levelling in viscous liquids and gels*, Appl. Sci. Res., 1962, **11**, 451-464.
- [45] J. A. Fay and D. P. Hoult (ed.), *In oil on the sea*, Plenum, New York, 1969.
- [46] D. P. Hoult, *Oil spreading on the sea*, Annu. Rev. Fluid Mech., 1972, **4**, 341-368.
- [47] C. Huh, M. Inoue and S. Mason, *Uni-directional spreading of one liquid on the surface of another*, Can. J. Chem. Eng., 1975, **53**, 367-371.
- [48] M. Foda and R. G. Cox, *The spreading of thin liquid films on a water-air interface*, J. Fluid Mech., 1980, **101**, 33-51.
- [49] D. W. Camp and J. C. Berg, *The spreading of oil on water in the surface-tension regime*, J. Fluid Mech., 1987, **184**, 445-462.

-
- [50] Z. Dagan, *Spreading of films of adsorption on a liquid surface*, Physico Chem. Hydrodyn., 1984, **5**, 43-51.
- [51] O. E. Jensen, *The spreading of insoluble surfactant at the free surface of a deep fluid layer*, J. Fluid Mech., 1995, **293**, 349-378.
- [52] P. Joos and J. v. Hunsel, *Spreading of aqueous surfactant solutions on organic liquids*, J. Colloid Interface Sci., 1985, **106**, 161-167.
- [53] T. F. Svitova, R. M. Hill and C. J. Radke, *Spreading of aqueous dimethyldidodecylammonium bromide surfactant droplets over liquid hydrocarbon substrates*, Langmuir, 1999, **15**, 7392-7402.
- [54] S. Berg, *Marangoni-driven spreading along liquid-liquid interfaces*, Phys. Fluids, 2009, **21**, 032105.
- [55] R. V. Craster and O. K. Matar, *On autophobing in surfactant-driven thin films*, Langmuir, 2007, **23**, 2588-2601.
- [56] A. Borhan, H. Haj-Hariri and A. Nadim, *Effect of surfactants on the thermocapillary migration of a concentric compound drop*, J. Colloid Interface Sci., 1992, **149**, 553-560.
- [57] J. Chen and K. J. Stebe, *Surfactant-induced retardation of the thermocapillary migration of a droplet*, J. Fluid Mech., 1997, **340**, 35-59.
- [58] Y. S. Chen, Y. L. Lu, Y. M. Yang and J. R. Maa, *Surfactant effects on the motion of a droplet in thermocapillary migration*, Int. J. Multiphase Flow, 1997, **23**, 325-335.
- [59] B.D. Edmonstone and O.K. Matar, *Simultaneous thermal and surfactant-induced Marangoni effects in thin liquid films*, J. Colloid Interface Sci., 2004, **274**, 183-199.
- [60] R. Hanumanthu and K. J. Stebe, *Transient enhancement of thermocapillary flow in a two-dimensional cavity by a surfactant*, Phys. Fluids, 2007, **19**, 042103.
- [61] S. H. Davis, A. Liu and G. R. Sealy, *Motion driven by surface-tension gradients in a tube lining*, J. Fluid Mech., 1974, **62**, 737-751.
- [62] F. F. Espinosa, A. H. Shapiro, J. J. Fredberg and R. D. Kamm, *Spreading of exogenous surfactant in an airway*, J. Appl. Physiol., 1993, **75**, 2028-2039.
- [63] H. A. R. Williams and O. E. Jensen, *Surfactant transport over airway liquid lining of nonuniform depth*, J. Biomech. Eng., 2000, **122**, 159-166.
- [64] W. T. Tsai and L. Y. Liu, *Transport of exogenous surfactants on a thin viscous film within an axisymmetric airway*, Colloid Surf. A: Physicochem. Eng. Aspects, 2004, **234**, 51-62.
- [65] D. Follows, F. Tiberg, R.K. Thomas and M. Larsson, *Multilayers at the surface of solutions of exogenous lung surfactant: Direct observation by neutron reflection*, Biochim. Biophys. Acta, 2007, **1768**, 228-235.
- [66] J. B. Segur and H. E. Oberstar, *Viscosity of glycerol and its aqueous solutions*, Ind. Eng. Chem., 1951, **43**, 2117-2120.
- [67] D. K. N. Sinz, M. Hanyak, J. Zeegers and A. A. Darhuber, *Insoluble surfac-*

- tant spreading along thin liquid films confined by chemical surface patterns*, Phys. Chem. Chem. Phys., 2011, **13**, 9768-9777.
- [68] A. A. Darhuber, J. Z. Chen, J. M. Davis and S. M. Troian, *A Study of Mixing in Thermocapillary Flows on Micropatterned Surfaces*, in Transport and Mixing at the Microscale, J. M. Ottino and S. Wiggins, Eds., Phil. Trans. Royal Soc. London A, 2004, **362**, 1037-1058.
- [69] H. A. Stone, *On surface levelling in viscous liquids and gels*, Phys. Fluids A., 1990, **2**, 111.
- [70] L. E. Scriven, *Dynamics of a fluid interface; Equation of motion for Newtonian surface fluids*, Chem. Eng. Sci., 1960, **12**, 98-108.
- [71] R. Aris, *Vectors, tensors, and the basic equations of fluid dynamics*, Prentice-Hall, Englewood Cliffs, NJ, 1962.
- [72] A. M. Waxman, *Dynamics of a couple-stress fluid membrane*, Stud. Appl. Math., 1984, **70**, 63-86.
- [73] D. Halpern and J. B. Grotberg, *Fluid-elastic instabilities of liquid-lined flexible tubes*, J. Fluids Mech, 1992, **237**, 1-11.
- [74] O. K. Matar, *Nonlinear evolution of thin free viscous films in the presence of soluble surfactant*, Phys. Fluids, 2002, **14**, 4216-4234.
- [75] C. Lin, C. Hwang, G. Huang and W. Uen, *Nonlinear spreading dynamics of a localized soluble surfactant on a thin liquid film*, J. Phys. Soc. of Japan, 2002, **71**, 2708-2714.
- [76] M. R. E. Warner, R. V. Craster and O. K. Matar, *Fingering phenomena created by a soluble surfactant deposition on a thin liquid film*, Phys. Fluids A, 2004, **16**, 2933-2951.
- [77] J. W. Barret, R. Nürnberg, and M. R. E. Warner, *Finite element approximation of soluble surfactant spreading on a thin film*, Siam J. Numer. Anal., 2006, **44**, 1218-1247.
- [78] K.S. Lee and V.M. Starov, *Spreading of surfactant solutions over thin aqueous layers: Influence of solubility and micelles disintegration*, J. Colloid Interface Sci., 2007, **314**, 631-642.
- [79] K.S. Lee and V.M. Starov, *Spreading of surfactant solutions over thin aqueous layers at low concentrations: Influence of solubility*, J. Colloid Interface Sci., 2009, **329**, 361-365.
- [80] K. Piroird, C. Clanetab and D. Qur, *Detergency in a tube*, Soft Matter, 2011, **7**, 7498-7503.
- [81] A. A. Newman and L. V. Cocks, *Glycerol*, CRC Press, 1968.
- [82] D. Lide (ed.), *CRC Handbook of Chemistry and Physics*, D-240, 1982.
- [83] R. M. Weinheimer, D. F. Evans and E. L. Cussler, *Diffusion in surfactant solutions*, J. Colloid Interface Sci., 1981, **80**, 357-368.
- [84] N. V. Churaev, B. V. Derjaguin, and V. M. Muller, *Surface forces*, Kluwer Academic, 1987.
- [85] L. W. Schwartz, R. R. Eley, *Simulation of droplet motion on low-energy and*

- heterogeneous surfaces*, J. Colloid Interface Sci., 1998, **202**, 173-188.
- [86] M. Hanyak, D. K. N. Sinz, and A. A. Darhuber, *Soluble surfactant spreading on spatially confined thin liquid films*, Soft Matter, 2012, **8**, 7660-7671.
- [87] D. Merkt, A. Pototsky and M. Bestehorn, *Long-wave theory of bounded two-layer films with a free liquid-liquid interface: Short- and long-time evolution*, Phys. of Fluids, 2005, **17**, 064104.
- [88] M. Heller, *Theory and design of polymer-based microfluidic systems*, PhD thesis, Technical University of Denmark, 2008.
- [89] R. G. M. van der Sman and S. van der Graaf, *Diffuse interface model of surfactant adsorption onto flat and droplet interfaces*, Rheol Acta, 2006, **46**, 3-11.
- [90] K. E. Teigen, P. Song, J. Lowengrub, and A. Voigt, *A diffuse-interface method for two-phase flows with soluble surfactants*, J. Comput. Phys., 2011, **230**, 375-393.
- [91] M. R. Booty and M. Siegel, *A hybrid numerical method for interfacial fluid flow with soluble surfactant*, J. Comput. Phys., 2010, **229**, 3864-3883.
- [92] P. H. Saksono and D. Perić, *On finite element modelling of surface tension: Variational formulation and applications - Part 1: Quasistatic problems*, Comput. Mech., 2006, **38**, 265-281.
- [93] N. D. P. Smith, S. E. Orchard, and A. J. Rhind-Tutt, *The physics of brush-marks*, J. Oil Colour Chemists Assoc., 1961, **44**, 618-633.
- [94] T. C. Patton, *Paint flow and pigment dispersion*, Interscience Publishers, New York, 1964.
- [95] T. C. Woo, *Wave decay on glass surfaces at high temperatures*, J. Appl. Phys., 1969, **40**, 3140-3143.
- [96] J. F. Rhodes and B. W. King Jr., *Leveling of vitreous surfaces*, J. Am. Ceram. Soc., 1970, **53**, 134-135.
- [97] H. Vanoene, *Rheology of sintering, spreading and leveling of fluids*, J. Adhes., 1972, **4**, 247-259.
- [98] A. Quach, *Polymer Coatings. Physics and Mechanics of Leveling*, Ind. Eng. Chem. Prod. Res. Develop., 1973, **12**, 110-116.
- [99] D. Degani and C. Gutfinger, *Leveling of a Newtonian fluid on a horizontal surface*, Israel J. Technol., 1974, **12**, 191-197.
- [100] D. Degani and C. Gutfinger, *A numerical solution of the leveling problem*, Comput. Fluids, 1976, **4**, 149-155.
- [101] W. S. Overdiep, in *Physicochemical Hydrodynamics Vol. II*, ed. by D. B. Spalding, Advance Publ. Ltd., London, 1977.
- [102] W. S. Overdiep, *The leveling of paints*, Progr. Org. Coatings, 1986, **14**, 159-175.
- [103] R. Keunings and D. W. Bousfield, *Analysis of surface tension driven leveling in viscoelastic films*, J. Non-Newt. Fluid Mech., 1987, **22**, 219-233.
- [104] H. S. Kheshgi and L. E. Scriven, *The evolution of disturbances in horizontal*

- films*, Chem. Eng. Sci., 1988, **43**, 793-801.
- [105] L. E. Stillwagon and R. G. Larson, *Fundamentals of topographic substrate leveling*, J. Appl. Phys., 1988, **63**, 5251-5258.
- [106] B. Huner and P. K. Ajmora, *The leveling of a purely viscous nonvolatile printing ink on a rough substrate*, Proc. ISHM '89 Conf., Baltimore, 1989.
- [107] S. K. Wilson, *The leveling of paint films*, IMA J. Appl. Math., 1993, **50**, 149-166.
- [108] D. W. Bousfield, *Long-wave analysis of viscoelastic film leveling*, J. Non-Newt. Fluid Mech., 1991, **40**, 47-54.
- [109] L. W. Schwartz, D. E. Weidner, and R. R. Eley, *An analysis of the effect of surfactant on the leveling behavior of a thin liquid coating layer*, Langmuir, 1995, **11**, 3690-3693.
- [110] L. W. Schwartz, R. A. Cairncross, and D. E. Weidner, *Anomalous behavior during leveling of thin coating layers with surfactant*, Phys. Fluids, 1996, **8**, 1693-1695.
- [111] R. R. Iyer and D. W. Bousfield, *The leveling of coating defects with shear thinning rheology*, Chem. Eng. Sci., 1996, **51**, 4611-4617.
- [112] S. Betelú, R. Gratton and J. Diez, *Observation of cusps during the levelling of free surfaces in viscous flows*, J. Fluid Mech., 1998, **377**, 137-149.
- [113] M. H. Eres, D. E. Weidner, and L. W. Schwartz, *Three-dimensional direct numerical simulation of surface-tension-gradient effects on the leveling of an evaporating multicomponent fluid*, Langmuir, 1999, **15**, 1859-1871.
- [114] H. Sirringhaus, T. Kawase, R. H. Friend, T. Shimoda, M. Inbasekaran, W. Wu, and E. P. Woo, *High-resolution inkjet printing of all-polymer transistor circuits*, Science, 2000, **290**, 2123-2126.
- [115] B.-J. De Gans, P. C. Duineveld, and U. S. Schubert, *Inkjet printing of polymers: state of the art and future developments*, Adv. Mater., 2004, **16**, 203-213.
- [116] C. W. Sele, T. von Werne, R. H. Friend, and H. Sirringhaus, *Lithography-free, self-aligned inkjet printing with sub-hundred nanometer resolution*, Adv. Mater., 2005, **17**, 997-1001.
- [117] T. Kawase, S. Moriya, C. J. Newsome and T. Shimoda, *Inkjet printing of polymeric field-effect transistors and its applications*, Jpn. J. Appl. Phys., 2005, **44**, 3649-3658.
- [118] T. Sekitani, Y. Noguchi, U. Zschieschang, H. Klauk, and T. Someya, *Organic transistors manufactured using inkjet technology with subfemtoliter accuracy*, Proc. Natl. Acad. Sci. USA, 2008, **105**, 4976-4980.
- [119] J. Stringer and B. Derby, *Limits to feature size and resolution in ink jet printing*, J. Eur. Ceramic Soc., 2008, **29**, 913-918.
- [120] E. Tekin, P. J. Smith, and U. S. Schubert, *Inkjet printing as a deposition and patterning tool for polymers and inorganic particles*, Soft Matter, 2008, **4**, 703-713.

-
- [121] M. Singh, H. M. Haverinen, P. Dhagat, and G. E. Jabbour, *Inkjet printing-process and its applications*, Adv. Mater., 2010, **22**, 673-685.
- [122] H. Wijshoff, *The dynamics of the piezo inkjet printhead operation*, Phys. Rep., 2010, **491**, 77-177.
- [123] P. C. Duineveld, *The stability of ink-jet printed lines of liquid with zero receding contact angle on a homogeneous substrate*, J. Fluid Mech., 2003, **477**, 175-200.
- [124] A. A. Darhuber and S. M. Troian, *Principles of microfluidic actuation by modulation of surface stresses*, Annu. Rev. Fluid Mech., 2005, **37**, 425-455.
- [125] M. S. Borgas and J. B. Grotberg, *Monolayer flow on a thin film*, J. Fluid Mech., 1988, **193**, 151-170.
- [126] J. H. Snoeijer, *Free-surface flows with large slopes: Beyond lubrication theory*, Phys. Fluids, 2006, **18**, 021701.
- [127] D. P. Gaver and J. B. Grotberg, *Droplet spreading on a thin viscous film*, J. Fluid Mech., 1992, **235**, 399-414.
- [128] V. B. Fainerman, D. Möbius, and R. Miller (eds.), *Surfactants: Chemistry, Interfacial Properties, Applications*, Elsevier, Amsterdam, 2001.
- [129] M. Hanyak, A. A. Darhuber, and M. Ren, *Surfactant-induced delay of leveling of inkjet-printed patterns*, J. App. Phys., 2011, **109**, 074905.

List of publications

Journal publications

1. M. Hanyak, D. K. N. Sinz and A. A. Darhuber, *Surfactant spreading at liquid-liquid interfaces*, in preparation.
2. M. Hanyak, D. K. N. Sinz and A. A. Darhuber, *Soluble surfactant spreading on spatially confined thin liquid films*, *Soft Matter*, 2012, 8, 7660-7671. (Chapter 4 and 5)
3. D. K. N. Sinz, M. Hanyak, J. Zeegers and A. A. Darhuber, *Insoluble surfactant spreading along thin liquid films confined by chemical surface patterns*, *Phys. Chem. Chem. Phys.*, 2011, 13, 9768-9777. (Chapter 3)
4. D. K. N. Sinz, M. Hanyak and A. A. Darhuber, *Immiscible surfactant droplets on thin liquid films: Spreading dynamics, subphase expulsion and oscillatory instabilities*, *JCIS*, 2011, 364, 519529. (Chapter 2)
5. M. Hanyak and A. A. Darhuber, *Surfactant-induced delay of leveling of inkjet printed patterns*, *J. Appl. Phys.*, 2011, 109, 074905 1-9. (Chapter 7)

Conference proceedings

1. M. Hanyak, D. K. N. Sinz, J. Zeegers and A. A. Darhuber, *Surfactant spreading on thin liquid films on chemically patterned surfaces*, Proceedings of the International Conference on Multiphase Flow 2010
2. D. K. N. Sinz, M. Hanyak, J. Zeegers and A. A. Darhuber, *Self-propelling surfactant droplets on inclined thin liquid films*, Proceedings of the International Conference on Multiphase Flow 2010

Talks

1. D. K. N. Sinz, M. Hanyak and A. A. Darhuber, *Immiscible surfactant droplets on thin liquid films: Spreading dynamics, subphase expulsion, oscillatory instabilities and the effect of spatial confinement*, 64th Annual Meeting of

- the APS Division of Fluid Dynamics, Baltimore, Maryland, November 20th 2011;
2. M. Hanyak, A. A. Darhuber and Maosheng Ren, *Surfactant-induced delay of leveling of inkjet printed patterns*, Winning Symposium at Oce, Venlo, September 24th 2010
 3. D. K. N. Sinz, M. Hanyak and A. A. Darhuber, *Surfactant spreading on thin liquid films on chemically patterned surfaces*, Winning Symposium at Oce, Venlo, September 24th 2010
 4. M. Hanyak, D. K. N. Sinz, J. Zeegers and A. A. Darhuber, *Surfactant spreading on thin liquid films on chemically patterned surfaces*, International Conference on Multiphase Flow 2010, Tampa, Florida, May 30th 2010
 5. D. K. N. Sinz, M. Hanyak, J. Zeegers and A. A. Darhuber, *Self-propelling surfactant droplets on inclined thin liquid films*, International Conference on Multiphase Flow 2010, Tampa, Florida, May 30th 2010
 6. M. Hanyak, D. K. N. Sinz, J. Zeegers and A. A. Darhuber, *Surfactant spreading on thin liquid films on chemically patterned surfaces*, JMBC Burgersdag 2010, Twente, January 13th 2010

Poster presentations

1. M. Hanyak, D. K. N. Sinz and A. A. Darhuber, *Surfactant spreading on spatially confined thin liquid films*, JMBC Burgersdag 2012, Eindhoven, January 12th 2012
2. M. Hanyak, A. A. Darhuber and Maosheng Ren, *Surfactant-induced delay of leveling of inkjet-printed patterns*, JMBC Burgersdag 2012, Eindhoven, January 12th 2012
3. D. K. N. Sinz and A. A. Darhuber, *Self-propulsion of droplets on chemically confined thin liquid films - The basics, cargo transport and thermal routing*, JMBC Burgersdag 2012, Eindhoven, January 12th 2012
4. M. Hanyak, D. K. N. Sinz and A. A. Darhuber, *Surfactant spreading on spatially confined thin liquid films*, The 25th European Colloid and Interface Society conference, Berlin, September 4th-9th 2011
5. M. Hanyak, D. K. N. Sinz and A. A. Darhuber, *Insoluble surfactant spreading on spatially confined thin liquid films*, JMBC Burgersdag 2011, Delft, January 13th 2011

Summary

Marangoni flows induced by non-uniform surfactant distributions

The spreading dynamics of surfactants is of crucial importance for numerous technological applications ranging from printing and coating processes, pulmonary drug delivery to crude oil recovery. In the area of inkjet printing surfactants are necessary for lowering surface tension of water-based ink solutions, but can considerably delay the leveling and redistribution of inkjet-printed lines. In the context of oil recovery, up to about 60% of the originally present crude oil remains in a reservoir after the so-called primary and secondary recovery phases. Injection of surfactant solutions is considered a potential means for extracting a larger fraction of the oil owing to two different mechanisms. Surfactant-induced reductions of interfacial tension facilitate deformations of oil-brine interfaces and therefore oil extraction. Furthermore, a non-uniform surfactant distribution at fluid-fluid interface gives rise to interfacial tension gradients and associated Marangoni stresses, which generate flow from regions of lower to regions of higher interfacial tension. This can be utilized to transport surfactant along dead-end pores that are inaccessible to pressure-driven transport.

This dissertation is mainly dedicated to the modeling of liquid transport induced by non-uniform surfactant distributions at liquid-air and liquid-liquid interfaces. Several types of material systems were investigated for surfactant-induced flows in the presence of geometrical confinement and constraints. We monitor the evolution of the liquid height profile after non-uniform surfactant deposition at the interface. The most prominent morphological feature of the spreading process is the formation of a local maximum in film thickness, called rim, and its propagation away from the deposition region. The rim dynamics can be well approximated by power-law $x_{\text{rim}} \sim t^\alpha$, where α is called spreading exponent. We conducted an extensive numerical study of surfactant spreading on thin films and quantitatively compared our results with experimental data. In addition, we also investigated how surfactant-induced flow phenomena affect leveling and redistribution dynamics of inkjet-printed lines.

Chapter 2 presents the spreading dynamics of insoluble surfactants on thin liquid films with initially uniform thickness. Numerical simulations based on the lubrication approximation of the far-field axisymmetric spreading dynamics compare very favorably with the experimental results reported in the literature for oleic acid spreading on glycerol. The corresponding non-linear equation of state, which provides an excellent fit for the experimental dependence of surface tension on surfactant concentration, was shown to influence spreading rates considerably compared with a linear one. A fingering instability was observed, which is induced by the temporary entrapment of sub-phase liquid in the surfactant deposition area and its subsequent release. The expulsion has a direct effect by increasing the spreading exponent.

Chapter 3 is dedicated to insoluble surfactant spreading at curved liquid-air interfaces. Using a numerical model based on the lubrication approximation, we monitored the evolution of the liquid height profile after deposition of an insoluble surfactant monolayer at rivulet-air interface. Continuous, i.e. unlimited surfactant supply led to higher exponents and increased the influence of the rivulet aspect ratio as compared to the case of limited supply. The spreading exponents determined from a model implementing a continuous supply of surfactant compare favorably with experimental data for oleic acid on glycerol. The initial film thickness has little effect on the spreading exponents for surfactant spreading at rivulet interfaces. The lateral confinement induces non-uniform height- and surface velocity profiles, which manifest themselves in a pronounced transition of the evolving rivulet morphology.

Chapter 4 contains the study of soluble surfactant spreading on curved liquid-air interfaces. Our numerical model was based on the lubrication approximation and the assumption of vertically uniform concentration profiles. A proper choice of initial and boundary conditions in the numerical models resulted in spreading exponents that are in excellent agreement with the experimental results for sodium dodecyl sulfate spreading on narrow glycerol rivulets. The influence of fingering instabilities, commonly observed during the spreading process, on the rim shape and propagation rate was studied. The rim height profiles deduced from experiments were in excellent agreement with numerical data at early times, but systematically lower at later stages. The origin of this discrepancy resides in vertical concentration non-uniformities, caused by slow vertical diffusion of the surfactant, which is not accounted for in the lubrication model.

Chapter 5 deals with the spreading at liquid-air interfaces of a soluble, slowly diffusing surfactant. The spreading was studied by employing two different numerical models. The first model is based on the full Navier-Stokes equation and convection-diffusion equations for bulk- and surface surfactant transport. It accounts for domain deformability and allows for vertically non-uniform concentration profiles. The second model is based on the lubrication approximation and the assumption of vertically parabolic concentration profiles. The two studied models gave considerably different results with respect to film thickness evolution

for diffusion coefficients below a certain value. The difference originates in vertical concentration non-uniformities in the sub-phase liquid that are not accurately represented by the parabolic profile upon which the lubrication model was based.

In addition, Chapter 6 analyzes the spreading of a soluble surfactant at liquid-liquid interfaces between parallel solid plates. We consider an interface with initially uniform height as well as narrow rivulets with initially curved interface. A model accounting for vertically non-uniform concentration profiles was used for slowly diffusing surfactants, while a model based on the lubrication approximation corresponding to vertically uniform concentration profiles was applied in the case of sufficiently large diffusion coefficients. We conclude that two liquids of a similar viscosity result in lower spreading rates and rim heights compared to the liquids with large difference in viscosities. A comparison of rivulet height profiles from experiments for a material system characterized by a very small viscosity ratio with the lubrication model data yielded similar conclusions as for spreading at liquid-air interfaces. Good quantitative agreement can be obtained with the lubrication model with combination of continuous surfactant supply at the interface and finite supply in the bulk.

Finally, Chapter 7 investigates leveling and redistribution dynamics of inkjet-printed lines in the presence of soluble and insoluble surfactants. We present numerical results as well as scaling relations for both the leveling and redistribution times of sinusoidal ripples and multi-lines as a function of the number of individual lines, the lateral pitch, the average line height and width. Our results were obtained for a non-linear equations of state and in the case of soluble surfactants for surfactant adsorption kinetics described by a Langmuir equation, which provides a basis for estimating optimal process conditions. Surfactants cause surface tension gradients that oppose capillary leveling of ripples initially present at the surface, and thus can slow down the leveling process. The retarding effect of surfactants depends on rates of bulk-surface exchange.

Acknowledgements

"Would you tell me, please, which way I ought to go from here?"

"That depends a good deal on where you want to get to," said the Cat.

"I don't much care where—" said Alice.

"Then it doesn't matter which way you go," said the Cat.

"—so long as I get somewhere," Alice added as an explanation.

"Oh, you are sure to do that," said the Cat, "if you only walk long enough."

(Alice's Adventures in Wonderland by Lewis Carroll, Chapter 6)

Once upon a time, after reading the dialog between Alice and the Cat, I printed it out and hung it on my office wall. If I were Alice, then four years as a PhD candidate at Applied Physics department would be my adventure in Wonderland. Except ... it turned out to be surprisingly logical and I met many wonderful people on the way. To them I want to dedicate this last chapter of my thesis.

I would like to offer my deepest gratitude to Anton Darhuber for supervising my research work during this four-year period. I am thankful for his generously given support, encouragement, suggestions and, of course, his detailed comments and corrections.

Without the financial support from the Dutch Technology Foundation STW and Shell International Exploration and Production this research would have never been done. In particular, I want to thank Steffen Berg, Axel Makurat, Hans Reinten, Michel Riepen, Herman Wijshoff and Bo Xiao Zhou for the cooperation and their enthusiasm during the project.

Special thanks go to my project partner, David Sinz, for keeping his office doors open and sharing his knowledge, cookies and, sometimes, jokes with me. At times, the road to a PhD is not easy, but we made it.

I am grateful for all the help, amusing discussions, Dutch lessons and, lately, "vernacular Italian" course offered to me by Berend Brasjen. Many thanks to my colleagues with whom I enjoyed the time spent in Cascade: Aniruddha, Ariel,

Badr, Brigitte, Calin, Christian, Devis, Federico, Florian, GertJan, Gunes, Hao, Henny, Humberto, Jan, Jorge, Jorgen, Jos, Jens, Judith, Kees, Margit, Matias, Mico, Naveed, Oleksii, Paul, Prasad, Rafal, Raoul, Sebastian, Stefan, Sudhir, Theo, Timm and Valentina.

Last but not least, I would like to thank my husband, Tiberiu, for always being there for me and loving me for who I am.

Myra Hanyak
Eindhoven, August 2012

Curriculum vitae

- 27 July 1983 Born in Chyshky, Ukraine
- 2000-2004 **Bachelor of Science**
Department of Mechanics and Mathematics
Ivan Franko National University of Lviv, Ukraine
- 2004-2005 **Master of Science**
Department of Mechanics and Mathematics
Ivan Franko National University of Lviv, Ukraine
Topic: *Another proof of the Jensen theorem for an annulus.*
- 2005-2006 **Teaching/Research Assistant**
Department of Mechanics and Mathematics
Ivan Franko National University of Lviv, Ukraine
- 2006-2008 **Professional Doctorate in Engineering**
Department of Mathematics and Computer Science
Eindhoven University of Technology, The Netherlands
Topic: *Stability of the Dyneema spinning process.*
- 2008-2012 **PhD candidate**
Department of Applied Physics
Eindhoven University of Technology, The Netherlands
Topic: *Marangoni flows induced by non-uniform surfactant distributions.*

